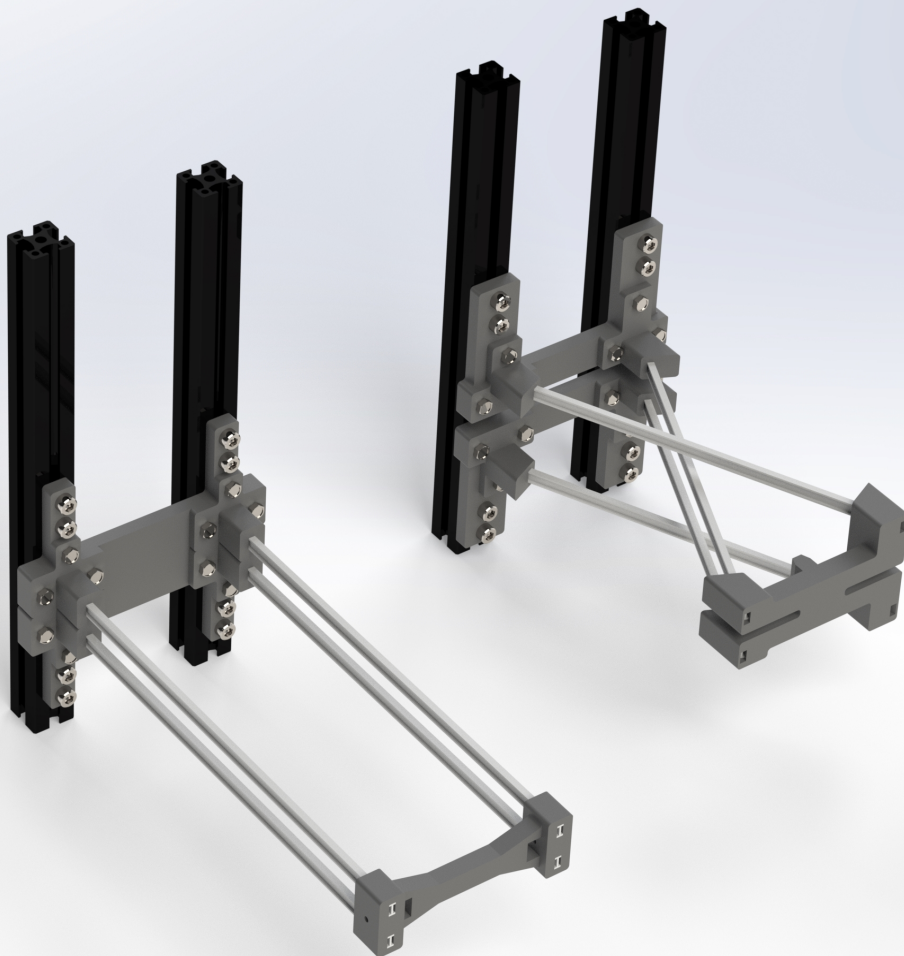


Department of Precision and Microsystems Engineering

Lateral torsional buckling in translational and rotational compliant joints to obtain zero-stiffness behaviour

Marco Moerman

Report no : 2023.013
Coach : Dr. ir. G. Radaelli
Professor : Prof. dr. ir. J.L. Herder
Specialisation : Mechatronic System Design
Type of report : Master Thesis
Date : February 24, 2023



Lateral torsional buckling in translational and rotational compliant joints to obtain zero-stiffness behaviour

by

Marco Moerman

to obtain the degree of Master of Science
at the Delft University of Technology,
to be defended publicly on February 24, 2023 at 13:30 PM.

Student number: 4460847
Project duration: September 1, 2021 – February 24, 2023
Thesis committee: Prof. dr. ir. J.L. Herder, TU Delft, chair
Dr. ir. G. Radaelli, TU Delft, daily supervisor
Dr. ir. J. Jovanova, TU Delft
Ir. A. Amoozandeh Nobaveh, TU Delft

An electronic version of this thesis is available at <http://repository.tudelft.nl/>.

Preface

This work marks the end of my time as a student at the University of Technology Delft. More than seven years ago I started with the bachelor in Mechanical Engineering. Followed by the High-Tech Engineering track of the Mechanical Engineering master program. This thesis, done within the ShellSkeletons research group, is the conclusion of this master's program. It was a journey with a lot of challenges but also valuable moments to remember.

This thesis, and all the work in the years before, would not have been possible without the support and guidance of many people. First of all, I would like to thank my supervisor Giuseppe for the interesting discussions during the meetings and his guidance when I needed it. Also, I would like to thank my fellow students and the other members of the ShellSkeleton group for the discussions in the group meetings, the assistance with my work, and all the lunch breaks. I also thank the students I have worked with in all those years for the collaboration in the group projects and the long study sessions before the exams.

Lastly, I would like to thank my parents, brothers, sisters, family and friends for their support and distraction when it was needed. A special thanks to my wife, for her patience from time to time and her neverending support.

*Marco Moerman
Delft, February 2023*

Contents

1	Introduction	1
2	Literature survey	3
3	Research paper	17
4	Discussion	33
4.1	Discussion literature review	33
4.2	Discussion research paper	33
4.3	General discussion and recommendations	34
5	Conclusion	35
A	Rigidities	39
A.1	Axial rigidity	39
A.2	Flexural rigidities	40
A.3	Torsional rigidity	42
B	Torsional constant	45
B.1	Optimal shape	45
B.2	Definition torsional constant	46
C	Experiments	49
C.1	Testing protocol.	49
C.2	Parasitic x -displacement	50
C.3	Additional photos.	51
C.4	Rotation shuttles	53
D	Rotational joint	55
D.1	Basic model.	55
D.2	Improvement zero-stiffness range	56
E	Twisted beam	59
F	Matlab code	61
F.1	Analysis mechanism	61
F.2	Sensitivity analysis	65
G	Data processing	73

1

Introduction

Mechanisms are all around us, and we use them every day. From the drive-train in a car and your bicycle to the lock of a door, the mechanism of a clock and a wrench. A definition that includes all these mechanisms is: “Mechanical device used to transfer or transform motion, force, or energy” [1]. In a conventional mechanism, multiple parts are working together to achieve this. Examples of such parts are: gears, belts, chains, rigid links, bearings and springs [2]. An alternative to conventional mechanisms is the use of compliant mechanisms. A compliant mechanism uses elastic deformation to achieve the transfer of motion, force, or energy. The field of compliant mechanisms is a popular research subject because of the advantages compliant mechanisms have over conventional mechanisms; less parts are required to build a compliant mechanism, resulting in a light-weight mechanism with lower assembly costs that require less maintenance, there is no backlash or friction and no lubrication is required [3, 4]. Compliant mechanisms can also be found in our daily life. In the supermarket, the cap of a bottle of sauce is connected to the bottle with a compliant hinge. Figure 1.1 shows two versions of the mechanism inside a bicycle bell. In Figure 1.1a, a spring is connected to a lever to transform the applied force of your thumb into a rotation of the gear. In Figure 1.1b the spring and lever are combined into a single compliant part with the same functionality.



(a) A conventional mechanism in a bicycle bell consisting of a spring and a lever [5].

(b) A compliant mechanism in a bicycle bell consisting of a single part.

Figure 1.1: A comparison between two types of mechanisms in a bicycle bell.

The use of compliant mechanisms also has some drawbacks. The main drawback is that external work is required to elastically deform the mechanism [1], i.e. the mechanism has a certain stiffness in the desired direction of motion. The elastic material behaves like a spring, without an applied force the mechanism will stay in the equilibrium position. However, there is a solution for this drawback; with the right combination of geometry, stiffness and prestress the stiffness can be reduced or even removed [6]. If the stiffness is successfully removed, the compliant mechanism has zero-stiffness behaviour [7], also referred to as neutral-stability. Therefore, a large part of the research on compliant mechanisms is focussed on creating compliant mechanisms with zero-stiffness behaviour [8, 9]. The basic principle is based on applying a preload in the stiffest direction of the flexible beam [10]. At a certain preload, the bending stiffness approaches zero and

zero-stiffness is obtained [11, 12]. In most zero-stiffness compliant mechanisms, leaf springs are preloaded in their stiffest direction [13, 14, 15, 16, 17]. This corresponds to the compression of the leaf springs and the critical preload is related to the critical load for Euler buckling [18].

Euler buckling is not the only existing type of buckling. One of the other types is lateral torsional buckling (LTB). This type of buckling typically occurs for slender beams with open cross-sections such as an I-section [19]. LTB occurs when a bending load is applied in the stiffest bending direction of the beam. Figure 1.2 provides a drawing of the undeformed and deformed state for LTB of an I-beam. Due to the type of cross-section, the stiffest bending direction is bending around the y -axis. If a force F is applied in the positive z -direction, the bottom flange of the I-beam is compressed and the top flange is tensioned. For a certain critical force LTB occurs, causing the I-beam to deflect laterally by a distance u and rotate by an angle α [20, 21]. LTB is well known in civil and structural engineering, where slender beams with open cross-sections are used for mass reduction. However, the focus of these engineering fields is on preventing LTB instead of using the elastic deformation of the beams [22].

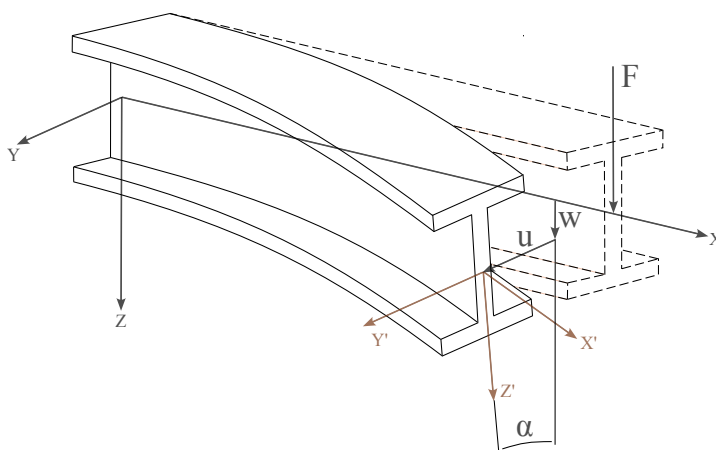


Figure 1.2: Unloaded and loaded configuration for lateral torsional buckling of an I-beam. A force F is applied, and when lateral torsional buckling occurs the deformed beam has a lateral displacement u and a rotation α .

The objective of this research is to investigate the possibility of implementing lateral torsional buckling into a compliant mechanism to obtain zero-stiffness behaviour. The hypothesis is that this working principle can successfully be implemented if the bending force is applied in the stiffest bending direction of the beam. In order to investigate this, the thesis is divided into two parts. First, a literature review is conducted on the buckling behaviour of Euler buckling and lateral torsional buckling. The focus of this literature review is on calculation methods that are used to calculate the critical buckling load for both types of buckling. The obtained knowledge is used in the research paper which is the second part of this thesis. The research paper proposes a method to implement lateral torsional buckling in compliant joints to obtain zero-stiffness behaviour. When the movements of a mechanism are evaluated, two main types of motion can be distinguished; translation and rotation. In the research paper, two types of compliant joints with these motions are considered; a translational joint [23, 24, 13] and a rotational joint [25, 16]. In the paper, an analytical analysis is carried out on the lateral torsional buckling of an I-beam. Next, the two joints are implemented in a finite element analysis (FEA) to simulate the zero-stiffness behaviour. A sensitivity analysis is performed to investigate how the cross-sectional dimensions affect the zero-stiffness behaviour. Lastly, the results from the FEA are verified by experiments on prototypes of the two joints.

The outline of this report is as follows. In Chapter 2, the literature review on calculation methods for the buckling behaviour of Euler buckling and lateral torsional buckling is provided. Next, the research paper on the implementation of lateral torsional buckling in translational and rotational compliant joints to obtain zero-stiffness behaviour is provided in Chapter 3. The obtained results in this work will be discussed in Chapter 4, followed by a general conclusion in Chapter 5. Lastly, any additional material that is used in this work is provided in the Appendices.

2

Literature survey

Literature review on calculation methods for the buckling behaviour of Euler buckling and lateral torsional buckling

Marco Moerman

Abstract—Compliant mechanisms are a popular alternative to conventional mechanisms because of their advantages in mass reduction, friction, backlash and lubrication. A drawback in the use of compliant mechanisms is the presence of stiffness. The advantages of compliant mechanisms and conventional mechanisms can be combined if the stiffness in the direction of motion of the compliant mechanism can be reduced or ideally removed. If the stiffness is successfully removed a zero-stiffness compliant mechanism can be realized. The creation of zero-stiffness mechanisms is often based on the principle of Euler buckling. A possible alternative for Euler buckling could be the use of lateral torsional buckling in compliant mechanisms. In this literature review calculation methods for the buckling behaviour of Euler buckling and lateral torsional buckling are discussed. The found methods are provided in an overview and compared to each other using comparison criteria to investigate the possibility of using lateral torsional buckling to create zero-stiffness compliant mechanisms.

Index Terms— Lateral torsional buckling, column buckling, Euler buckling, critical load, compliant mechanisms, zero-stiffness

I. INTRODUCTION

Compliant mechanisms are a popular alternative for conventional mechanisms for several reasons; the same mechanism can be built using less parts resulting in a light-weight mechanism, no lubrication is needed and there is no friction or backlash [1]. In a conventional mechanism rigid parts connected by joints are used to achieve force and/or motion transmission. In a compliant mechanism, however, elastic deformation is used to achieve this transmission. Compliant mechanisms are a research field where possibilities are explored looking for clever designs. An interesting possibility is the use of compliant mechanisms in exoskeletons. Next to the already mentioned advantages compliant mechanisms show potential in terms of adaptability, safety, efficiency and comfort [2]. These are all important properties of exoskeletons which explain the interest in the use of compliant mechanisms.

The use of compliant mechanisms introduces also some design challenges. One of the main challenges is the requirement of external work to elastically deform the mechanism due to the stiffness of the mechanism [3]. Part of the research in

compliant mechanisms is focused on reducing or removing this stiffness in a mechanism in order to create a zero-stiffness compliant mechanism [4]. With the right combination of geometry, stiffness and prestress the stiffness can be removed. If this is successfully done the advantages of compliance can be used without the requirement of external work.

One of the possible solutions to this challenge is using the principle of Euler buckling in a compliant mechanism. Euler buckling is also known as column buckling and is described by Leonard Euler in 1757 [5]. A compressive axial load is applied to a column and for a certain critical load, the column is put in a state of unstable equilibrium. A load beyond this critical load results in the buckling of the column which can be observed by the lateral deflection of the column. In compliant mechanisms, this principle is used by applying an axial load on a leaf spring or a similar type of compliant member. The lateral instability at the critical load can be used to create a zero-stiffness mechanism [6]–[8]. By applying a load that is beyond the critical load bistable behaviour can be obtained. Instead of the unstable equilibrium the mechanism now has two stable states [9]–[11].

Euler buckling is not the only existing type of buckling. Lateral Torsional Buckling (LTB) is a type of buckling that occurs typically for slender beams with open cross-sections [12]. LTB is mostly known in civil- and structural- engineering where slender open cross-section beams are often used for mass reduction. In most cases, an I-beam is used. LTB occurs when a downward load is applied on the I-beam resulting in compression of the bottom flange and tensioning of the top flange. At a certain critical load this results in an instability which causes the I-beam to deflect laterally and twist at the same time [13]. Early studies on LTB were carried out by Prandtl (1899) and Timoshenko (1953) [14], [15]. Due to the static nature of civil- and structural- engineering LTB is an undesired phenomenon considered to be a failure mode [16]. Therefore, a lot of research is carried out to obtain the critical load for LTB. However, literature on LTB loads beyond the critical load or post-buckling behaviour is not available.

It would be interesting to investigate the possibility to use LTB as an alternative for Euler buckling in a compliant mechanism to obtain zero-stiffness behaviour. Therefore it is required to get more insight into both types of buckling. The aim of this literature review is to find methods for calculating the critical load behaviour of both Euler buckling and lateral torsional buckling. There are three main approaches to calculate these; empirical, analytical and numerical. The goal is to find similarities between the types of buckling to see if it is possible to implement LTB in a compliant mechanism to obtain zero-stiffness behaviour.

This literature review is written for the ME56010 course of the Mechanical Engineering - High Tech Engineering program at the University of Technology Delft)

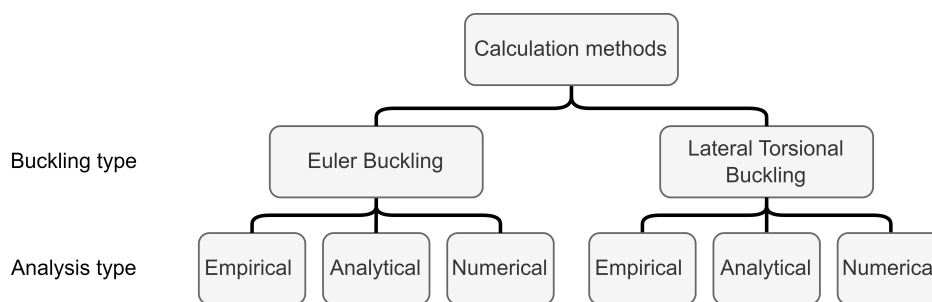


Fig. 1. Categorization literature review

In this literature review, the different techniques to calculate the buckling behaviour of Euler buckling and lateral torsional buckling are investigated and categorized. In Section II the used method including the categorization, search protocol and comparison criteria are described. Next in Section III the found literature is presented and will be compared using the proposed criteria. In Section IV the results will be discussed and the gaps in the literature will be identified. Lastly, the conclusion of the literature review is given in Section V.

II. METHODS

In this section, the methods used in this literature review are discussed. First, the categorization that will be used to distinguish the found literature will be introduced. Next, the search protocol which will be used to find all the relevant literature is described. Lastly, the criteria for comparison of the literature are given.

The aim is to compare different calculating methods for Euler Buckling and LTB. In order to do this systematically the found literature is divided into categories. The first distinction of the categorization is made on the type of buckling. The focus of this review is on two types of buckling; (i) *Euler buckling* and (ii) *Lateral Torsional Buckling*. Also, a distinction is made based on the calculation method. Here three types of analysis are available. An (i) *empirical analysis* is based on the results of experiments. An (ii) *analytical analysis* uses theoretical formulas to obtain a result. In a (iii) *numerical analysis* the problem is solved using algorithms that use numeric approximations. In many papers, multiple types of analysis are used. For example, a numerical method is proposed and the results of this analysis are validated by experiments. Or some analytical background is given which will be used in the numerical analysis. In such a case, it is possible that a single paper is used in two categories if both types of analysis can be used independently. A schematic overview of this categorization is provided in Figure 1.

In order to find all the relevant literature in a systematic way a search protocol is composed. The relevant keywords and search terms used in this search are provided in Table II. The terms in each column can be combined with a term from another column to obtain a complete search term. For example "Euler buckling" from column one combined with "Critical Load" from column two and "Analysis" from column three result in the complete search term "Euler buckling critical load

analysis". In order to find the literature search engines such as Scopus, ScienceDirect, Google Scholar and the TU library are used.

TABLE I
OVERVIEW OF USED SEARCH TERMS TO FIND LITERATURE ON
CALCULATION METHODS

Search terms combined with AND/OR		
Column buckling	Critical load	Calculation
Lateral buckling	Critical moment	Numerical
Torsional buckling	Failure	Analytical
Lateral torsional buckling	Stability	Empirical
Euler buckling	Load	Measurements
Flexural buckling		FEM
Flexural torsional buckling		Analysis
		Experiments

After all the literature is gathered also a comparison is made between the found calculation methods. For this comparison, some criteria are chosen on which each method will be examined. The first criterion is *correctness*, for every method an indication of the correctness is given. A method is an estimate (-) if the result can only be used to give an estimation of the actual result, accurate (++) if the result has high precision and one of these three other levels (-, +- and +) if it is somewhere in between. This assessment is based on the results reported in the corresponding work. The second criterion is *computation time*. Here five levels of computation time are defined; slow (-), fast (++) and again the levels in between (-, +- and +) for very slow to very fast computations respectively. The next criterion is called *applicability* which gives an indication of the flexibility of the found method to apply to slightly different situations. This gives an indication of how many boundary conditions and load cases are taken into account in the method. Also here five levels are defined; bad (-) if the method can only be used for a single situation, good (++) if the method is applicable for (almost) all possible situations and the other levels (-, +- and +) if it is somewhere in between. The last criterion is *difficulty* as an indication of how difficult it is to implement and use the method. In this case, possibilities are difficult (-), easy (++) and the other options (-, +- and +) for methods of decreasing difficulty.

III. RESULTS

The results of the literature review are discussed in this section. First, an overview is given of the number of papers found for each category. Next, for each category, the relevant information found in the literature is provided. Lastly, the found literature is summarized in a table and the assessment made based on the comparison criteria is discussed.

In Table III the number of papers for each category is provided. The abbreviations used in this table are; EB (Euler Buckling), LTB (Lateral Torsional Buckling), E (Empirical), A (Analytical) and N (Numerical). Also, the references to the papers in every category are given.

TABLE II
NUMBER OF PAPERS FOUND FOR EACH CATEGORY

Category	Number of papers	Sources
EB-E	4	[17]–[20]
EB-A	7	[15], [21]–[26]
EB-N	4	[27]–[30]
LTB-E	5	[31]–[35]
LTB-A	9	[15], [36]–[43]
LTB-N	5	[31], [38], [40], [43], [44]

A. Euler buckling - critical load

Empirical. The first method to determine the critical load for Euler buckling is empirical research. Experiments are conducted and can be compared to known references for validation. In other cases, the experiments are used as validation for a proposed analytical or numerical method. In an experimental investigation by Ban et al., [17], [18] the buckling behaviour of steel columns is investigated. In this research initial imperfections such as residual stress, initial bending and loading eccentricity are measured beforehand and taken into account in the comparison. In total twelve specimens are tested, some are box-sections and some are I-sections, which are welded together. On both ends, a cylindrical hinge is attached to ensure the pin support. The compression load is applied by a hydraulic actuator. Transducers are used to measure the relevant horizontal and vertical displacements and rotations. The results from these experiments can be displayed in a force-displacement diagram as shown in Figure 2. In the end, the results from the imperfect specimens are compared with results from a Finite Element Analysis (FEA). This comparison is used to predict the buckling behaviour for imperfect columns with different dimensions.

A similar empirical study was conducted by Shi et al. [19]. In this study, the focus is on determining the critical load for circular columns with imperfections. To fit the boundary conditions spherical hinges are used on both sides. This allows rotation of the column. Some pictures of three columns with different lengths are provided in Figure 3. The red lines in these pictures correspond to the deformed centerlines of the columns. In this study the results are used to modify the existing design code, the Eurocode 3 [45], by adding an imperfection factor to it to further improve the design efficiency.

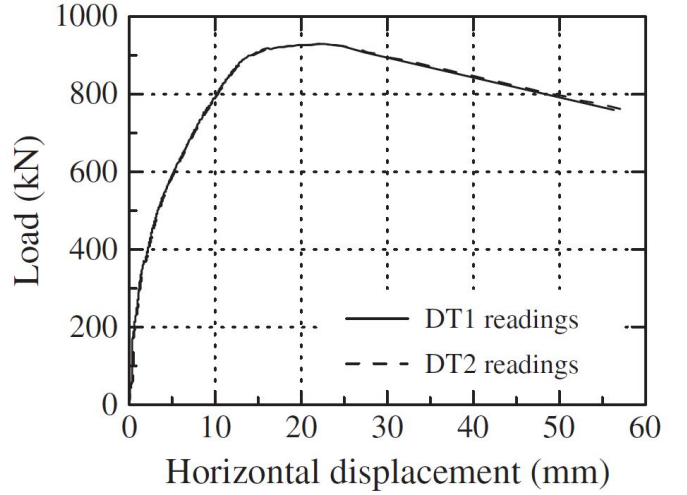


Fig. 2. Typical loading-horizontal displacement curve [17].

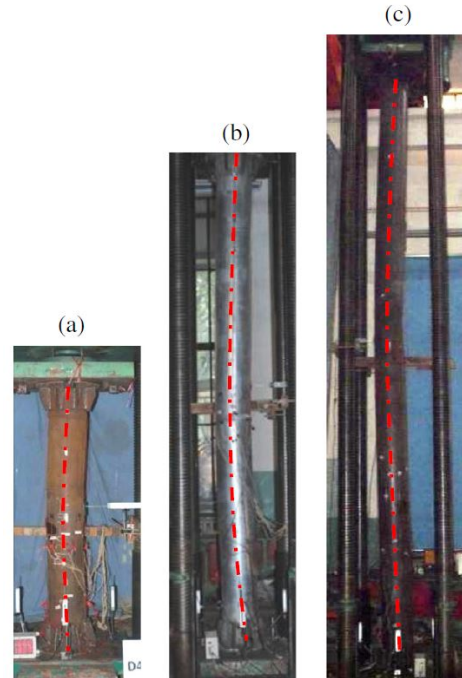


Fig. 3. Column in buckled state for three different specimens [19].

In the work of Luible & Crisinel [20], an experimental study is performed to find the buckling behaviour of columns made of glass elements. An eccentric compression load is applied to the column which is again supported by two cylindrical hinges. The columns are tested for different values of the slenderness ratio and the results are compared to a theoretical Euler curve as shown in Figure 4. In this experiment, an initial deformation w_0 is used.

Analytical. In the work of Timoshenko et al. [15] the critical load for a compressed bar is obtained by considering the behaviour of an ideal column. This ideal column is assumed to be perfectly straight and compressed by an applied load. The critical load is calculated using the differential equation

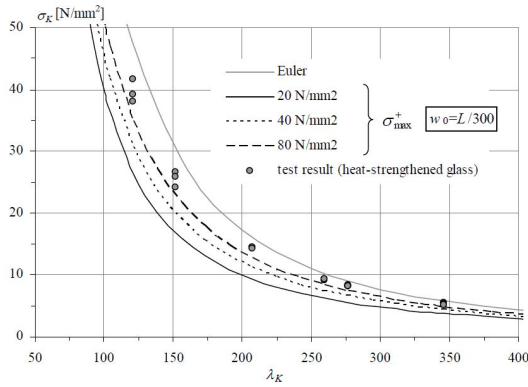


Fig. 4. Euler buckling and test results [20].

of the deflection curve of the column. Euler buckling for a column of which the upper end is free is shown in Figure 5. This figure shows different buckling modes for these boundary conditions.

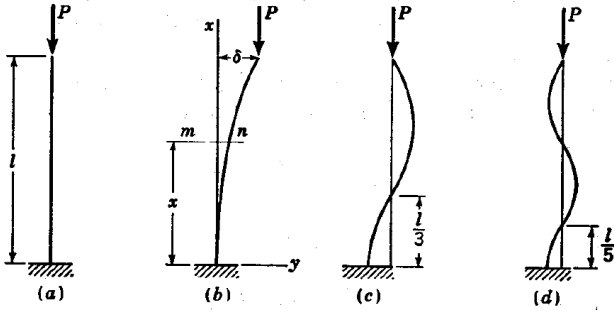


Fig. 5. Column or Euler buckling [15]

The curvature of the axis of the beam for a given bending moment is

$$EI \frac{d^2 y}{dx^2} = -M. \quad (1)$$

The quantity EI in this formula is the flexural rigidity of the beam. The bending moment at any cross-section $m - n$ in Figure 5(b) is

$$M = -P(\delta - y). \quad (2)$$

If this bending moment is inserted in Equation 1 this differential equation becomes

$$EI \frac{d^2 y}{dx^2} = P(\delta - y). \quad (3)$$

By inserting the simplification $k^2 = \frac{P}{EI}$ into Equation 3 the equation can be rewritten in the form

$$\frac{d^2 y}{dx^2} + k^2 y = k^2 \delta. \quad (4)$$

The solution of this differential equation with the boundary conditions at the lower end of the column taken into account is

$$y = \delta(1 - \cos(kx)). \quad (5)$$

The boundary condition at the upper end of the column is satisfied if $\delta \cos(kl) = 0$. This gives the expression

$$kl = (2n - 1) \frac{\pi}{2}. \quad (6)$$

The smallest critical load is obtained by taking $n = 1$ in Equation 6. The value of the critical load P is

$$P_{cr} = \frac{\pi^2 EI}{4l^2}. \quad (7)$$

The formula obtained in Equation 7 is valid for these specific end conditions; one end of the column is fixed and the other end is free. The formula is slightly different for other boundary conditions. In the work of Qiao, & Davalos [21] an overview is given of some possible boundary conditions as shown in Figure 6. With the effective length factor including Equation 7 can be written as

$$P_{cr} = \frac{\pi^2 EI}{l_e^2}. \quad (8)$$

In this expression, l_e is the effective length. The first set of end conditions in the figure corresponds to the situation of Equation 7 by using $l_e = 2l$. The other possible boundary conditions result in different values for the critical load. The effective length factor for a special set of end conditions is discussed by Cao et al. [22]. Instead of fixed ends of the column, rotational spring hinges are used resulting in a counteracting moment when the column is bending. Depending on the stiffness of the springs the effective length factor l_e lies between 0.5 and 1, corresponding with situations (b) (no stiffness) and (d) (high stiffness) in Figure 6.

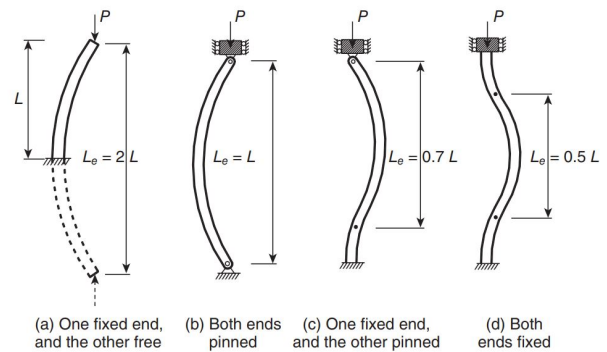


Fig. 6. Effective length factors for various end-conditions [21].

There are also analytical expressions available when the load is not applied through the centroid of the column [23], [24]. In this case, the load is applied at an eccentric distance e . For increasing values of e the maximum deflection v_{max} of the column also increases. This deflection can be calculated using

$$v_{max} = e \left[\sec \left(\sqrt{\frac{P}{EI}} \frac{L}{2} \right) - 1 \right]. \quad (9)$$

Webber et al. [25] propose a method for calculating the effective length of columns in multi-story frames. Such frames are built from separate beams which are connected to each other. These connections influence the effective length of the whole frame resulting in a different critical load. This method is taken a step further by Slimani et al. [26]. In this work, the effective length factor of columns in frames is determined for asymmetrical frames which are asymmetrically loaded. From both studies can be concluded that the effective length factor is strongly affected by the stiffness and loading conditions in the adjacent columns.

Numerical. In a numerical study conducted by Desai & Satish [27] the effect of the slenderness ratio on the critical load for Euler buckling is investigated. The formula for the slenderness ratio is

$$\lambda = \frac{l_e}{r}, \quad (10)$$

$$r = \sqrt{\frac{I}{A}}.$$

It is defined as the effective length l_e divided by the minimum radius of gyration r . This minimum radius of gyration is the root of the smallest moment of inertia I divided by the cross-sectional area A . In this study some assumptions are made; the column is perfectly straight and the load is applied axially, the cross-section is uniform, the material is perfectly elastic homogeneous and isotropic and the length of the column is large compared to the size of the cross-section. The analysis is carried out in ANSYS in which the columns are modelled using 80 elements. An eigenvalue buckling analysis is conducted and the found critical load is compared to the theoretical value. It was found that results between the numerical analysis and theoretical results were relatively large for a slenderness ratio smaller than 50.

The work of Yazdchi & Anaraki [28] focuses on the presence of a crack in one of the sides of the column. The goal is to find how this crack influences the buckling behaviour of the column. In this study, ANSYS is used to perform the FEA and the Euler-Bernoulli beam model is used. The cracked section is modelled as a rotational spring, the stiffness of this spring depends on the properties of the crack. It was found that the effects of the crack depend strongly on the location and the depth of the crack. The buckling load decreases when the flexibility of the column increases (so the stiffness becomes smaller).

In the work of Shi et al. [29] a FEA is used to determine the buckling behaviour of equal angle profiles. This analysis is performed using ANSYS and the element-type SHELL 181 is used. This type of element supports non-linear buckling analysis and also has to option to include initial stress in the model. An element has 4 nodes with 6 Degrees of Freedom (DoF) each. Part of the study is to investigate the influence of an end plate at both ends of the column, the model of this configuration is shown in Figure 7.

A numerical method to investigate the buckling behaviour of columns under eccentric compression is proposed by Zhao et al. [30]. In this study, the focus is on two types of columns; square hollow section (SHS) and circular hollow section

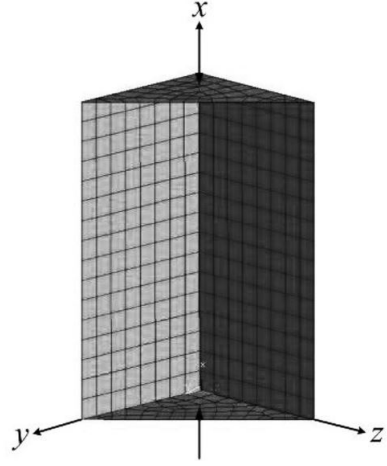


Fig. 7. Finite element model of the column including end plates [29].

(CHS) columns. The FEA software ABAQUS is used and geometric and material nonlinearities are taken into account. To describe the non-linear stress-strain relationship the Ramberg-Osgood model is used. In ABAQUS the solid element C3D8R is used to model the rigid ends of the columns and shell element S4R is used to model the columns. An example of the deformed model in the first buckling mode is shown in Figure 8 for both types of columns.

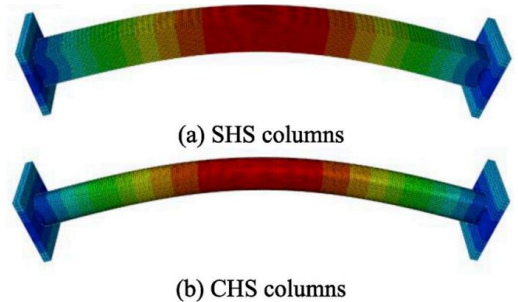


Fig. 8. Deformed model for SHS and CHS columns [30].

B. Lateral torsional buckling

Empirical. In the work of Demirhan et al. [31] an experimental study is performed on cantilever I-beams loaded under a point load at the free end of the beam. There are two main experimental variables in this study. The length of the cantilever is varied to investigate the influence of the slenderness ratio on the performance of the beam. For this experiment beams of three different lengths are used. The second variable is the height of the application point of the load on the beam with respect to the shear center. In Figure 9 this height is defined as the variable z_g and can be a positive or a negative value. In this study, three different force application points are used: at the top flange, at the bottom flange and at the shear center of the beam. The three variations in length and force application points result in nine different test specimens.

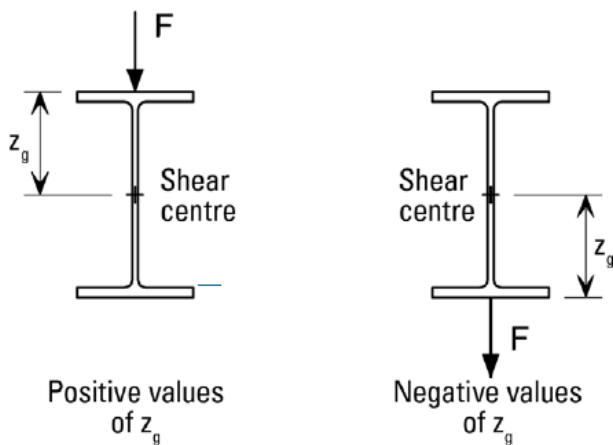


Fig. 9. Application point of the force with respect to the shear center [13].

For the experiments, a set-up is used where one end of the beam is fixed and a load is applied on the other end. A schematic overview of this test set-up is shown in Figure 10. Most important in this setup is the hydraulic jack which applies an increasing force on the beam and the load cell which measures the applied force. Also, two distance sensors are used to measure the vertical and lateral displacement of the tip of the beam.

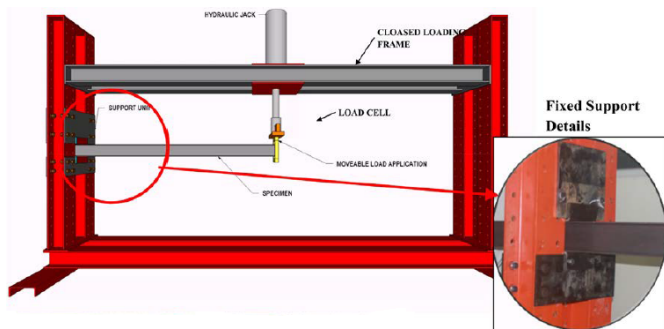


Fig. 10. Schematic overview of test set-up [31].

The results of the experiments are compared to a numerical calculation. One of the resulting graphs is shown in Figure 11. It is a load-lateral displacement graph that clearly shows the increase of lateral displacement at a certain (critical) load. From the experiments is concluded that decreasing the slenderness of the beam results in an increased critical load. For the second experimental variation is found that loading at the bottom flange results in the highest critical loads, followed by the shear center and the top flange with the lowest critical loads.

Similar studies as the one described above are conducted for different types of boundary conditions. In the work of Mottram [32] a simply supported I-beam, but with lateral deflection, warping and twist at the ends restrained, is investigated. In this study, a single load is applied at the middle of the beam. Bhat & Gupta [33] have conducted an experimental study with similar boundary conditions, but the load is now applied at

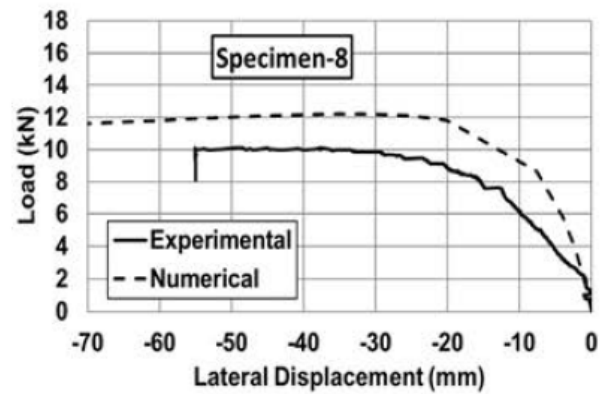


Fig. 11. Load - lateral displacement graph of one of the specimens [31].

two locations on the span of the beam. The focus of this study is to investigate the influence of holes in the web of the beam. The results are compared with a FEA and a factor is introduced to give an indication of the influence of the holes. The work of Fortan & Rossi [34] has a focus on the buckling behaviour of welded I-beams. In total 13 welded I-beams of varying cross-section dimensions and lengths are tested. The beams are placed on fork supports and four-point bending tests are carried out. In the experiments, geometrical imperfections and residual stresses introduced by welding are taken into account. The results are compared with the available design codes. In an experimental study by Jankowska-Sandberg et



Fig. 12. Steel buckled I-beam [34].

al. [35] the lateral torsional buckling behaviour of a steel truss is investigated. Instead of a single beam, a truss is build consisting of a number of beams. Several experiments are performed on different configurations and load cases. In this study was found that the critical load depends on the type of loading (on the top or on the bottom of the truss), on the dimensions of the truss and members and on the stiffness of the connections of the members.

Analytical. One of the first analytical descriptions of LTB was provided by Timoshenko & Gere [15]. In this derivation, nonlinear differential equations are used to obtain the critical

load for a cantilever I-beam. The results of these calculations are

$$\begin{aligned} P_{cr} &= \gamma_2 \frac{\sqrt{EI_y C}}{l^2}, \\ C &= GJ, \\ C_1 &= EC_w, \\ C_w &= \frac{t_f h^2 b^3}{24}, \\ \gamma_2 &= \frac{4.013}{(1 - \sqrt{C_1/l^2 C^2})}. \end{aligned} \quad (11)$$

C is considered to be the torsional rigidity and C_1 is the warping rigidity. γ_2 is a dimensionless stability coefficient that is dependent on the ratio $l^2 C/C_1$. For large values of this ratio, the dimensionless factor can be calculated using the formula shown below. For smaller values, a table is provided in which the value for γ_2 can be found. Some variations in boundary conditions and load cases are mentioned by Timoshenko & Gere: LTB of beams in pure bending and LTB of simply supported beams.

Over the years many improvements are made in the formulation of Timoshenko & Gere. In the case of a cantilever beam the most extensive formulation is given by Andrade et al. [36]. This paper provides a formula that can be both singly and doubly symmetric. A distributed load, concentrated load or a combination can be used. Also, the option to add a warping constraint at the fixed end of the beam is included. A schematic representation of the used cantilever is shown in Figure 13.

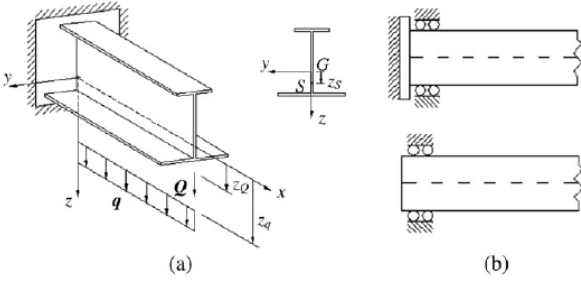


Fig. 13. (a) Representation of the used cantilever. (b) Warping conditions at the fixed end. [36].

The expression for the critical moment is

$$M_{cr} = C_1 \frac{\pi^2 EI_z}{(k_z L)^2} \times \left[\sqrt{\left(\frac{k_z}{k_w}\right)^2 \frac{I_w}{I_z} + \frac{(k_z L)^2 GI_t}{\pi^2 EI_z}} + (C_2 z_g - C_3 z_j)^2 - (C_2 z_g - C_3 z_j) \right]. \quad (12)$$

C_1, C_2 and C_3 are coefficients depending on the load case, warping conditions, cross-section symmetry and dimensions. The dependence on cross-section dimensions is taken into account in the dimensionless parameter \bar{K} , calculated by

$$\bar{K} = \frac{\pi}{L} \sqrt{\frac{EI_z h_s^2}{4GI_t}}. \quad (13)$$

Low values of \bar{K} correspond to short compact cantilevers while high values of \bar{K} correspond to long slender cantilevers.

k_z and k_w are effective length factors. z_j is a cross-sectional property that depends on the asymmetry between the top and the bottom flange. In the case of a doubly symmetric beam $z_j = 0$.

An analytical method to obtain the governing differential equations of LTB is introduced by Yoo & Lee [37]. This method is called the Energy Method. The critical load is derived for an I-beam supported at both ends with an applied distributed transverse load. First, the strain energy of the loaded equilibrium configuration is calculated. Also, the loss of potential energy of the transverse load is calculated. The change of potential energy from the unbuckled to the buckled state is used. With the strain energy and the loss of potential energy, the total energy function $\Pi = U + V$ is composed. By solving the differential equations of Π , a characteristic equation for the critical moment is obtained. This equation is similar to the one obtained by Timoshenko & Gere in Equation 11 but can be used in more cases because the stability coefficient γ_2 is given for more loading and boundary conditions. A schematic representation of some of the boundary conditions is shown in Figure 14. The paper provides stability coefficients for various loading and boundary conditions. With these stability coefficients, the critical moment is determined for the specific set of conditions.

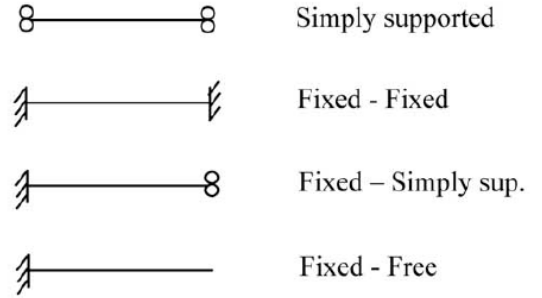


Fig. 14. Schematic overview of possible boundary conditions [38].

The study also introduces the Rayleigh-Ritz method to determine an approximation of the critical loads for LTB. This is a method to obtain the eigenvalues of the differential equations used in the Energy Method. An important observation made in this work is the effect of the position of the transverse load with respect to the shear center of the beam. When the load is applied on the upper flange of the beam it tends to increase the rotation and therefore had a destabilizing effect. This results in a lower critical load. An applied load on the bottom flange on the other hand has a stabilizing effect and results in a higher critical load.

A similar approach to the Energy Method is used in the work of Raftoyiannis & Adamakos [38]. The paper uses a simplified expression for the potential energy loss obtained from Chajes [46]. Also is the critical moment specifically calculated for web-tapered I-beams. The focus of the study is on determining modification factors to calculate the critical load when web-tapered I-beams are used. A variation in this study is performed by Yuan et al. [39]. In this study the focus of also on web-tapered beams, but the critical buckling load

is calculated for T-section beams instead. The influence of the flange width, indicated by the ratio (width/web height), on the critical load is also investigated.

An analytical method to calculate the critical load for a beam that is restrained against warping at the supports is described in a study conducted by Piotrowski & Szychowski [40]. In this paper, the beam is stiffened by adding for example a plate at the end of the beam which results in a different stiffness. For the calculation of the critical load, the energy method is used. An extra term is added to the total energy function in which the elastic energy of the restraint against warping is calculated. The study provides also a set of approximation formulas for different loading schemes. These formulas contain coefficients that are dependent on a factor κ . The value of this fixity factor κ depends on the type of restraint at the end of the beam.

In the work of Challamal, & Wang [41] a method is proposed for the analytical calculation of the critical load for intermediate and end point loads of a cantilever beam. The paper uses the exact buckling formula derived for Euler columns [47] and extends these results to LTB. An important property of the cantilever beam used in this study is the narrow rectangular cross-section as shown in Figure 15. The equilibrium equations that need to be solved in this method are second-order linear differential equations. Using an I-beam was not considered in this study because it requires the implementation of warping in the calculations. Warping leads to fourth-order differential equations instead of second-order differential equations.

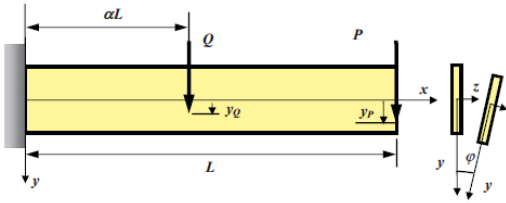


Fig. 15. LTB of a cantilever beam under combined intermediate and end point loads. [41].

In the work of Bresser et al. [42] a general formulation of an equivalent moment factor for elastic LTB is proposed. The paper focuses on slender rectangular sections and I-section beams. The known design codes provide a procedure to design beams based on equivalent moment factors. However, in many cases, a load pattern is found for which the design codes do not provide solutions. In these cases, the designer must rely on assumptions or very case-specific literature. The paper proposes a general formulation to obtain the equivalent moment factors for any load case. These moment factors can be used for both slender rectangular sections and I-section beams loaded at the shear center. The beams are supported at both ends by fork supports. The fork support prevents lateral displacement and twisting at the ends of the beams and allows for lateral bending. In the paper, an energy method is used to determine the general formulation. The strain and potential energy before and after bending are calculated. The result is an

expression with five coefficients that depend on the load case. This formulation can be applied to at least twenty different load cases. With this formulation, it is also possible to combine different load cases into one load case.

In the work of Ozbasaran [43] a formula is proposed for cantilever I-beams. The formula is

$$P_{cr} = \frac{K_b}{C_k} E \left(\frac{t_f^2}{h} \right)^2, \quad (14)$$

and in this formula two coefficients are used, a dimensionless factor K_b depending on the section properties and loading case and a slenderness ratio C_k . The slenderness ratio is calculated using

$$C_k = \left(\frac{L t_f}{h b} \right)^2. \quad (15)$$

Factor K_b depends on the loading case and on C_k . In the paper five load cases are described; an applied end-force, a distributed force, a distributed force + an applied force halfway the beam, a distributed force + an end-point force and an applied moment. Also, two types of I-beams are taken into account which is commonly used in industry; IPE (beam with straight flanges) and IPN (beam with more curved and tapered flanges). For the IPN beam and an applied end-force, the expression for K_b is

$$K_b = 0.61 C_k^{-0.56} + 1.04 C_k^{-0.05}. \quad (16)$$

Numerical. There are several numerical methods available for calculating the critical load for LTB. In the work of Wijaya et al. [44] a FEA is used for this calculation. In this FEA shell elements are used to describe the I-beams. Every node has six degrees of freedom, three translations and three rotations. The focus of this study is on cantilever beams, where one of the ends of the beam is fixed and the other is free. Two load cases are considered: a point load at the end of the beam and a uniformly distributed load. For the analysis, a buckling analysis in an SAP program is used. The results are compared with analytical results for some variations in the cross-section and lengths of the beam.

In the subsection of empirical methods, the experiments in the paper of Demirhan et al. [31] are already mentioned. The results of these experiments are compared to the results of a numerical calculation. The numerical method in this paper consists of two steps. In the first step, the elastic critical buckling loads and the corresponding buckling mode shapes are determined. A non-linear load-displacement analysis, including geometrical and material non-linearity, is performed in the second step. The method used in this second step is called the Riks method and is a post-buckling method. The numerical analysis is performed in ABAQUS software. To model the cantilever beams, thin-shell elements (S8R5) are used. S8R5 is a shell element with eight nodes and five degrees of freedom per node. In the first step of the analysis, a linear-elastic material model is used. Using this numerical analysis the critical load for LTB, the von Mises stress distributions and buckling mode shapes are determined. An example of a

resulting figure obtained from this numerical analysis is shown in Figure 16 where one of the models is shown in the buckled state.

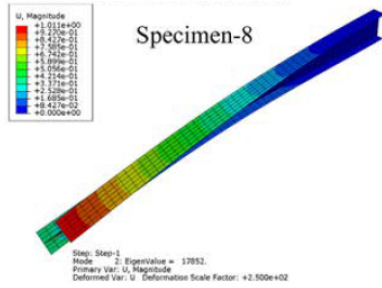


Fig. 16. Mode shape obtained from numerical analysis [31].

In the analytical method, subsection a paper for the calculation of the critical load for a beam restrained against warping at the supports is already described [40]. In this study, a numerical analysis is performed to verify the results of the analytical calculations. One of the methods used is a free software program called LTBeam. The user must provide the beam properties, boundary conditions and loading case. The software uses the provided information to calculate the critical load. The other method used in the study is a FEM analysis performed in ABAQUS. For this analysis volumetric elements (C3D8) are used. These elements have eight nodes and six degrees of freedom for each node. The computations are only performed in the elastic range of the beam.

In the work of Raftoyiannis, & Adamakos [38] a numerical calculation is used to verify the results of the proposed analytical analysis for web-tapered I-beams. The Algor FEA software is used to perform this analysis. A model consists of 1200 3-D oriented quadrilateral plate elements. A uniform load q is applied on the top flange and the beam is simply supported. An undeformed I-beam modelled in the software is shown in Figure 17.

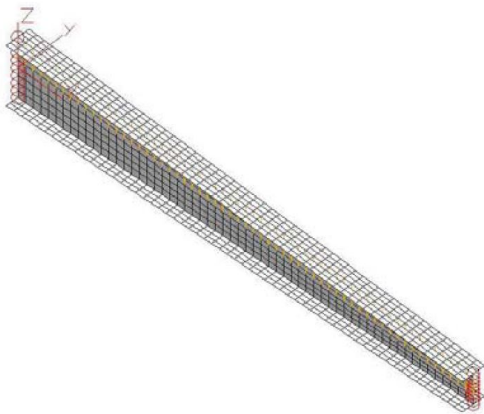


Fig. 17. FE model of a undeformed web-tapered I-beam [38].

A parametric study on the buckling load for LTB is conducted by Ozbasaran [43]. In this study, the influence of the length L , elasticity modulus E , section height h , flange width

w and flange thickness t_f on the buckling load is investigated. Using these parameters two coefficients are composed; a slenderness ratio C_k and a dimensionless coefficient K_b which depends on the loading case and section properties. The values of these coefficients varied in the study. The FEA is performed in ABAQUS. For this analysis S8R5 shell elements are used. This is a rectangular element with 8 nodes and 5 DoF at every node. To simplify the modelling the fillets between the flange and the web are neglected. It was found that these simplifications don't have a significant effect on the results. In this research four different load cases are taken into account; an applied moment, a distributed load, an applied force and a combination between an applied force and distributed load. One of the resulting plots is shown in Figure 18. In this plot, the critical moment is calculated for a varying slenderness ratio C_k . The results from the FEA (green dots) are compared with results from a presented formula.

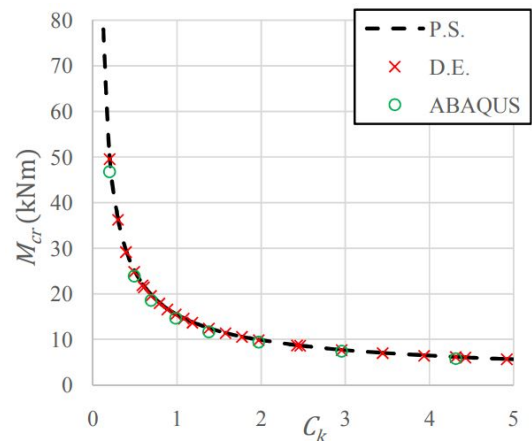


Fig. 18. Critical moment depending on slenderness ratio C_k [43].

C. Comparison

In this subsection, an overview of the found literature is presented and the calculation methods are compared to each other. In Table III all the found calculation methods are listed per category. The aim of this table is to give insight into the differences between the categories and how they score on each of the comparison criteria.

IV. DISCUSSION

The purpose of this literature review is to create an overview of the available calculation methods for the buckling behaviour of Euler buckling and lateral torsional buckling. In this section, the results from the found literature will be discussed.

The first discussion point is on the categorization used in this literature review. The two categories Euler buckling and lateral torsional buckling were well chosen, and no overlap between these categories was found. The other division in the categories; empirical, analytical and numerical was a bit more problematic. In many papers, a combination of these calculation methods is used. For example, a proposed analytical formula is verified by a FEA or experiments. Some of these

TABLE III
OVERVIEW OF THE FOUND CALCULATION METHODS FOR EULER BUCKLING AND LATERAL TORSIONAL BUCKLING.

Source	Category	Correctness	Computation time	Applicability	Difficulty
[17]	EB-E	+	-	--	+-
[18]	EB-E	+	-	--	+-
[19]	EB-E	+	-	--	+-
[20]	EB-E	+-	-	--	-
[15]	EB-A	+	++	-	+
[21]	EB-A	+	++	+-	+
[22]	EB-A	+	+	--	+-
[23]	EB-A	+	+-	-	+-
[24]	EB-A	+	+-	-	+-
[25]	EB-A	+	+-	+	+-
[26]	EB-A	+	+-	+	+-
[27]	EB-N	++	+-	+	+-
[28]	EB-N	+	+-	+-	+
[29]	EB-N	+	+	+-	+
[30]	EB-N	++	+-	+	+
[31]	LTB-E	-	-	--	+-
[32]	LTB-E	+	-	--	+-
[33]	LTB-E	+	-	--	+-
[34]	LTB-E	+	-	--	+-
[35]	LTB-E	+	-	-	+-
[15]	LTB-A	+	++	+-	+-
[36]	LTB-A	+	+	+	-
[37]	LTB-A	++	+-	++	-
[38]	LTB-A	+	+	+-	+-
[39]	LTB-A	+	+	+-	+-
[40]	LTB-A	+	+	+	+-
[41]	LTB-A	+	+	-	+
[42]	LTB-A	++	+	++	+-
[43]	LTB-A	+	+	+-	+-
[44]	LTB-N	++	+	-	+-
[31]	LTB-N	++	+	+	+-
[40]	LTB-N	+	+-	+	+
[38]	LTB-N	++	+	+-	+
[43]	LTB-N	++	+-	+	+

papers are used in multiple categories. This is only the case if the described calculation method can be used independently from any other methods from different categories.

The differences between calculation methods for the two buckling phenomena are also points for discussion. In general, Euler buckling is easier to understand and calculate. For Euler buckling the critical load can be calculated using a simple formula with a single effective length factor for different boundary conditions. The slenderness ratio is a guideline for the buckling behaviour that is used in many methods. The relatively simple formula is used as a starting point in some other methods focused on more specific cases. For example, an eccentric load, flexible fixation, model imperfections and Euler buckling in frames are topics discussed in the literature. For LTB the basic formula is more complicated and depends on many parameters and factors. In the easiest version, a single coefficient is used depending on a slenderness coefficient, but this formula can only be used for one specific load case. More elaborate formulas require multiple coefficients depending on load case and boundary conditions. Many of the proposed methods are focuses on reducing the weight of the beams, for example by using a web-tapered beam, adding holes in the

web or using a T-section beam instead of an I-section beam. This can be explained by the fact that LTB is mostly known in civil- and structural- engineering.

The next discussion point is the difference between the three calculation types. From Table III can be concluded that empirical methods score very low on computation time and applicability. The process of building a set-up, gathering materials and performing the experiments is very time-consuming. Also, the results from experiments can only be used in that very specific case of dimensions, boundary conditions, material and load case. Therefore, these methods are in most cases used to verify results from an analytical or numerical method. When the analytical and numerical methods are compared it can be concluded that the numerical methods score slightly higher on correctness and applicability. This can be explained by the fact that in most analytical formulas some coefficients are used that are only valid for a certain range of parameters or a specific load case. A FEA is more flexible and it is also possible to include imperfections or expand to the analysis of more complicated problems. However, the numerical methods score a bit lower on computation time and difficulty. In most cases, it requires some time to build the model for a FEA

and it is often more complicated because of all the modelling possibilities that are available.

The focus of found literature on LTB is on relatively large beams made of steel. This was already explained by the engineering field where LTB is used. In all these papers LTB is considered to be a failure mode and must be avoided. The beams deform plastically just beyond the critical load due to the relatively low maximum strain of the used materials. When different materials are used, for example, plastics or high-strength metals, with a higher allowable strain the buckling of the beam remains within the elastic domain. This could be used in a compliant mechanism to obtain zero-stiffness or bistable behaviour.

V. CONCLUSION

This literature review is conducted in order to investigate the possibility of using LTB in a compliant mechanism as an alternative to Euler buckling. Therefore it is desired to get an overview of the available calculation methods for both buckling phenomena. In total 34 papers with different calculation methods are found and the relevant information in these papers is discussed. A categorization is made between these papers and the methods are compared to each other using comparison criteria. The results are discussed to indicate the differences and similarities between the buckling phenomena and calculation methods. It can be concluded that lateral torsional buckling can be used to create zero-stiffness compliant mechanisms. This can be done as long as a correct combination of geometry and material properties is used such that the mechanism deforms only elastically.

REFERENCES

- [1] S. Jagtap, B. Deshmukh, and S. Pardeshi, "Applications of compliant mechanism in today's world—a review," in *Journal of Physics: Conference Series*, vol. 1969, no. 1. IOP Publishing, 2021, p. 012013.
- [2] M. d. C. Sanchez-Villamañan, J. Gonzalez-Vargas, D. Torricelli, J. C. Moreno, and J. L. Pons, "Compliant lower limb exoskeletons: a comprehensive review on mechanical design principles," *Journal of neuroengineering and rehabilitation*, vol. 16, no. 1, pp. 1–16, 2019.
- [3] L. L. Howell, "Compliant mechanisms," in *21st century kinematics*. Springer, 2013, pp. 189–216.
- [4] M. Schenk and S. D. Guest, "On zero stiffness," *Proceedings of the Institution of Mechanical Engineers, Part C: Journal of Mechanical Engineering Science*, vol. 228, no. 10, pp. 1701–1714, 2014.
- [5] M. I. Hamakareem, "Euler's theory of column buckling," Jan 2020. [Online]. Available: <https://theconstructor.org/structural-engg/euler-theory-column-buckling/37341/>
- [6] J. Van Eijk, "On the design of plate-spring mechanisms," 1985.
- [7] T. Liu, S. Bi, Y. Yao, Z. Dong, Q. Yang, and L. Liu, "Research on zero-stiffness flexure hinge (zsfh) based on spring four-bar linkage (4bsl)," *Mechanism and Machine Theory*, vol. 143, p. 103633, 2020.
- [8] C.-W. Hou and C.-C. Lan, "Functional joint mechanisms with constant-torque outputs," *Mechanism and Machine Theory*, vol. 62, pp. 166–181, 2013.
- [9] P. Liu and P. Yan, "A modified pseudo-rigid-body modeling approach for compliant mechanisms with fixed-guided beam flexures," *Mechanical Sciences*, vol. 8, pp. 359–368, 12 2017.
- [10] P. G. Opdahl, B. D. Jensen, and L. L. Howell, "An investigation into compliant bistable mechanisms," in *International Design Engineering Technical Conferences and Computers and Information in Engineering Conference*, vol. 80319. American Society of Mechanical Engineers, 1998, p. V01BT01A046.
- [11] G. Chen, Y. Gou, and L. Yang, "Research on multistable compliant mechanisms: The state of the art," *Proceedings of the 9th International Conference on Frontiers of Design and Manufacturing (ICFDM 2010)*, pp. 17–19, 01 2010.
- [12] S. H. Venter *et al.*, "The effect of the adjacent span on the lateral-torsional buckling capacity of overhang beams," Ph.D. dissertation, University of Pretoria, 2017.
- [13] M. BRETTLER, "Lateral torsional buckling and slenderness," *New steel construction*, vol. 14, no. 9, 2006.
- [14] L. Prandtl, "Kipperscheinungen," *Ein Fall von instabilem elastischem Gleichgewicht. Inaugural Dissertation d. Phil. Fakultät, Sekt. IId. Ludwigs-Maximilians-Universität München*, 1899.
- [15] S. Timoshenko, J. Gere, and W. Prager, "Theory of elastic stability," *Journal of Applied Mechanics*, vol. 29, no. 1, p. 220, 1962.
- [16] I. Kalkan and S. Kartal, "Torsional rigidities of reinforced concrete beams subjected to elastic lateral torsional buckling," *International Journal of Civil and Environmental Engineering*, vol. 11, no. 7, pp. 969–972, 2017.
- [17] H. Ban, G. Shi, Y. Shi, and Y. Wang, "Overall buckling behavior of 460 mpa high strength steel columns: Experimental investigation and design method," *Journal of Constructional Steel Research*, vol. 74, pp. 140–150, 2012.
- [18] H. Ban, G. Shi, Y. Shi, and M. A. Bradford, "Experimental investigation of the overall buckling behaviour of 960 mpa high strength steel columns," *Journal of Constructional Steel Research*, vol. 88, pp. 256–266, 2013.
- [19] G. Shi, X. Jiang, W. Zhou, T.-M. Chan, and Y. Zhang, "Experimental study on column buckling of 420 mpa high strength steel welded circular tubes," *Journal of Constructional Steel Research*, vol. 100, pp. 71–81, 2014.
- [20] A. Luible and M. Crisinel, "Buckling strength of glass elements in compression," *Structural engineering international*, vol. 14, no. 2, pp. 120–125, 2004.
- [21] P. Qiao and J. Davalos, "Design of all-composite structures using fiber-reinforced polymer (frp) composites," in *Developments in fiber-reinforced polymer (FRP) composites for civil engineering*. Elsevier, 2013, pp. 469–508.
- [22] K. Cao, Y.-J. Guo, and J. Xu, "Buckling analysis of columns ended by rotation-stiffness spring hinges," *International journal of steel structures*, vol. 16, no. 1, pp. 1–9, 2016.
- [23] R. C. Hibbeler, *Mechanics of materials*. Pearson Educación, 2005.
- [24] "Column buckling." [Online]. Available: <https://mechanicalc.com/reference/column-buckling>
- [25] A. Webber, J. Orr, P. Shepherd, and K. Crothers, "The effective length of columns in multi-storey frames," *Engineering Structures*, vol. 102, pp. 132–143, 2015.
- [26] A. Slimani, F. Ammari, and R. Adman, "The effective length factor of columns in unsymmetrical frames asymmetrically loaded," *Asian Journal of Civil Engineering*, vol. 19, no. 4, pp. 487–499, 2018.
- [27] P. R. Desai and C. Satish, "Effect of slenderness ratio on euler critical load for elastic columns with ansys," *Int. J. Eng. Res. Appl*, vol. 8, no. 5-III, pp. 40–43, 2018.
- [28] K. Yazdchi and A. Gowhari Anaraki, "Carrying capacity of edge-cracked columns under concentric vertical loads," *Acta mechanica*, vol. 198, no. 1, pp. 1–19, 2008.
- [29] G. Shi, Z. Liu, H. Ban, Y. Zhang, Y. Shi, and Y. Wang, "Tests and finite element analysis on the local buckling of 420 mpa

- steel equal angle columns under axial compression,” *Steel & Composite structures*, vol. 12, no. 1, pp. 31–51, 2012.
- [30] Y. Zhao, X. Zhai, and J. Wang, “Buckling behaviors and ultimate strengths of 6082-t6 aluminum alloy columns under eccentric compression—part i: Experiments and finite element modeling,” *Thin-Walled Structures*, vol. 143, p. 106207, 2019.
- [31] A. L. Demirhan, H. E. Eroğlu, E. O. Mutlu, T. Yılmaz, and Ö. Anil, “Experimental and numerical evaluation of inelastic lateral-torsional buckling of i-section cantilevers,” *Journal of Constructional Steel Research*, vol. 168, p. 105991, 2020.
- [32] J. Mottram, “Lateral-torsional buckling of a pultruded i-beam,” *Composites*, vol. 23, no. 2, pp. 81–92, 1992.
- [33] R. A. Bhat and L. M. Gupta, “Moment-gradient factor for perforated cellular steel beams under lateral torsional buckling,” *Arabian Journal for Science and Engineering*, vol. 45, no. 10, pp. 8727–8743, 2020.
- [34] M. Fortan and B. Rossi, “Lateral torsional buckling of welded stainless steel i-profile beams: experimental study,” *Journal of Structural Engineering*, vol. 147, no. 3, p. 04020342, 2021.
- [35] J. Jankowska-Sandberg and J. Kołodziej, “Experimental study of steel truss lateral–torsional buckling,” *Engineering Structures*, vol. 46, pp. 165–172, 2013.
- [36] A. Andrade, D. Camotim, and P. P. e Costa, “On the evaluation of elastic critical moments in doubly and singly symmetric i-section cantilevers,” *Journal of Constructional Steel Research*, vol. 63, no. 7, pp. 894–908, 2007.
- [37] C. H. Yoo and S. Lee, *Stability of structures: principles and applications*. Elsevier, 2011.
- [38] I. G. Raftoyiannis and T. Adamakos, “Critical lateral-torsional buckling moments of steel web-tapered i-beams,” *The Open Construction and Building Technology Journal*, vol. 4, no. 1, 2010.
- [39] W.-b. Yuan, B. Kim, and C.-y. Chen, “Lateral–torsional buckling of steel web tapered tee-section cantilevers,” *Journal of Constructional Steel Research*, vol. 87, pp. 31–37, 2013.
- [40] R. Piotrowski and A. Szychowski, “Lateral-torsional buckling of beams elastically restrained against warping at supports,” *Archives of Civil Engineering*, vol. 61, no. 4, pp. 155–174, 2015.
- [41] N. Challamel and C. M. Wang, “Exact lateral–torsional buckling solutions for cantilevered beams subjected to intermediate and end transverse point loads,” *Thin-Walled Structures*, vol. 48, no. 1, pp. 71–76, 2010.
- [42] D. Bresser, G. Ravenshorst, and P. Hoogenboom, “General formulation of equivalent moment factor for elastic lateral torsional buckling of slender rectangular sections and i-sections,” *Engineering Structures*, vol. 207, p. 110230, 2020.
- [43] H. Ozbasaran, “A parametric study on lateral torsional buckling of european ipn and ipe cantilevers,” *International Journal of Civil, Architectural, Structural and Construction Engineering, World Academy of Science, Engineering and Technology*, vol. 8, no. 7, 2014.
- [44] P. K. Wijaya *et al.*, “Elastic lateral torsional buckling of cantilever i beam,” 2013.
- [45] London:BSI. (2005) Bs en 1993-1-1, eurocode 3: design of steel structures: Part 1-1: general rules and rules for buildings.
- [46] A. Chajes, *Principles of structural stability theory*. Prentice Hall, 1974.
- [47] C. Wang, C. Wang, and I. Nazmul, “Stability criteria for euler columns with intermediate and end axial loads,” *Journal of engineering mechanics*, vol. 129, no. 4, pp. 468–472, 2003.

3

Research paper

Lateral torsional buckling in translational and rotational compliant joints to obtain zero-stiffness behaviour

Marco Moerman

Abstract—Compliant mechanisms are a popular alternative to conventional mechanisms consisting of multiple parts. Mass reduction, no backlash, no friction and less maintenance are some of the advantages of the use of compliant mechanisms. However, there is also a major drawback; there is always some stiffness present in the desired direction of motion. The advantages of conventional and compliant mechanisms can be combined if the stiffness can be reduced or ideally removed, resulting in a zero-stiffness compliant mechanism. The stiffness can be removed if a preload is applied in the stiffest direction of a flexible beam. In the current design of most zero-stiffness compliant mechanisms, this working principle is based on Euler buckling. This work proposes a method to use lateral torsional buckling in translational and rotational compliant joints to obtain zero-stiffness behaviour. In an analytical analysis, the lateral torsional buckling of a single beam is determined. The translational and rotational joint are implemented in a finite element analysis (FEA) to investigate the zero-stiffness behaviour. Experiments on a prototype verify the results from the FEA. Additionally, a sensitivity analysis is carried out on the effect of the cross-sectional dimensions of the flexible beam on the zero-stiffness range. The translational joint has a zero-stiffness range of 28.8 mm, corresponding to 11.5% of the beam length, and the rotational joint has a zero-stiffness range of 26.4°. From the sensitivity analysis, it is found that a rectangular cross-section has the best region of zero-stiffness.

Index Terms— Lateral torsional buckling, Euler buckling, zero-stiffness, neutral stability, compliant mechanisms, translational joint, rotational joint

I. INTRODUCTION

Compliant mechanisms can be used as an alternative to conventional mechanisms consisting of multiple parts. Compliant mechanisms use elastic deformation to achieve force and/or motion transmission. In conventional mechanisms, rigid parts are connected by joints to achieve force and/or motion transmission. The field of compliant mechanisms is a popular research subject because of the advantages over conventional mechanisms; less parts are needed to build the same mechanism resulting in light-weight mechanisms that require less maintenance, there is no friction or backlash and no lubrication is required [1, 2]. However, the use of compliant mechanisms has some drawbacks. The main challenge is that external work is required to elastically deform the mechanism [3], i.e. the mechanism has a certain stiffness. However, with the right combination of geometry, stiffness and prestress the stiffness can be reduced or even removed to create a zero-stiffness mechanism [4].

Over the years all kinds of compliant joints have been designed, which can be divided into 2D and 3D mechanisms [5, 6]. Also, a distinction can be made in the type of joint; translational joints [7–9], rotational joints [10, 11] and joints that have both translational and rotational freedom [10]. A large part of the research on compliant mechanisms is focused on making compliant joints with zero-stiffness behaviour [12, 13]. One way to do this is to make use of leaf springs that are preloaded in their stiffest direction. By applying the preload the bending stiffness is reduced. At a certain preload, the bending stiffness approaches zero, and zero-stiffness (or neutral stability) is obtained [14, 15]. The principle of applying a preload in the stiffest direction of the leaf spring is based on Euler buckling [16]. The preload at which the bending stiffness approaches zero is related to

the critical load for Euler buckling [17]. By applying a load that is beyond the critical load, bistable behaviour can be obtained. In this situation the mechanism has an unstable equilibrium at the point that was neutrally stable for the critical load and two stable equilibrium states [18, 19].

Next to Euler buckling, there are also other types of buckling. One of these types is lateral torsional buckling (LTB). This type of buckling occurs typically for slender beams with open cross-sections [20]. This specific type of beam, slender with open cross-sections, is mostly known in civil and structural engineering where it is used to achieve mass reduction. A commonly used type of beam in LTB research is an I-beam. Due to the static nature of civil and structural engineering, LTB is an undesired phenomenon and is considered to be a failure mode [21]. In Figure 1 a drawing is provided of the unloaded and loaded state for LTB of an I-beam. LTB occurs when a transverse load (in positive z direction) is applied to the I-beam. Similar to Euler buckling, the load is applied in the stiffest bending direction. The load results in compression of the bottom flange and tension of the top flange. When the load is increased to a certain critical load the combination of compression and tension results in an instability of the beam. The instability causes the I-beam to deflect laterally (denoted by u) and rotate (α) at the same time [22, 23].

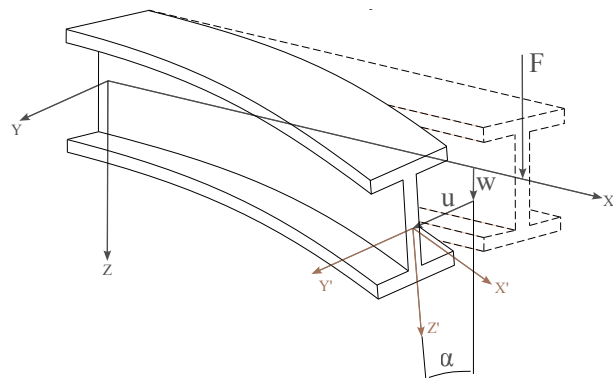


Fig. 1: Unloaded and loaded configuration for lateral torsional buckling of an I-beam. A force F is applied, and when lateral torsional buckling occurs the deformed beam has a lateral displacement u and a rotation α . The vertical displacement is w .

In current literature, lateral torsional buckling is not considered to be a possible working principle to create zero-stiffness compliant joints. The objective of this work is to examine the possibility of making a zero-stiffness compliant joint with lateral torsional buckling as a working principle. Due to the similarities between the buckling behaviour of Euler buckling and LTB, this could be a promising alternative to create zero-stiffness compliant mechanisms. The focus of this research is on two types of joints; a translational joint (TJ) and a rotational joint (RJ). A method is proposed to analyse these mechanisms analytically and in a finite element analysis (FEA). The results of this proposed method are verified by an experimental setup that contains a prototype of the mechanisms. Additionally, a sensitivity analysis is performed on the design parameters to investigate their influence on the results. The focus of the sensitivity analysis is on maximizing the stroke of the zero-stiffness region of the mechanism. Lastly, the potential of using multiple mechanisms in series to increase the stroke of zero-stiffness behaviour is investigated.

The outline of this paper is as follows. In Section II, the used method is explained starting with a description of the concept followed by an analytical, numerical and experimental analysis of the designs. Section III presents the results of the simulations and experiments. Next, the results are discussed in Section IV, followed by the conclusion of the paper in Section V.

II. METHODS

In this section, the process of obtaining a mechanism with zero-stiffness behaviour using LTB is explained. First, in Section II-A, the concept that will be used is introduced. Next, in Section II-B, the mechanism is simplified to a single beam to explain the applied loads. An analytical analysis of the mechanisms is performed using this simplification. Next, the modelling of a numerical model in the form of a finite element analysis (FEA) in MATLAB[®] is discussed in Section II-C. Lastly, Section II-D elaborates on a prototype and the conducted experiments.

A. Concept

In this paper, the idea to use LTB to obtain zero-stiffness behaviour will be applied to two commonly used compliant mechanisms. In the first mechanism, see Figure 2a, a linear moving shuttle is connected to the ground by parallel flexible beams [7, 16]. The shuttle can move a distance y_d with respect to the neutral position. The second mechanism contains a joint that is often used in compliant mechanisms, namely a crossed flexure hinge [24, 25]. The flexible beams that connect the shuttle to the ground are not parallel but are crossed instead. This results in a mechanism with a rotational degree of freedom (DoF) with an angle ϕ as shown in Figure 2b. The mechanisms are based on the two principal movements in 2D, translation and rotation, and will be referred to as translational joint (TJ) and rotational joint (RJ) respectively.

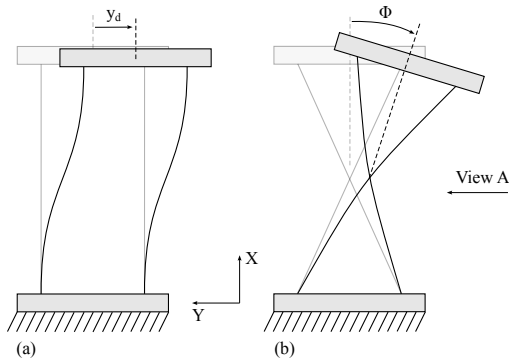


Fig. 2: (a) The translational joint (TJ) mechanism, (b) The rotational joint (RJ) mechanism. The black lines represent the flexible beams. The grey blocks represent the rigid parts.

In this research, I-beams will be used as flexible beams. A sideview of both mechanisms is provided in Figure 3. In this figure, a cross-section of one of the flexible beams is given to define the orientation of the I-beams. As discussed in Section I, an applied transverse load is required for LTB to occur. With the orientation used in the figure, this corresponds to a load in the z -direction. The transverse load is applied to the flexible beams by increasing the distance z_d . The flexible beams will move laterally in the y -direction when the transverse load is high enough for LTB to occur. For the analysis of the mechanisms the critical preload displacement and corresponding load are important to know. This will be determined in the next subsection of the analytical analysis. The formulas of the analytical analysis will be used in the numerical implementation of the mechanisms into a FEA. Next, a sensitivity analysis to find the optimal dimensions of the I-beams will be performed using the FEA. The results from the FEA will be verified by experiments on a prototype.

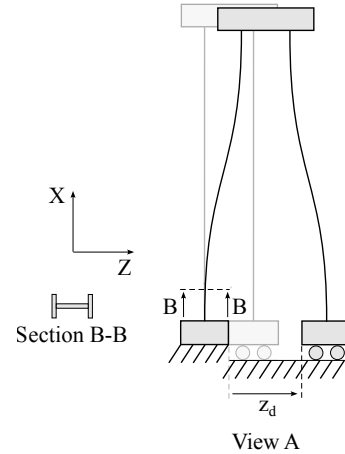


Fig. 3: Sideview of the two mechanisms including the orientation of the flexible beams and the preload displacement z_d .

B. Analytical analysis

As a starting point of the analytical analysis, a single beam of the mechanism will be considered in 2D. Figure 4a displays the load case and boundary conditions of the single beam. One end of the beam is fixed, i.e. the translations and rotation are constrained. On the other end, a transverse load is applied. The end of the beam is free to translate in both directions but rotation is constrained. In the figure also the beam in the deformed state, the Free Body Diagram (FBD), shear diagram and moment diagram of the beam are shown.

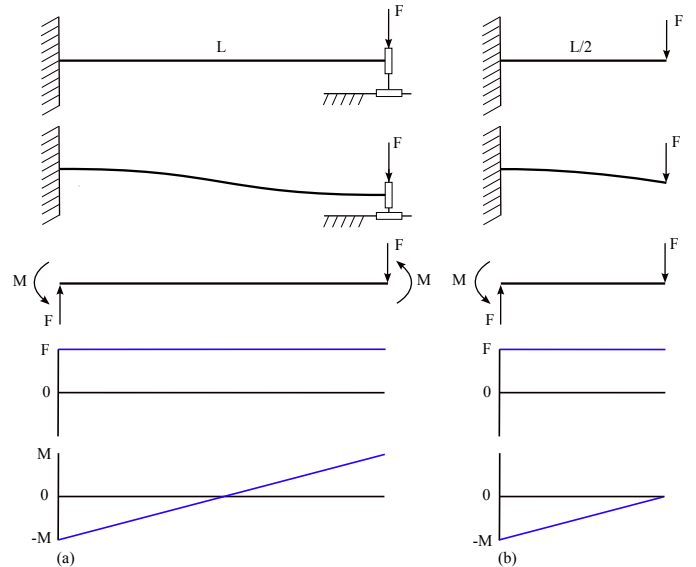


Fig. 4: (a) Single beam of the mechanism with an applied transverse load including deformed state, FBD, shear diagram and moment diagram, (b) Simplified cantilever including deformed state, FBD, shear diagram and moment diagram.

To the authors knowledge, no analytical models have been developed yet to calculate the critical load for these specific boundary conditions. A simplification of the model can be made to solve this problem. The moment diagram in Figure 4a is a straight line between M and $-M$. The value of M is given by the equation

$$\sum M_0 = -2M + FL = 0, \quad (1)$$

$$M = \frac{1}{2}FL.$$

Halfway the beam the moment is 0, as can be seen in the moment diagram. The first half of the moment diagram corresponds to that of a cantilever beam with only a transverse force at the free end of the beam. The simplified version of the beam is shown in Figure 4b. One end of the beam is again fixed, translations and rotation are constrained. However, the other end of the beam is free to translate and rotate. It's a cantilever beam of length $L/2$ with matching shear and moment diagrams to the first half of the beam with full length in Figure 4a.

The cantilever with an applied load at the free end is a commonly used load case in LTB problems. For the analytical analysis, the following considerations are taken into account; the cantilever beam is a doubly symmetric I-beam as shown in Figure 5. A cartesian reference coordinate system xyz is introduced such that, (i) the longitudinal axis of the beam is aligned with the x -axis, (ii) y and z are the major and minor central axis of the cross-section and (iii) the top flange of the beam corresponds to positive values of z . The shape of the cross-section is given by four parameters H, h, W, w . H is the height between the two flanges also known as the web height, h is the thickness of the top and the bottom flange, W is the width of the top and bottom flange and w is the thickness of the web. The length of the beam is defined as L_c , this corresponds to the length of the cantilever $L/2$ in Figure 4b.

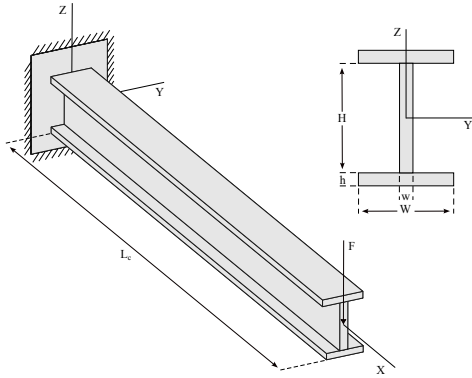


Fig. 5: Cantilever beam with applied end-point load and cross-section of the I-beam with relevant dimensions.

As discussed in Section II-A the transverse load on the beam is applied by the preload displacement z_d . Therefore, it is required to know the critical distance $z_{d,cr}$ at which LTB occurs. The critical distance is

$$z_{d,cr} = \frac{F_{cr} L_c^3}{3EI_{yy}}, \quad (2)$$

which is the deflection formula for bending of a cantilever beam [26]. Next to the Young's modulus E and second moment of inertia I_{yy} the critical force F_{cr} is required to calculate the deflection. The critical force is calculated by

$$F_{cr} = \frac{M_{cr}}{L_c}, \quad (3)$$

in which M_{cr} is the critical internal moment in the beam. As illustrated in 4b, the maximum internal moment is at the fixed end of the beam. In order to calculate the critical moment M_{cr} for the cantilever beam the first step is to determine some of the mechanical quantities of the beam. Important quantities are the second moments of inertia about the y - and z -axis [26]. For an I-beam these second moments of inertia are

$$\begin{aligned} I_{yy} &= \frac{1}{12} w H^3 + \frac{2}{12} W h^3 + \frac{2}{4} h W (H + h)^2, \\ I_{zz} &= \frac{1}{12} H w^3 + \frac{2}{12} h W^3. \end{aligned} \quad (4)$$

Together with the Young's modulus E , the second moments of inertia form the flexural rigidities EI_{yy} and EI_{zz} of the beam [27]. Also, the St. Venant torsional constant is required for the

calculations. This constant is a measure of the resistance of the beam to pure torsion [28]. The equation to calculate the St. Venant torsional constant is

$$J = \frac{2}{3} W h^3 + \frac{1}{3} H w^3. \quad (5)$$

Together with the Shear modulus G , the constant forms the torsional rigidity GJ . Formulas to calculate the critical moment have been formulation for a large variety of load cases and boundary conditions [22, 29–32]. For a doubly-symmetric cantilever beam with a load at the free end, which will be used in this work, the formula is

$$M_{cr} = C_1 \frac{\pi^2 EI_{zz}}{(k_z L_c)^2} \sqrt{\left(\frac{k_z}{k_w}\right)^2 \frac{I_w}{I_{zz}} + \frac{(k_z L_c)^2 GJ}{\pi^2 EI_{zz}}}, \quad (6)$$

which uses a few additional parameters [23]. I_w is the warping constant and is defined as

$$I_w = \frac{1}{4} I_{zz} h_s^2, \quad (7)$$

parameter h_s is the distance between the centers of the two flanges and is defined as $h_s = H + h$. Coefficients k_z and k_w are effective length factors. k_z is associated with the rotations of the end of the beam about the z -axis and k_w with the restriction of warping of the end of the beam. In the case of a cantilever beam fixed values are assigned: $k_z = 2.0$ and $k_w = 1.0$. Coefficient C_1 depends on the load case and boundary conditions of the cantilever beam. For the used boundary conditions and load case the expression for C_1 is

$$C_1 = 2.462/\sqrt{1 + \bar{K}^2} + 2.383\bar{K}/\sqrt{1 + \bar{K}^2}. \quad (8)$$

To calculate C_1 a dimensionless parameter \bar{K} is used, which gives an indication of the slenderness of the cantilever beam. \bar{K} is calculated using

$$\bar{K} = \frac{\pi}{L_c} \sqrt{\frac{EI_{zz} h_s^2}{4GI_t}}. \quad (9)$$

A low value of \bar{K} means a long cantilever and compact cross-section. On the contrary, a high value of \bar{K} corresponds to a short cantilever with a slender cross-section.

The results from the analytical analysis of the cantilever beam are used to derive the critical load and corresponding deflection for the beam with full length shown in Figure 4a. The critical load is the same for both situations and the deflection can simply be doubled. When this conclusion is expanded to the translational and rotational mechanisms the deflection doubles again (two beams in series as can be seen in Figure 3). The critical load is in this case also doubled because parallel beams are used as can be seen in Figure 2. Summarizing, using the results from the cantilever the critical distance has to be multiplied by four and the corresponding critical load is multiplied by two to calculate critical preload displacement $z_{d,cr}$ and critical force F_{cr} for the complete mechanism.

C. Numerical implementation

The derived formulas in the analytical analysis can be used to determine the critical deflection and corresponding load. However, the behaviour of the beam at or beyond the critical load is not included in the analysis. In this section, the implementation of the mechanisms into a FEA is described. For the FEA, an Euler-Bernoulli beam formulation is used based on the work of Battini [33]. The formulation uses geometrically non-linear co-rotational beam elements. The undeformed geometry is modelled by defining the coordinates of the nodes of the beam elements. For both mechanisms, the complete model of four beams is used in the FEA. The relevant dimensions to model the mechanisms are shown in Figure 6. The used values for these parameters and the cross-section dimensions are provided in Table I. The table includes a value for the length of the beams of the rotational joint. This value is defined by d_1 and α but gives an idea of how the length of the beams compares to the length of the beams of the translational joint.

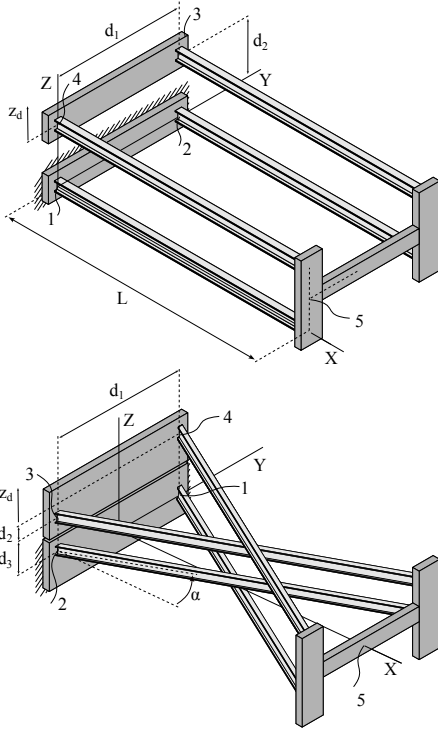


Fig. 6: Overview of the translational joint (TJ) and rotational joint (RJ) with the relevant dimensions and nodes for modelling.

TABLE I: Dimensions of the two mechanisms for FEA and experiments.

Translational Joint (TJ)		Rotational Joint (RJ)	
H	4.15 mm	H	4.15 mm
W	3.50 mm	W	3.50 mm
h	1.45 mm	h	1.45 mm
w	0.80 mm	w	0.80 mm
d ₁	100 mm	d ₁	80 mm
-	-	α	25°
L	250 mm	L	189 mm
d ₂	20 mm	d ₂	20 mm
-	-	d ₃	25 mm

In the FEA every beam consists of 20 beam elements. After defining the coordinates, the connections between the nodes are assigned. For the analysis, the second moments of inertia I_{yy} , I_{zz} , cross-section area A and St. Venant torsional constant J are required. Additionally, the material properties, the Young's modulus E and the Shear modulus G , are required. Imperfections in the dimensions and material of the beam can result in differences between the simulations and experiments. Therefore, a number of material tests were carried out on the beams that will be used in the experiments. A tensile test is performed to determine the axial rigidity EA of the beam. Two three-point bending tests were performed to obtain the flexural rigidities EI_{yy} and EI_{zz} . Lastly, a torsion test is performed to determine the torsional rigidity GJ of the material. The results of these material tests are implemented in the FEA. Using the rigidities directly, instead of measuring the material and cross-sectional properties separately minimizes the effects of material and dimensional imperfections. This ensures better results for the final experiments that will be conducted. In the FEA the cross-section of the rigid part is modelled the same as the beam elements. For these rigid parts, E and G are multiplied by a factor thousand to increase their stiffness.

Next, the boundary conditions are defined. In a 3D model, a node has 6 DoF; 3 translations and 3 rotations. In Figure 6 a few nodes are indicated with numbers. Nodes 1 and 2 are always fully constrained in both models, the values for the other nodes depend on the loading

step. An overview of the different loading steps in the FEA is shown in Figure 7. The influence of gravity was neglected in the analysis. For clarification, stills from the FEA are shown in Figure 8. The figures show the positions of the translational joint before and after each loading step. For both mechanisms, the first step is a displacement y_d in lateral direction (negative y) applied on node 5 followed by the applied preload in form of a displacement z_d in positive z direction on nodes 3 and 4. During the third step, a positive lateral displacement $2y_d$ is applied on node 5. The reaction force to the displacement is calculated which will be used to analyse the lateral stiffness of the mechanism.

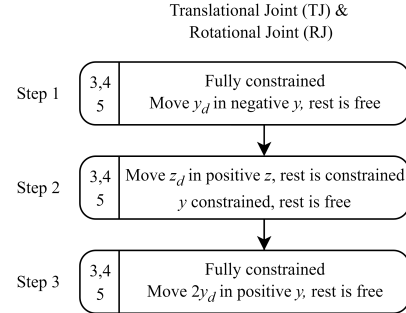


Fig. 7: Loading steps for a single analysis of the mechanisms. Nodes 1 and 2 are always fully constrained. Displacements for nodes 3, 4 and 5 are provided for each loading step.

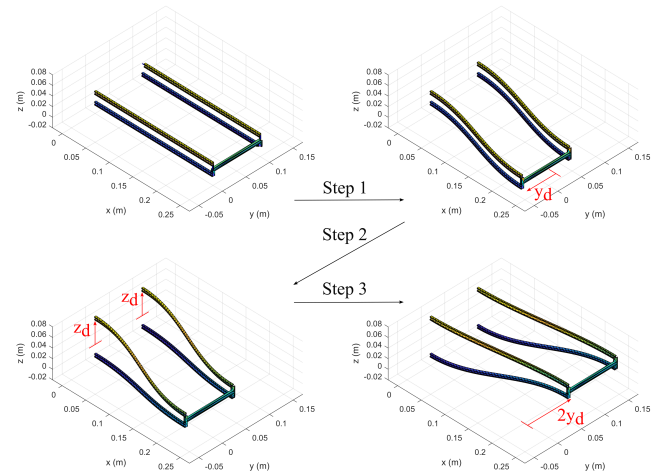


Fig. 8: Stills from the FEA to illustrate the loading steps. Step 1 is a lateral displacement y_d in $-y$. Step 2 is the applied preload displacement z_d in $+z$. Step 3 is a lateral displacement $2y_d$ in $+y$.

The order of loading steps is chosen for better stability of the FEA. If the preload displacement z_d is used as the first step the FEA could have problems solving close to the critical distance $z_{d,cr}$ because this is the bifurcation point of the mechanism. By applying the lateral displacement first, this problem is solved. In the case of the RJ, it is also possible to apply a rotation and calculate the reaction moment to investigate the moment-angle characteristic. However, this introduced significant challenges in the experimental validation of the model. So, a displacement is applied in the RJ mechanism as well. The loading steps are applied in 50 substeps. For every substep, the displacements and reaction forces are saved. Next, this information is used to analyse the reaction forces and displacements.

The described FEA so far is combined into a single function. As an input for the function z_d , y_d , E , G and the dimensions of the mechanism are required. The output of the function is a file that contains all the information about the performed analysis.

The results from the analysis are used to generate a force-displacement plot. On the horizontal axis the lateral displacement and on the vertical axis the reaction force are displayed. The next step in the numerical analysis is determining the optimal preload displacement $z_{d,opt}$ for which the zero-stiffness region is the largest for a given set of dimensions of the mechanism. This process is explained below and Figure 9 is used as clarification.

- 1) First the analysis is performed with $z_d = 0$, resulting in the red line in Figure 9. The difference between the minimum and maximum reaction force is used as a reference. A bound on the reaction force RF_b is calculated by taking a percentage of the reference, for example, 5% as is used in Figure 9. Half the height of the green box corresponds to RF_b .
- 2) The region of zero-stiffness is calculated by taking the distance between the first point larger than $-RF_b$ and the last point smaller than RF_b . In the figure, this is illustrated by the width of the green box d_{zs} .
- 3) It is found that the maximum zero-stiffness region corresponds to the case where the distance between $+RF_b$ and the maximum value of the first half of the plot is minimal. A variable d_{obj} is defined as this distance.
- 4) An optimization step is performed to minimize d_{obj} for design variable z_d . For this step, the MALTAB[®] function *fminsearch* is used, which is a simplex search method [34]. As an initial starting point for z_d the result from Equation 2 is used.

At the end of this process, there is an optimal preload displacement $z_{d,opt}$ and a corresponding value for the zero-stiffness region d_{zs} for a given set of dimensions.

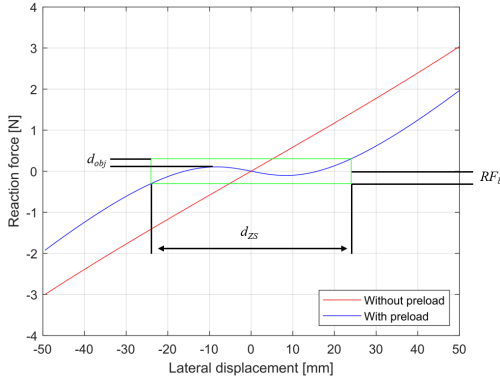


Fig. 9: Force-displacement plot with variables for preload optimization.

The resulting value for the zero-stiffness region d_{zs} is of particular interest. It can be used to investigate the influence of changing the dimensions of the mechanism. A sensitivity analysis in form of a grid search is performed to see how these changes in dimensions influence the zero-stiffness region d_{zs} . The grid search is performed three times, each time some of the variables are varied while the others are kept constant. An overview of the grid search is provided in Table II. The range of the grid search is given by the first two numbers. For example, for H in GS1, the range is 1 mm to 10 mm. The number between brackets is the used step size. In the first grid search (GS1), it is investigated how the size of the cross-section, defined by H and W , influences the region of zero stiffness d_{zs} . The other parameters are kept constant. The focus of the second grid search (GS2) is on the thickness of the flanges and the web, variables h and w respectively. Lastly, in the third grid search (GS3) the size of the cross-section and the thickness of the flanges are varied. In order to have two free variables, H and W are coupled by defining $W = 0.75H$ and h and w are coupled by keeping them equal to each other.

TABLE II: Values for the dimensional parameters in the grid search including the used step sizes between brackets.

	H [mm]	W [mm]	h [mm]	w [mm]	L [mm]
GS1	1:10 (0.3)	1:10 (0.3)	1	1	250
GS2	6	4	0.5:3 (0.1)	0.5:3 (0.1)	250
GS3	1:10 (0.3)	0.75·H	0.5:3 (0.1)	h	250

In the grid search, a constraint is taken into account to see if the set of parameters results in a feasible solution. For every set of parameters also the strain is calculated. For this calculation, the saved information from a simulation is used. For every node, the coordinates of the cross-section are determined using the undeformed coordinates, displacements and rotations of the model. For the four outer corners, where the strain will be the largest, the length of the element dL is estimated by a straight line between one of the corners on node n and on node $n+1$. The original length of the element dL_0 is defined by the length of an element in the undeformed state. These lengths are used in

$$\epsilon = \frac{dL - dL_0}{dL_0} \quad (10)$$

to calculate the strain. The maximum strain from the four outer corners is determined and saved. This procedure is repeated for all elements and finally, the maximum strain in the complete model is determined. The value of the strain is compared to the yield strain of the material. The yield strain can be calculated using Hooke's law

$$\epsilon_y = \frac{\sigma_y}{E}, \quad (11)$$

in which σ_y is the yield stress and E is the Young's modulus of the material [26]. In the grid search the same material is used as will be used in the experiments. This is polystyrene and this material has a yield strength varying from 5 MPa to 50 MPa [35]. In the analysis, a value of 30 MPa is used. For the Young's modulus, 2.1 GPa is used. With these material properties, the yield strain becomes 1.42%. The calculated strain and yield strain will be compared in the grid search as a constraint on the dimensional variables.

A second constraint is applied on the second moment of inertia I_{zz} . LTB occurs when bending is applied in the stiffest bending direction. To achieve this, the second moment of inertia about the horizontal axis I_{yy} must be larger than the second moment of inertia about the vertical axis I_{zz} . The FEA cannot find a solution when $I_{zz} > I_{yy}$ because LTB does not occur. Therefore, both I_{yy} and I_{zz} are calculated and when $I_{zz} > I_{yy}$ the region of zero-stiffness is not calculated and the grid search continues with the next set of parameters. The grid search is only performed on the translational joint because only the cross-sectional dimensions of the beam are taken into account. The results will be similar for the rotational joint because the focus of the sensitivity analysis was not on the dimensions of the used mechanism geometry. In order to save computation time a single beam is used instead of the four beams. In the model, at the free end of the beam, all rotations are constrained. The model has the same behaviour as the complete model with four beams.

Changing the dimensions of the mechanism is not the only possible solution for maximizing the zero-stiffness region d_{zs} . An interesting alternative is connecting multiple mechanisms in series with each other. It is expected that the distances d_{zs} of the individual mechanisms can be added together for the mechanism in series. This idea is tested on the TJ mechanism of which two mechanisms are connected in series. This mechanism will be referred to as the double translational joint (DTJ). An overview of the mechanism is provided in Figure 10. The mechanism has three moving shuttles (the I-shaped rigid parts) while the normal translational joint only has one. The important nodes are again provided in the overview. Node 5 is now a point on the shuttle in the middle, this is the shuttle with the largest displacements. For the mechanism, the same loading scheme in Figure 7 is used.

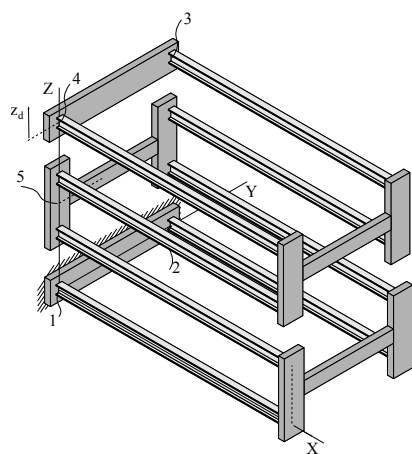


Fig. 10: Overview of the double translational joint (DTJ).

D. Experimental validation

A prototype is designed using SolidWorks for both mechanisms to validate the results from the numerical analysis. For the prototypes, the dimensions from Table I are used. The cross-section dimensions in this table correspond to the dimensions of the used Polystyrene I-beams in the experiments. The I-beams are off-the-shelf beams from MAQUETT of the type 414-55 [36]. The Young's modulus E of Polystyrene is 2.1 GPa and the Shear modulus $G = 0.8$ GPa, these material properties were provided by the manufacturer. The beams are connected with 3D-printed Poly-lactic Acid (PLA) rigid parts. In the rigid parts, rectangular holes are modelled with a clearance of +0.1 mm with respect to the outer cross-section dimensions. The clearance allows modular construction of the mechanism without the need for other types of fixation. The rigid parts are mounted on two XE25L300/M Thorlabs construction rails using M6 bolts. The SolidWorks designs of the two mechanisms are shown in Figure 11.



Fig. 11: Solidworks design of the TJ and RJ.

For the experiments, the setup consists of the construction rails mounted vertically on a Thorlabs breadboard. The lateral displacement is applied by a translational precision stage with a range of 100 mm (PI M-505.4DG [37]). The reaction force is measured by a load cell (Futek FSH03875 [38]). The mechanism is connected to the load cell using a fishing line. A fishing line is chosen because it is lightweight and stiff compared to the measured stiffness in the experiments. Additionally, it is used because a relatively large distance between the mechanism and the load cell is required. Over the range of motion, the application point on the mechanism has a small parasitic displacement in negative x direction. By setting a relatively large distance between the mechanism and the load cell any

undesired forces are minimized. On the other side of the mechanism, a mass of 500 gr is connected using a fishing line over a pulley in order to apply a constant pulling force on the sensor. This allows the sensor to measure a reaction force for both negative and positive displacements. The correct preload displacement for the mechanism is set using gauge blocks. An overview of the test setup is shown in Figure 12. The red lines in the picture represent the fishing line that is used to connect the precision stage to the mechanism and the mechanism to the mass. With white text, the relevant parts of the experimental setup are indicated.

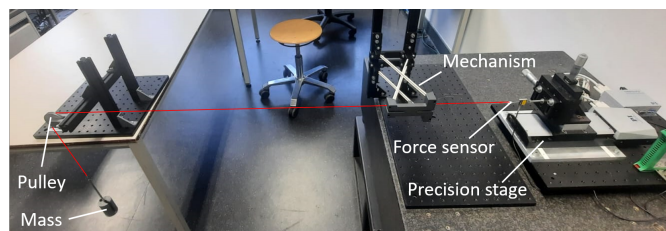


Fig. 12: Experimental setup; the precision stage with force sensor, the compliant mechanism and the mass connected to each other by a fishing line.

On both mechanisms, four experiments are conducted with different preload displacements. For each configuration, the experiment is conducted five times. One experiment consists of the lateral movement from -50 mm to 50 mm followed by the reverse movement. The results from the experiments are loaded into MATLAB[®] for comparison with the simulations. For each configuration, the mean of the five experiments is calculated and compared to the result of the simulation.

The utilized pulley is 3D-printed PLA and contains a steel bush in the center. The steel bush has a hole of 1.1 mm and is placed on a needle with a diameter of 1 mm. A small diameter minimizes the friction in the pulley. However, the presence of friction cannot be neglected. Therefore an experiment is conducted where the mechanism is removed and the mass is directly connected to the sensor. The precision stage performs a forward movement followed by a backward movement. The measured difference by the sensor gives an indication of the amount of friction introduced by the pulley.

A prototype is constructed for the double translational joint (DTJ), following the same procedure as described for the TJ and the RJ. The same type of experiments is carried out on this prototype as well. However, the experiment is carried out at two different preloads,

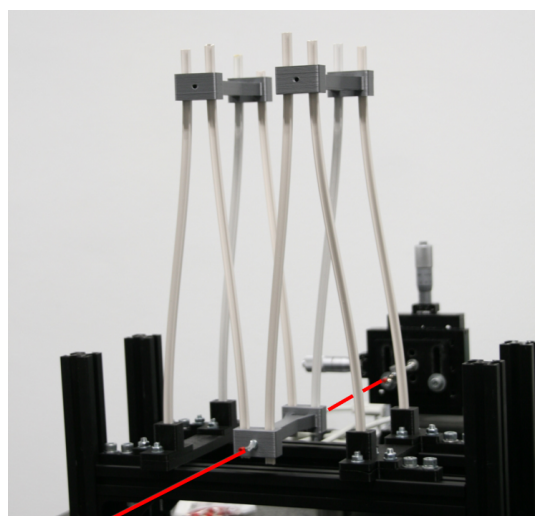


Fig. 13: Experimental setup for the double translational joint.

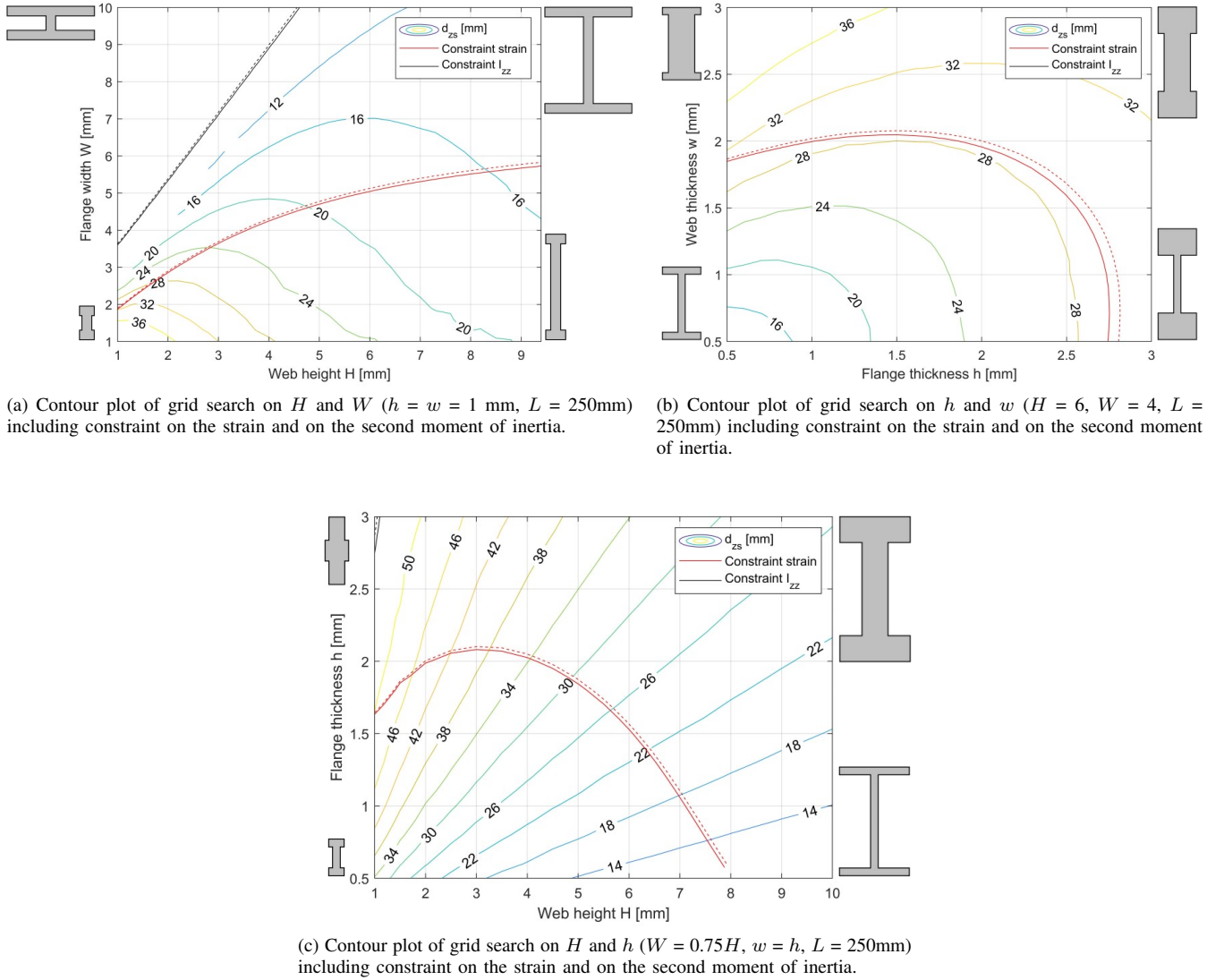


Fig. 14: Contour plots of the grid search on the cross-section dimensions of the I-beam. Contours give the obtained region of zero-stiffness d_{zs} . Constraints are used on the strain and the second moment of inertia I_{zz} . The dashed line indicates the infeasible region resulting from the constraint. In grey, the shape of the cross-section is provided for the area of design points close to that particular shape.

one without preload and one at the optimal preload for comparison with the single translational joint. The same testing procedure as described above is used. For this mechanism, a different orientation (beams vertical) is used in the experiments. In the original orientation (beams horizontal) the middle shuttle could touch the rigid parts which resulted in extra friction force in the measurements. A picture of the mechanism is provided in Figure 13. The mechanism is still connected to the mass by the fishing line but only the first part of the line is visible in the picture.

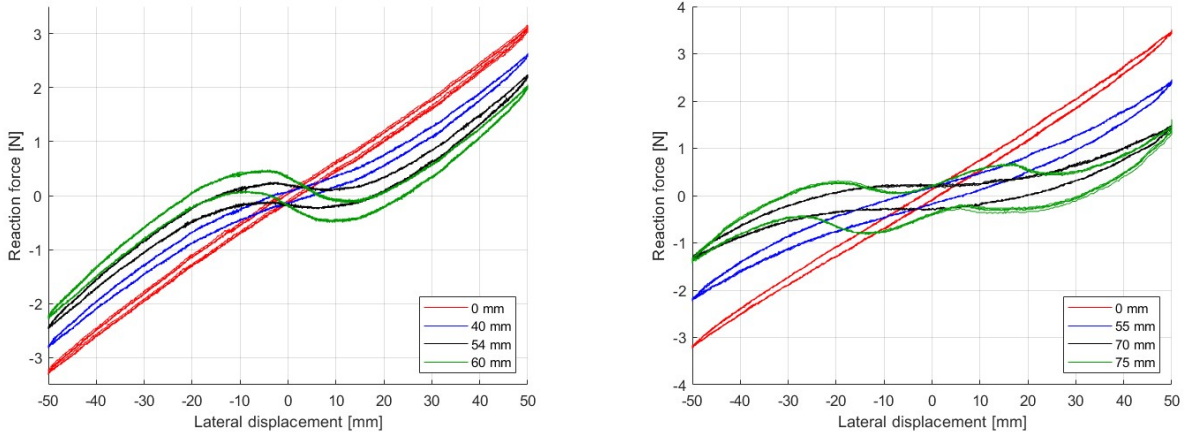
III. RESULTS

In this section, the results will be discussed. First, in Section III-A the results from the numerical analysis are provided. In Section III-B the results of the experiments and the comparison with the simulations are shown. Lastly, the results from the experiments of the double translational joint are provided in Section III-C.

A. Simulations

The FEA is used for a sensitivity analysis on the cross-sectional dimensions of the I-beam in the translational joint. The results from

the grid searches are provided in Figure 14. The grid search is performed three times, each time with a comparison between different parameters. The grey cross-sections are added to give some idea of the shape of the cross-section in that area of the grid search. For example, the top-left area of Figure 14a corresponds to wide, but low cross-sections. In the first contour plot, shown in Figure 14a, the results of the grid search on H and W (GS1) are visible. The values on the contour lines represent the region of zero-stiffness d_{zs} for the corresponding values for H and W . The remaining design parameters are kept constant; $h = w = 1$ mm and $L = 250$ mm. Additionally, two constraint lines are visible. The red line corresponds to the constraint considering the strain. The dashed red line indicates the infeasible region. Combinations of H and W at the side of the dashed line result in a strain exceeding the maximum allowed strain ϵ_y . For combinations of H and W at the dashed side of the black constraint, LTB does not occur because in these cases $I_{zz} > I_{yy}$. This can be explained by the relatively high values of the flange width W compared to the web height H . From the contour plot can be concluded that the region of zero-stiffness d_{zs} increases for decreasing values of H and W . The increasing values of the objective



(a) Raw data from the experiments on the translational joint with four different preloads.

(b) Raw data from the experiments on the rotational joints with four different preloads.

Fig. 15: Raw data from the experiments.

remain within the bounds of the constraints. However, the smallest value of 1 mm is chosen because the web and flange thickness, h and w , would otherwise be larger resulting in an infeasible geometry.

The results of the second grid search (GS2), on the thicknesses h and w , are provided in Figure 14b. Again the contour lines of the objective d_{zs} and the constraints are shown. Similar to the first grid search the remaining parameters are kept constant; $H = 6$ mm, $W = 4$ mm and $L = 250$ mm. Because $H > W$ there is no infeasible region for the constraint on the moments of inertia. This is the reason that the black constraint is not visible. The region right and above the red dashed line is infeasible because of the constraint on the strain. The contour lines show that the region of zero-stiffness is increasing for increasing values of the thicknesses h and w . It is also observed that the web thickness w is dominant with respect to the flange thickness h . The constraint on the strain limits the maximum achievable region of zero-stiffness.

In Figure 14c the results from the last grid search are shown. In this grid search, the size of the cross-section (H and W) is compared to the thickness of the flanges (h and w). On the axes of the plot, only H and h are visible. However, the other two parameters are not independent. A relation between the web height and flange width is defined by $W = 0.75H$. Similarly, the web thickness and flange thickness are related by $w = h$. Again, the length of the beam is kept constant; $L = 250$ mm. A very small piece of the black constraint is visible in the top-left corner. The shown domain is part of the feasible domain for this constraint because of $H > W$. The constraint on the strain limits the possible solutions to the bottom-left region. Similar to the first two plots, the highest values for d_{zs} are found for decreasing cross-section size (H and W) and increasing flange thicknesses (h and w).

B. Experiments

On the prototypes of the translational and rotational joint experiments are conducted to verify the results from the FEA. The raw measurement data from these experiments is shown for both mechanisms in Figure 15. In Figure 15a, the results are shown for four different preloads z_d on the translational joint. The figure contains the data of all five measurements for every preload. On the x-axis the lateral displacement in mm is shown, the range of -50 mm to +50 mm corresponds with the range of the translational precision stage. A single experiment is a forward motion followed by a backward motion. This results in a hysteresis loop consisting of two lines slightly above each other. On the y-axis, the measured reaction force by the force sensor is shown in newton [N]. In Figure 15b, the

measured data from the rotational joint is provided. The mean of the five experiments of each configuration is calculated for comparison with the results from the FEA.

For the translational joint, the comparison between simulation and experiments is shown in Figure 16. The figure consists of four sub-figures, each corresponding to a different preload for the translational joint. Every sub-figure is a force-displacement plot containing the results from the simulation and experiment for the same preload. Without a preload, the stiffness of the mechanism is constant while the reaction force is linear. With increasing preload the stiffness decreases and for the optimal preload $z_{d,opt}$ the zero-stiffness behaviour can be observed. If the mechanism has a preload beyond the optimal preload it becomes bistable and around the origin, negative stiffness is observed. In this simulation the bound on the reaction force RF_B is set on 1% which is in this case 0.0613 N. With the FEA a corresponding optimal preload of $z_{d,opt} = 53.6$ mm is found. For this preload, the region of zero-stiffness is 28.8 mm, this is 11.5% of the length of the beams. The prototype is tested on a slightly higher preload of 54 mm. Small differences are found between simulations and experiments for the preloads. The used values to obtain the figures are provided in Table III. Also, the corresponding values for the region of zero-stiffness d_{zs} are provided in this table.

TABLE III: Used preloads in simulations and experiments and resulting region of zero-stiffness d_{zs} of the translational joint.

Plot	Simulation z_d [mm]	Experiment z_d [mm]	d_{zs} [mm]
16a	0.0	0.0	1.9
16b	40.0	40.0	4.4
16c	53.6	54.0	28.8
16d	59.0	60.0	2.4

In Figure 17 the results from simulations and experiments are compared for the rotational joint. In Table IV the used preloads in the simulations and experiments and the resulting regions of zero-stiffness d_{zs} from the simulations are provided. From the simulations, an optimal preload $z_{d,opt}$ of 70.4 mm was found. The bound on the reaction force RF_b is 1%, which for this mechanism is 0.0646 N. The corresponding width of the zero-stiffness region is 40.9 mm. This corresponds to a rotation of $26.4^\circ (\pm 13.2^\circ)$ of the shuttle. Again the decreasing stiffness for increasing preload can be observed. However, the behaviour of the mechanism beyond the optimal preload $z_{d,opt}$ is different from the translational joint. The rotational joint does not show bistability but behaves more like a multistable mechanism instead. The difference between the simulation and experiment for

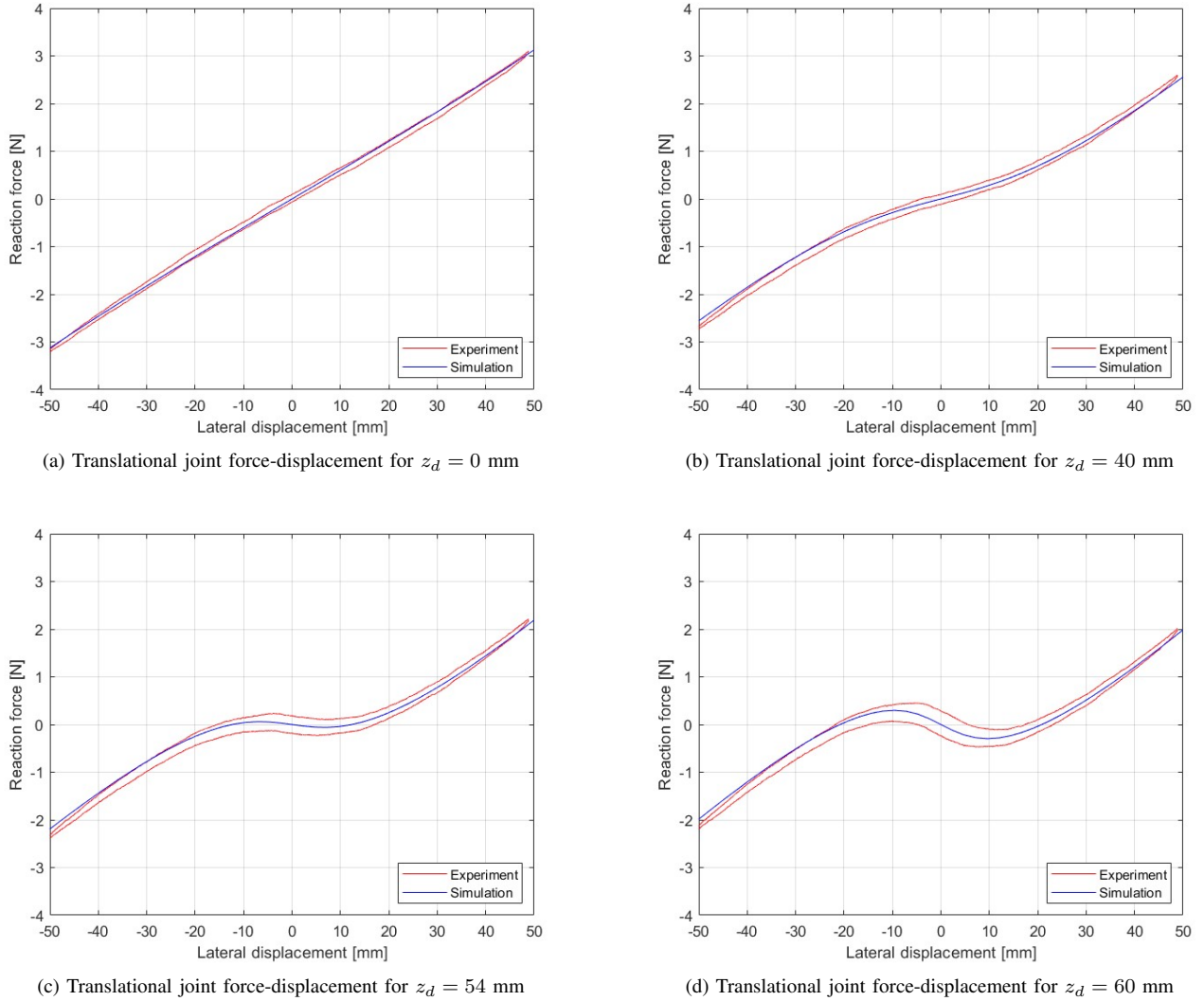


Fig. 16: Force-displacement plots of the translational joint for varying z_d . Results from the simulations and experiments.

this configuration is quite significant. The used preload and the shape of the plots show some differences.

TABLE IV: Used preloads in simulations and experiments and resulting region of zero-stiffness d_{zs} of the rotational joint.

Plot	Simulation z_d [mm]	Experiment z_d [mm]	d_{zs} [mm]
17a	0.0	0.0	1.9
17b	55.0	55.0	4.2
17c	70.4	71.0	40.9
17d	76.0	85.0	24.4

Also, an experiment on the friction force introduced by the pulley was conducted. From the experiment is found that the friction force is 0.05 N. This is the average of the friction force over the range of motion. The friction force is constant because the force applied on the pulley by the fishing line is also constant. The applied force depends only on the mass that is connected at the end of the fishing line. The determined friction force is part of the hysteresis that can be seen in the plots of the experiments.

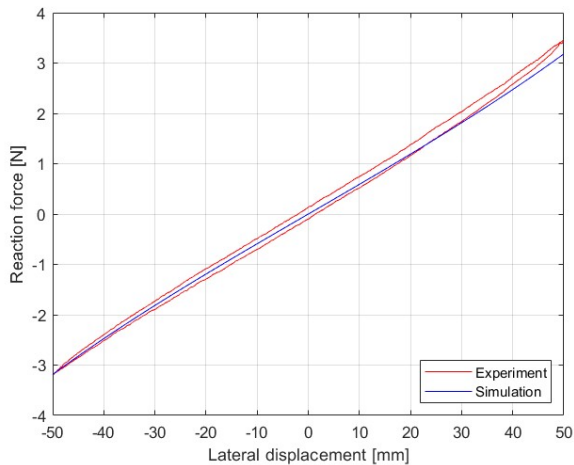
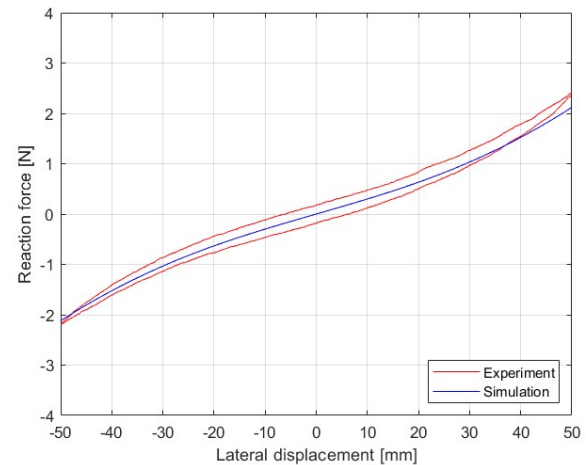
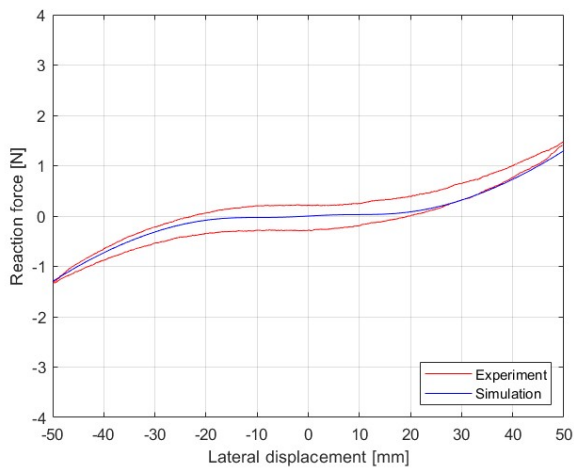
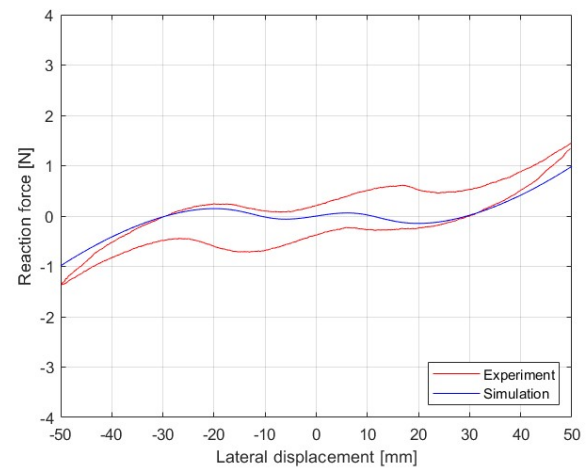
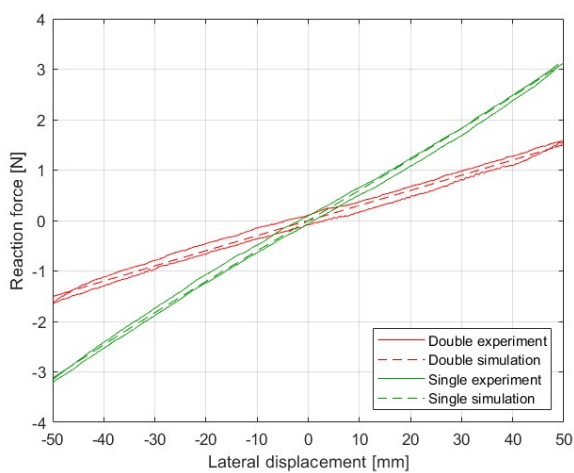
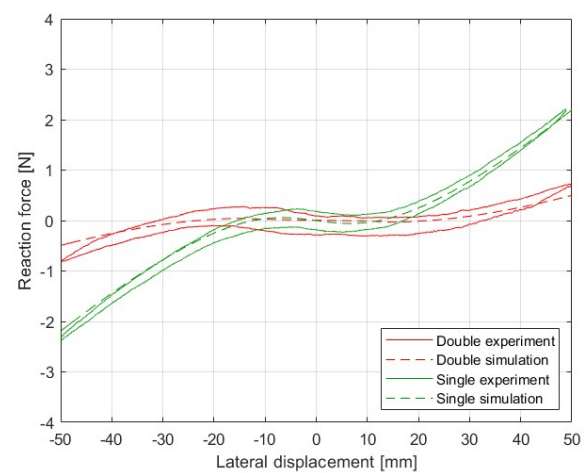
C. Double rotational joint

Lastly, experiments are conducted on the double translational joint to investigate the possibility of adding multiple mechanisms in series.

The results from these experiments are shown in Figure 18. The prototype is tested at no preload and at the optimal preload. Again, the results are compared with the simulations. For comparison, the results from the single translational joint are provided in the same figure. In both plots, the dashed lines represent the force-displacement behaviour from the simulations. From Figure 18a, it can be observed that the stiffness for the DTJ is approximately half the stiffness of the TJ. The used preloads in the simulations and experiments are shown in Table V. For the TJ the region of zero-stiffness was found to be 28.8 mm. For the DTJ the same settings of the FEA are used. For this mechanism, the region of zero-stiffness is 54.6 mm. This is 1.90 times higher than the region of zero-stiffness for the TJ. A good agreement is found between the results from simulations and experiments.

TABLE V: Used preloads in simulations and experiments and resulting region of zero-stiffness d_{zs} . A comparison between translational joint and double translational joint.

Plot	Simulation z_d [mm]	Experiment z_d [mm]	d_{zs} [mm]
18a-TJ	0.0	0.0	1.9
18b-TJ	53.6	54.0	28.8
18a-DTJ	0.0	0.0	3.8
18b-DTJ	100.4	100.0	54.6

(a) Rotational joint force-displacement $z_d = 0$ mm(b) Rotational joint force-displacement $z_d = 55$ mm(c) Rotational joint force-displacement $z_d = 70$ mm(d) Rotational joint force-displacement $z_d = 85$ mmFig. 17: Force-displacement plots of the rotational joint for varying z_d . Results from the simulations and experiments.(a) TJ and DTJ force displacement $z_d = 0$ mm.(b) TJ and DTJ force displacement at optimal preload; $z_{d,TJ} = 54$ mm and $z_{d,DTJ} = 100$ mmFig. 18: Force displacement of the TJ and DTJ for varying z_d . Results from the simulations and experiments.

IV. DISCUSSION

A. Sensitivity analysis

The subject of the first part of the discussion is the collection of results from the sensitivity analysis. The sensitivity analysis is performed to investigate the influence of the cross-section dimensions on the region of zero-stiffness d_{zs} . The length of the beam L is in all cases constant because increasing the length of the beam will always increase the region of zero-stiffness, which is trivial. In GS1, provided in Figure 14a, the influence of the web height H and the flange width W is investigated. The top-left region is not feasible because of the constraint on I_{zz} . When $I_{zz} > I_{yy}$ LTB does not occur. The FEA cannot find a valid solution for d_{zs} so this part of the contour plot is not calculated. In the bottom-right part of the contour plot of GS1 the contour lines show some non-smooth behaviour. This part of the grid search corresponds with a high, narrow cross-section with a small thickness. For the FEA it is hard to find the correct solution because, at the critical load, this type of cross-section has multiple buckling modes very close to each other. The beam has a low flexural rigidity EI_{zz} and a low torsional rigidity GJ [22]. The highest values for the objective d_{zs} are obtained for low values of H and W . This corresponds to a small, narrow cross-section. The constraint on the strain is not a limiting factor for these low values.

GS2 focuses on the influence of the web and flange thickness h and w . The shown contour plot in Figure 14b is completely within the feasible region of the constraint on I_{zz} . This is the case because of the chosen constant values $H = 6$ mm and $W = 4$ mm. The highest values of d_{zs} are found for increasing values of h and w . The constraint on the strain is in this case the limiting factor. The dashed line indicates the region where the strain exceeds the maximum allowable strain.

In GS3 the effect of the size of the cross-section (H and W) and the thickness of the web and flanges (h and w) is investigated. Since it is only possible to have two free variables in a 2D-contour plot, H and W are coupled by defining $W = 0.75H$ and h and w are coupled by defining $w = h$. Similar to GS2, the contour plot in Figure 14c is almost completely within the feasible region of the constraint on I_{zz} because W is relatively small compared to H . In accordance with GS1 and GS2, the highest values for d_{zs} are found for small values of H and W and high values of h and w . The maximum achievable d_{zs} is limited by the constraint on the strain.

An interesting conclusion can be drawn from these results. For small values of H and W combined with high values of h and w , the cross-section is no longer an I-beam. This can be explained using the definition of the cross-section in Figure 5. For example, if $H = W = 1$ mm and $h = w = 2$ mm are used, the shape of the cross-section becomes a plus-shape. The width of the web w is larger than the width of the flanges W and the height of the web H is smaller than the height of the flanges h . The situation where $H = W = h = w$ corresponds to a rectangular shape. It is expected that the rectangular shape results in the highest region of zero-stiffness d_{zs} . The flexural rigidity EI_{zz} is relatively low for this situation resulting in large lateral displacement at the critical load. However, the expression of the St Venant torsional constant J , provided in Equation 5, is only valid for a thin-walled I-section. To draw a more justified conclusion, it is recommended to use a general expression for the torsional constant that is accurate for all types of cross-sections. When this expectation is compared to what is known in literature about LTB this seems reasonable. As discussed in the introduction, LTB is mostly known in civil and structural engineering where LTB is an undesired phenomenon. In contrast to this research, where the goal is to utilize the elastic lateral torsional buckling behaviour. An I-section has better cross-sectional properties in the prevention of LTB and is therefore used in civil and structural engineering. A similarity is found between this result and obtaining zero-stiffness using Euler buckling. A rectangular cross-section (leaf-spring) has a lower resistance to Euler buckling than other types of cross-sections (for example an I-section). Leaf springs are in almost all cases used in compliant mechanisms to obtain zero-stiffness behaviour.

In the process to calculate the region of zero-stiffness, a bound on the reaction force RF_b is used. The mechanism is considered to have zero-stiffness as long as the reaction force remains within this bound. The goal is to maximize the region of zero-stiffness. Using a RF_b of 1% results in a significant reduction of the stiffness for this purpose and a slightly bistable mechanism has a larger region of quasi zero-stiffness. However, for other purposes, a higher reduction may be desired. For these purposes, a lower RF_b can be used in the same method. When the goal is to obtain actual zero-stiffness behaviour, RF_b should approach zero.

B. Experiments

Next, the results from the experiments and comparison with simulations for the translational joint and rotational joint will be discussed. In the FEA the rigidities EA , EI_{yy} , EI_{zz} and GJ are used instead of the separate material properties E and G and the cross-section properties A , I_{yy} , I_{zz} and J . To obtain the rigidities a tensile test, two three-point bending tests and a torsional test were conducted. The use of rigidities gives more accurate results because the material and geometric imperfections are averaged out in these tests. Material properties can vary from batch to batch. Additionally, time, temperature and UV light can have an effect on the properties of the material. The dimensions of the cross-section are determined using a calliper. This introduces measuring inaccuracy for the dimensions. Also, the fillet between the web and the flange is not taken into account in the formulas to determine the cross-section properties. The flanges are also slightly tapered, and h increases from the side of the flange towards the web. These imperfections together can have a significant effect on the cross-sectional properties and therefore also on the results of the FEA.

In Figure 15, the raw data from the experiments for the translational joint and rotational joint is shown. Each coloured line is a set of five repeated measurements. Because the deviation between the single measurements is small, the mean of the five measurements can be calculated for comparison with simulations. In the other plots, the calculated mean is always compared with the simulation.

For both mechanisms, similar behaviour is observed in Figures 16 and 17. Without preload, the lateral stiffness is linear. By increasing the preload, the stiffness decreases around the origin until for an optimal preload $z_{d,opt}$ the stiffness approaches zero. Beyond this preload, the translational joint becomes bistable resulting in a negative stiffness at the origin. For the rotational joint, the last configuration behaves differently. In Table IV the preloads for the simulations and experiments of the rotational joint are shown. For this configuration the preloads are 76 mm and 85 mm for the simulation and experiment respectively. In Figure 17d, can be seen that the result from the experiment has a similar shape when compared to the simulation. However, in the experiment, the reaction force increases slightly over the range of motion. During the experiment, it was observed that the four beams did not buckle at the same time. When travelling from left to right two of the beams always buckled before the other two. For the reverse motion, the other two beams buckled first. A possible explanation for this behaviour is imperfections in assembling the mechanism. Even the smallest differences in the length of the beams can result in a preferred position of the mechanism at the bifurcation point.

For the rotational mechanism, it was decided to investigate the force-displacement behaviour. However, it would make more sense to have a moment-angle characteristic for a rotational joint. Conducting experiments to obtain a moment-angle characteristic, however, would introduce all kinds of challenges. The center of rotation for a compliant rotational joint is not constant but drifts slightly [39]. This makes it difficult to apply a pure rotation on the mechanism. The most feasible option was to use the same test setup as for the translational joint. In Figure 6 the position of node 5, on which the lateral displacement y_d is applied, is chosen in the middle of the shuttle. This point has the least parasitic motion on the x -direction over the range of motion. However, the parasitic motion in x -direction

cannot be neglected. Also for the translational joint, a small motion in x -direction is present over the range of motion. A direct solid connection between the force sensor and mechanism was therefore not possible. Instead, a fishing line was used to connect the sensor and mechanism. This makes it possible to create a certain distance between the sensor and mechanism. For an increasing distance, the effect of the parasitic motion on the force measurement decreases. Between the sensor and mechanism, the space was limited, this can be seen in Figure 12. However, the available distance was enough to minimize the effects of the parasitic motion in x -direction. The rotational joint has the most parasitic motion, referred to as x_p . For a complete movement, this is 8.9 mm. The available distance between the sensor and mechanism L_s is 140 mm. For the experiments, the aim is to position the force sensor such that x_p is exactly divided into two. The amount of parasitic motion will be the same for the neutral position $y_d = 0$ mm and the outer positions $y_d = \pm 50$ mm. However, for the following calculation, the worst-case scenario is considered. With $x_p = 8.9$ mm and $L_s = 190$ mm the angle of the fishing line is 2.69° . For the rotational joint with $z_d = 0$ mm, this can result in a measurement error of 0.0035 N or 0.11%.

The translational joint and rotational joint were tested in an orientation with horizontal beams. An orientation with vertical beams would be better because the influence of gravity is less in that orientation. However, this was not possible because of the limited height of the precision stage, resulting in a situation where the force sensor and moving shuttle cannot be connected to each other in the correct way. Therefore, the horizontal orientation was chosen. The shuttle is made of 3D-printed PLA. By choosing a relatively low infill of the 3D-print and reducing the volume of the shuttle the mass is kept as low as possible. The effect of gravity is tested in the FEA by applying a gravitational force at the shuttle and comparing the results to a FEA without gravity. For the used mass of the shuttle, these effects are very low. Therefore, it is concluded that the translational and rotational joints can be tested in a horizontal orientation.

The plots of the experiments all consist of a forward and a reverse motion resulting in two lines. These lines form the hysteresis loop of the experiment. One of the sources of hysteresis is friction. For the forward motion, the measured force is slightly higher due to the friction force. For the reverse motion, the measured force is slightly lower. The pulley that is used to redirect the pulling force introduces friction to the measurements. The friction force of the pulley is determined by performing the experiment without the mechanism. The mass is directly connected to the force sensor by the fishing line. The found friction force is 0.05 N, so the contribution of friction to hysteresis is 0.1 N. The friction force is always the same, as long as the same weight is used.

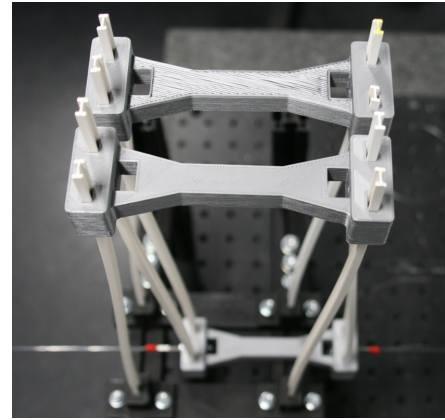
Friction is not the only source of hysteresis. From the plots can be concluded that the amount of hysteresis is increasing for an increasing preload displacement z_d . For example, in Figure 16 the force-displacement plots for the translational joint are shown. In the plot for $z_d = 0$ mm, the hysteresis is approximately 0.13 N. In the bistable configuration, $z_d = 60$ mm, the hysteresis is almost 0.5 N. The additional type of hysteresis is elastic hysteresis. During the movement of the mechanisms, part of the energy is dissipated as heat due to internal friction [40]. A preloaded mechanism has higher internal stresses which increase the internal friction. This explains the increasing hysteresis for an increasing preload displacement. In a typical hysteresis loop, the amount of hysteresis approaches zero at the ends of the movement and increases towards the middle. This effect is also visible in the plots of the experiments.

An important factor to take into account during the experiments is creep of the I-beams. Creep is a time-dependent permanent deformation. When stresses are present in the material for a long period of time due to a certain load the beams will deform [26]. For the prototypes used in the experiments, creep can occur when the preload displacement z_d is applied for a long period of time. When creep occurs and the beams are deformed permanently, this will change the behaviour of the mechanism. The amount of time needed for creep to occur depends on the stresses in the mechanism

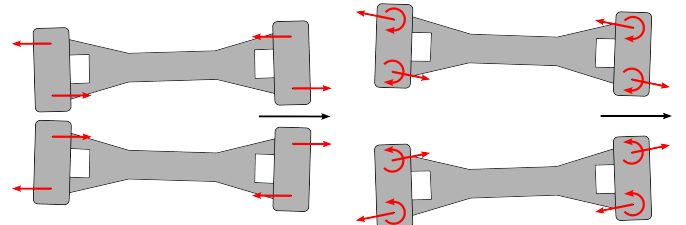
and therefore on the used preload. In the case of these mechanisms, the amount of time can be a few hours for high preload displacements z_d . In order to minimize the effect of creep the preload is applied to the mechanism just before the experiment is started.

C. Double translational joint

The last set of experiments is performed on the double translational joint. From Figure 18a, the mechanisms without preload can be concluded that the stiffness of the DTJ is half the stiffness of the TJ. This can be explained by the fact that for the DTJ the mechanism of the TJ is used twice in series. The resultant stiffness of two equal springs in series is half the stiffness of a single spring. This can also be used for these two mechanisms in series. The regions of zero-stiffness d_{zs} are 28.8 mm and 54.6 mm for the TJ and DTJ respectively. It was expected that d_{zs} for the DTJ would be double the value of the TJ. However, for the DTJ the region of zero-stiffness is 1.90 times higher than for the TJ. To understand the difference also the used preloads are of importance. The used preloads z_d are 53.6 mm for the TJ and 100.4 mm for the DTJ. This means that the preload for the DTJ is 1.87 times higher than for the TJ. Again, a factor of 2 was expected. A possible explanation is observed during the experiments. When a lateral displacement is applied to the mechanism, the forces on the two shuttles that are next to each other are not balanced out. A picture of the mechanism with an applied lateral displacement y_d is shown in Figure 19a. A FBD of the two shuttles, in the configuration without preload, is provided in Figure 19b. The forces, indicated by the red arrows, are applied on the shuttles by the I-beams. These forces form a couple, causing the shuttles to rotate. In this case, the left side of the shuttles rotates towards each other. For the preloaded configuration, the FBD is provided in Figure 19c. In this situation, the forces applied on the shuttles also have a vertical component, resulting in a rotated resultant force. Additionally, the I-beams apply a moment on the shuttles



(a) Picture of the double translational joint with a lateral displacement y_d .



(b) FBD of the two shuttles without preload. (c) FBD of the two shuttles with preload.

Fig. 19: Explanation of rotation of the shuttles. The displacement of the bottom shuttle is indicated with the black arrow. In red the applied loads are given.

counteracting the rotation introduced by the forces. For a certain preload, the applied moment is dominant resulting in an opposite rotation. In this case, the right side of the shuttles rotates towards each other. Both types of rotations result in a change in the effective applied preload displacement. This explains why the results of the DTJ are not exactly double the results of the TJ.

Performing the experiments on the DTJ in a horizontal orientation of the beams was not possible. Because the beams are in series and multiple shuttles are used the influence of gravity could not be neglected in this case. This was easily solved by testing the mechanism in a vertical orientation of the beams, as can be seen in Figure 13. Because the displacement is applied on the middle shuttle the limited height of the precision stage is no longer a problem.

The idea of adding multiple mechanisms in series can be expanded to n mechanisms instead of only two. It is expected that the region of zero-stiffness improves by a factor n . For the DTJ, the FEA had some problems finding the correct solution for the critical load. At the bifurcation point, the model has three DoF compared to one DoF for the TJ. All three shuttles are in unstable equilibrium and can either go to $+y$ or $-y$. For a model with n mechanisms in series, the number of DoF at the critical load is $2n - 1$.

D. Recommendations

From the results can be concluded that lateral torsional buckling can be used in compliant mechanisms to obtain zero-stiffness behaviour. Similar to zero-stiffness obtained with Euler buckling, the flexible beams have to be preloaded in the stiffest direction. However, with LTB a bending load is applied compared to a compressive load for Euler buckling. This opens up opportunities for applications where applying a compressive load may be challenging. Additionally, when the available space is limited, LTB can be a solution because the load is applied perpendicular to the flexible beam. In order to improve on this conceptual idea the following recommendations are proposed.

A recommendation for future research is further investigation of the optimal shape of the cross-section. It is expected that a rectangular beam is the optimal shape but the current model needs to be improved in order to prove this. Next, a new sensitivity analysis can be conducted to find the optimal dimensions for this rectangular beam.

In the research, the possibility to add multiple mechanisms in series to improve the region of zero-stiffness is investigated. This concept is proved by simulations and experiments on the translational joint. However, it would be interesting to expand this concept to the rotational joint. It is also recommended to investigate the positions of the beams in the current model. As discussed earlier the current configuration results in the rotation of the shuttles. It would be beneficial to have these forces aligned in order to prevent the undesired rotation.

The proposed method in this research can be applied to create a mechanism with variable stiffness. Without preload the stiffness is positive. The stiffness decreases for increasing preload until zero-stiffness behaviour is obtained. Beyond the critical preload, the mechanism has negative stiffness around the origin. The negative stiffness can be used in combination with an equal positive stiffness to obtain zero-stiffness behaviour.

Lastly, the focus of this work is on two types of joints, a translational and a rotational joint. For future work, also joints in 3D can be considered. The translational joint can be expanded to a spatial joint and the rotational joint to a spherical joint. Also, implementing the concept of LTB in compliant mechanisms with a translational and (coupled) rotational degree of freedom can be considered.

V. CONCLUSION

To conclude, in this work the possibility to use lateral torsional buckling in a compliant mechanism to obtain zero-stiffness behaviour is investigated. This concept is applied to a translational joint and a rotational joint with I-beams as flexible beams. A single beam is evaluated analytically to obtain the critical buckling load and

displacement. Both mechanisms are implemented in a FEA to investigate the behaviour. With the FEA the stroke of the mechanism considered to have zero-stiffness can be determined. Experiments on the mechanisms verify the results from the FEA. For the translational joint, a region of zero-stiffness $d_{zs} = 28.8$ mm is found. The rotational joint has a region of zero-stiffness $d_{zs} = 40.9$ mm or 26.4° . The FEA is also used to perform a sensitivity analysis on the cross-sectional dimensions. The goal of the sensitivity analysis is to maximize d_{zs} . It is found that an I-section is actually not the optimal shape of the beam. The maximum values of d_{zs} are found for beams with a rectangular cross-section. The region of zero-stiffness can also be improved by adding multiple mechanisms in series. This is performed for the translational joint in the FEA and verified by experiments. The double translational joint has a region of zero-stiffness $d_{zs} = 54.6$ mm. This is a multiplication of 1.90 compared to the translational joint. In general, the results of this work show that lateral torsional buckling can be used in compliant mechanisms to obtain zero-stiffness behaviour. Lateral torsional buckling is a possible alternative to Euler buckling in zero-stiffness compliant mechanisms, which makes it possible to use zero-stiffness in a wider range of applications.

REFERENCES

- [1] A. E. Albanesi, V. D. Fachinotti, and M. A. Pucheta, "A review on design methods for compliant mechanisms," *Mecánica Computacional*, vol. 29, no. 3, pp. 59–72, 2010.
- [2] S. Jagtap, B. Deshmukh, and S. Pardeshi, "Applications of compliant mechanism in today's world—a review," in *Journal of Physics: Conference Series*, vol. 1969, no. 1. IOP Publishing, 2021, p. 012013.
- [3] L. L. Howell, "Compliant mechanisms," in *21st century kinematics*. Springer, 2013, pp. 189–216.
- [4] M. Schenk and S. D. Guest, "On zero stiffness," *Proceedings of the Institution of Mechanical Engineers, Part C: Journal of Mechanical Engineering Science*, vol. 228, no. 10, pp. 1701–1714, 2014.
- [5] R. G. Saleeby, "A method for the characterization and selection of compliant joints," 2015.
- [6] F. Parvari Rad, R. Verthey, G. Berselli, and V. Parenti-Castelli, "Design and stiffness evaluation of a compliant joint with parallel architecture realizing an approximately spherical motion," in *Actuators*, vol. 7, no. 2. MDPI, 2018, p. 20.
- [7] T.-S. Yang, P.-J. Shih, and J.-J. Lee, "Design of a spatial compliant translational joint," *Mechanism and Machine Theory*, vol. 107, pp. 338–350, 2017.
- [8] G. Hao, H. Li, X. He, and X. Kong, "Conceptual design of compliant translational joints for high-precision applications," *Frontiers of Mechanical Engineering*, vol. 9, no. 4, p. 331, 2014. [Online]. Available: https://journal.hep.com.cn/fme/EN/abstract/article_11781.shtml
- [9] K. A. Tolman, E. G. Merriam, and L. L. Howell, "Compliant constant-force linear-motion mechanism," *Mechanism and Machine Theory*, vol. 106, pp. 68–79, 2016.
- [10] D. Farhadi, N. Tolou, and J. Herder, "A review on compliant joints and rigid-body constant velocity universal joints toward the design of compliant homokinetic couplings," *Journal of Mechanical Design*, vol. 137, p. 032301, 03 2015.
- [11] I. Gandhi and H. Zhou, "Synthesizing constant torque compliant mechanisms using precompressed beams," *Journal of Mechanical Design*, vol. 141, no. 1, 2019.
- [12] F. M. Morsch and J. L. Herder, "Design of a generic zero stiffness compliant joint," in *International Design Engineering Technical Conferences and Computers and Information in Engineering Conference*, vol. 44106, 2010, pp. 427–435.
- [13] H. Zhao, C. Zhao, S. Ren, and S. Bi, "Analysis and evaluation of a near-zero stiffness rotational flexural pivot," *Mechanism and Machine Theory*, vol. 135, pp. 115–129, 2019.
- [14] T. Liu, S. Bi, Y. Yao, Z. Dong, Q. Yang, and L. Liu, "Research on zero-stiffness flexure hinge (zsfh) based on spring four-bar linkage (4bsl)," *Mechanism and Machine Theory*, vol. 143, p. 103633, 2020.
- [15] C.-W. Hou and C.-C. Lan, "Functional joint mechanisms with constant-torque outputs," *Mechanism and Machine Theory*, vol. 62, pp. 166–181, 2013.
- [16] J. Van Eijk, "On the design of plate-spring mechanisms," 1985.
- [17] J. Dekens, "Three-step method to design the preload of geometries to create spatial large range of motion zero-stiffness compliant mechanisms," 2021.

- [18] P. G. Opdahl, B. D. Jensen, and L. L. Howell, "An investigation into compliant bistable mechanisms," in *International Design Engineering Technical Conferences and Computers and Information in Engineering Conference*, vol. 80319. American Society of Mechanical Engineers, 1998, p. V01BT01A046.
- [19] G. Chen, Y. Gou, and L. Yang, "Research on multistable compliant mechanisms: The state of the art," *Proceedings of the 9th International Conference on Frontiers of Design and Manufacturing (ICFDM 2010)*, pp. 17–19, 01 2010.
- [20] M. BRETTLE, "Lateral torsional buckling and slenderness," *New steel construction*, vol. 14, no. 9, 2006.
- [21] I. Kalkan and S. Kartal, "Torsional rigidities of reinforced concrete beams subjected to elastic lateral torsional buckling," *International Journal of Civil and Environmental Engineering*, vol. 11, no. 7, pp. 969–972, 2017.
- [22] S. Timoshenko, J. Gere, and W. Prager, "Theory of elastic stability," *Journal of Applied Mechanics*, vol. 29, no. 1, p. 220, 1962.
- [23] A. Andrade, D. Camotim, and P. P. e Costa, "On the evaluation of elastic critical moments in doubly and singly symmetric i-section cantilevers," *Journal of Constructional Steel Research*, vol. 63, no. 7, pp. 894–908, 2007.
- [24] J. Wu, S. Cai, J. Cui, and J. Tan, "A generalized analytical compliance model for cartwheel flexure hinges," *Review of Scientific Instruments*, vol. 86, p. 105003, 10 2015.
- [25] R. M. Panas, F. Sun, L. Bekker, and J. B. Hopkins, "Combining cross-pivot flexures to generate improved kinematically equivalent flexure systems," *Precision Engineering*, vol. 72, pp. 237–249, 2021.
- [26] R. C. Hibbeler, *Mechanics of materials*. Pearson Educación, 2005.
- [27] K. Dwivedi, "Flexural rigidity: Definition, formula, derivation, calculation," Jul 2022. [Online]. Available: <https://www.mechical.com/2022/05/flexural-rigidity.html>
- [28] C. I. of Steel Construction, "Torsional section properties of steel shapes," vol. 19, 2002.
- [29] I. G. Raftoyiannis and T. Adamakos, "Critical lateral-torsional buckling moments of steel web-tapered i-beams," *The Open Construction and Building Technology Journal*, vol. 4, no. 1, 2010.
- [30] D. Bresser, G. Ravenshorst, and P. Hoogenboom, "General formulation of equivalent moment factor for elastic lateral torsional buckling of slender rectangular sections and i-sections," *Engineering Structures*, vol. 207, p. 110230, 2020.
- [31] H. Ozbasaran, "A parametric study on lateral torsional buckling of european ipn and ipe cantilevers," *International Journal of Civil, Architectural, Structural and Construction Engineering, World Academy of Science, Engineering and Technology*, vol. 8, no. 7, 2014.
- [32] R. Piotrowski and A. Szychowski, "Lateral-torsional buckling of beams elastically restrained against warping at supports," *Archives of Civil Engineering*, vol. 61, no. 4, pp. 155–174, 2015.
- [33] J.-M. Battini and C. Pacoste, "Co-rotational beam elements with warping effects in instability problems," *Computer Methods in Applied Mechanics and Engineering*, vol. 191, no. 17-18, pp. 1755–1789, 2002.
- [34] J. C. Lagarias, J. A. Reeds, M. H. Wright, and P. E. Wright, "Convergence properties of the nelder–mead simplex method in low dimensions," *SIAM Journal on optimization*, vol. 9, no. 1, pp. 112–147, 1998.
- [35] "The online materials information resource." [Online]. Available: <https://www.matweb.com/search/DataSheet.aspx?MatGUID=1c41e50c2e324e00b0c4e419ca780304&ckck=1>
- [36] "I-beam 414," Jul 2017. [Online]. Available: <https://www.maquett.nl/product/strip-414/>
- [37] PI. M-505 low profile translation stages with ballscrew drives. PI. [Online]. Available: https://static.pi-usa.us/fileadmin/user_upload/pi_us/files/product_datasheets/M505_Precision_Positioning_Stage.pdf
- [38] FUTEK. Miniature s-beam jr. load cell lsb200. FUTEK. [Online]. Available: <https://www.futek.com/store/legacy-sensors-and-instruments/miniature-s-beam-LSB200/FSH03875>
- [39] Z. Hongzhe and B. Shusheng, "Accuracy characteristics of the generalized cross-spring pivot," *Mechanism and Machine Theory*, vol. 45, no. 10, pp. 1434–1448, 2010.
- [40] Instron, "Elastic hysteresis." [Online]. Available: <https://www.instron.com/en-us/resources/glossary/e/elastic-hysteresis>

4

Discussion

4.1. Discussion literature review

This thesis focused on obtaining zero-stiffness compliant joints using lateral torsional buckling. First, the literature review was carried out. Because the current design of zero-stiffness compliant mechanisms is in most cases based on Euler buckling, the focus of the literature review was on comparing Euler buckling and lateral torsional buckling. Calculation methods for both types of buckling were gathered in order to find similarities between the buckling behaviour. Both types of buckling have a similar working principle, a load is applied in a stiff direction of the beam resulting in a deflection in a direction with lower stiffness at the critical load. There is also a major difference, for Euler buckling a compressive (axial) load is applied on a beam. At the critical load, the beam has a deflection in the direction of the lowest bending stiffness. For lateral torsional buckling, however, a (transverse) load is applied in the direction with the highest bending stiffness. This results in a deflection in the direction of the lowest bending stiffness (lateral) in combination with a rotation of the beam at the critical load.

In the literature review is found that determining the critical load is the focus of research on lateral torsional buckling. It is an undesired phenomenon and is considered to be a failure mode of the designed beams. An obvious explanation is that lateral torsional buckling is almost always investigated in civil and structural engineering. The focus of these engineering fields is on statics and not on the flexible behaviour of beams. However, with the correct combination of geometry and material properties, a beam will only deform elastically.

4.2. Discussion research paper

Next, the results from the research paper will be discussed. The simulations and experiments showed that zero-stiffness behaviour can be obtained using lateral torsional buckling. A good agreement was found between the results of simulations and experiments on the translational and rotational joints. In order to make a correct comparison between simulations and experiments it was required to use the rigidities in the FEA. The rigidities are EA , EI_{yy} , EI_{zz} and GJ , and are derived from the material properties E and G and the cross-sectional properties A , I_{yy} , I_{zz} and J . Using the rigidities results in more accurate results because the material and geometric imperfections are averaged out. The rigidities are determined in a set of material tests. A more elaborate explanation of these tests and the obtained rigidities is provided in Appendix A. In the experiments, a certain amount of hysteresis was measured. Part of the hysteresis is introduced by the pulley in the experiments. The other source of hysteresis is elastic hysteresis, which increases for an increasing preload displacement.

A third prototype was made of the double translational joint (DTJ). This model consists of two translational joints (TJ) in series. The idea behind this concept is that the region of zero-stiffness is doubled for two joints in series. The found regions of zero-stiffness are 28.8 mm and 54.6 mm for the TJ and the DTJ respectively. This is a multiplication of 1.90, where 2 was expected. However, a possible explanation for this difference was observed. The forces and moments applied by the beams on the shuttles result in a rotation of the shuttles. The rotation results in a change of the effective applied preload displacement. An explanation of this observation is included in Appendix C. Nevertheless, the results from the DTJ show that using multiple mechanisms in series improves the region of zero-stiffness.

A sensitivity analysis of the cross-sectional dimensions is also part of the research paper. The effect of variations of these dimensions on the region of zero-stiffness d_{zs} is determined. For this analysis, three grid searches are performed, each with a different combination of dimensions. In the sensitivity analysis is found that the highest values of d_{zs} are found for low values of the web height H and flange width W and high values of the flange thickness h and web width w . This combination of dimensions, however, does not correspond with an I-section anymore. It is found that a rectangular cross-section is the optimal shape. However, this causes a problem in the FEA, the used expression for the St. Venant torsional constant J is only valid for thin-walled I-sections. How this can be improved in order to perform a better sensitivity analysis of the optimal shape is discussed in Appendix B.

4.3. General discussion and recommendations

A general point of discussion is the used terminology in this work. The term zero-stiffness is used to describe the behaviour of the compliant mechanisms. Possible alternative terms are quasi-zero-stiffness [26] or neutral stability [27]. In this work, the extent of zero-stiffness behaviour depends on the used bound on the reaction force RF_b . A higher RF_b results in a higher region of zero-stiffness, which is the aim of this research. For other purposes, however, it might be beneficial to use a very low RF_b resulting in a mechanism that actually approaches zero-stiffness. For example, for vibration isolation, actual zero-stiffness behaviour is required [26, 28, 29].

The focus of this work was not directly on obtaining zero-stiffness behaviour. It started with a more general idea: using lateral torsional buckling in compliant mechanisms. One of the conceptual ideas was changing the shape of an I-beam such that, lateral torsional buckling occurs at a desired location at a desired load. The idea of a twisted beam with an applied load such that lateral torsional buckling occurs after the twist is removed by rotation looked promising. A basic model with possible alternations of this idea is provided in Appendix E.

From the research paper can be concluded that lateral torsional buckling can be implemented in a compliant mechanism to obtain zero-stiffness behaviour. For this behaviour, a preload is required in the stiffest bending direction of the flexible beams. This main difference, compared to current zero-stiffness compliant mechanisms, opens up opportunities to apply zero-stiffness in a wider range of compliant mechanisms. For example, it might be challenging to apply a compressive load to a flexible beam, or a mechanism can be made smaller if lateral torsional buckling is used as a working principle. Additionally, an application where a gravitational force of a mass causes lateral torsional buckling belongs to the possibilities. However, a comparison with current zero-stiffness compliant mechanisms is not included in this work. Therefore, it is complicated to draw a conclusion about the region of zero-stiffness. It is recommended to compare the region of zero-stiffness of both working principles by, for example, using beams of similar dimensions. The following recommendations are proposed for further improvement of this idea.

It is recommended to further investigate the optimal shape of the cross-section. It is expected that the optimal shape is a rectangular cross-section. However, as mentioned before, in this analysis the expression for the St. Venant torsional constant is not always correct. After the improvement of the expression, a new sensitivity analysis can be carried out to find the optimal shape and dimensions of the cross-section.

The investigation of adding multiple mechanisms in series focused on the translational joint. Promising results were obtained for this idea. Therefore, it would be interesting to apply this concept to the rotational joint as well. This idea can also be expanded to more than two mechanisms in series. Next to the increase in zero-stiffness this can also be used to obtain a multistable mechanism.

The stiffness of the mechanisms in the research paper can be varied. One of the possibilities is to create a (bistable) mechanism with negative stiffness around the origin. Such a mechanism can be combined with an equal positive stiffness (for example a spring) to obtain zero-stiffness behaviour.

Lastly, the focus of this work was on a translational and rotational joint, both mechanisms move in the 2D-plane. For future research, also joints in 3D can be considered. In the process of finding a working principle, an alternative to the rotational joint was considered consisting of two beams connected to each other by a rigid part. This concept has some unsolved problems but may be interesting for future research. A more elaborate description is given in Appendix D.

5

Conclusion

The objective of this thesis was to investigate the use of lateral torsional buckling in compliant joints to obtain zero-stiffness behaviour. In the literature review was found that Euler buckling and lateral torsional buckling have similarities in their working principles. A load is applied in a direction with high stiffness of the flexible beam for both buckling types. At the critical buckling load, the flexible beams will deflect to one of the directions with lower stiffness.

The research paper showed that zero-stiffness compliant mechanisms can be obtained using lateral torsional buckling. This concept is applied to two compliant joints, a translational and a rotational joint, with I-beams as flexible beams. First, the buckling behaviour of a single beam is determined in an analytical analysis. Next, the two joints are implemented into a model in a finite element analysis. Using the models, the optimal preload displacement at which the zero-stiffness behaviour occurs is determined. Experiments on prototypes of the compliant joints verify the results from the simulations. The translational joint has a region of zero-stiffness of 28.8 mm. For the rotational joint, a region of zero-stiffness of 40.9 mm is found, this corresponds with a rotation of 26.4°. A sensitivity analysis is performed on the cross-sectional dimensions to find the optimal region of zero-stiffness. It is found that not an I-section, but a rectangular shape is the optimal shape of the cross-section. An additional option to improve the region of zero-stiffness is adding multiple mechanisms in series. This is performed for the translational joint, a model is made in the FEA and the results are verified by experiments. The so-called double translational joint has a region of zero-stiffness of 54.6 mm, a multiplication of 1.90 with respect to the single translational joint.

In general, it can be concluded that lateral torsional buckling can be implemented in compliant mechanisms to obtain zero-stiffness behaviour. A proof of concept is given in this work, together with recommendations for further research. In future work, the performance of the zero-stiffness compliant mechanisms of this work can be compared to the current design of zero-stiffness compliant mechanisms. Additionally, some improvements and extensions for this work are discussed. This work is a first step towards zero-stiffness compliant joints with lateral torsional buckling as a working principle. An actual application is yet to be discovered, but the results of this work are promising.

Appendices

The appendices contain supplementary material that is used in the thesis. Appendix A contains the determination of the rigidities that are used in the experiments. An explanation is given of the performed material tests and how the results are used in the FEA. In Appendix B, the determination of a general expression of the St. Venant torsional constant is described. Appendix C contains the testing protocol that is used to carry out the experiments. Additionally, an explanation of the parasitic x -displacement during the experiments is given. Also, some photos of the experiments are provided and the rotation of the shuttles in the double translational joint is discussed in more detail. An alternative design of the rotational joint is provided in Appendix D. The design of a twisted beam, for which lateral torsional buckling occurs after the beam is twisted back, is described in Appendix E. The used MATLAB[®] codes in this work are provided in Appendix F. The appendix starts with a description of the analysis of one of the mechanisms. An elaboration of the sensitivity analysis is provided next. Appendix G contains a description of the processing of the measurement data.

A

Rigidities

For comparison of the simulations and experiments, the rigidities of the beams are used. There are four rigidities; the axial rigidity EA , two flexural rigidities EI_{yy} and EI_{zz} and the torsional rigidity GJ . The rigidities are obtained by multiplying one of the material properties, Young's Modulus E and Shear Modulus G , with one of the cross-sectional properties, the area A , the second moments of inertia I_{yy} and I_{zz} and the St. Venant torsional constant J . Originally, the material properties and cross-sectional properties were used separately in the finite element analysis (FEA). However, the results of the FEA did not match the results from the experiments. Imperfections in dimensions and the material are included in the determination of the rigidities. This results in better agreement between the FEA and the experiments. The relevant dimensions of the beams are provided in Figure A.1 for clarification.

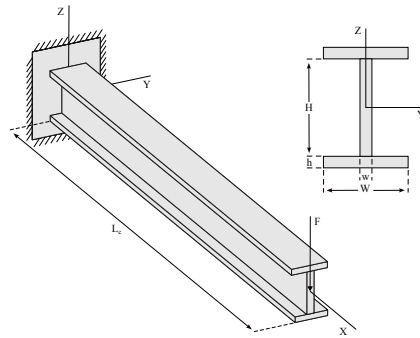


Figure A.1: Cantilever beam with applied end-point load and cross-section of the I-beam with relevant dimensions.

A.1. Axial rigidity

To determine the axial rigidity EA , a tensile test is performed. In all the material tests, the same beams are used as in the experiments on the prototypes. For the tensile test, three specimens of $L = 100$ mm are tested up to the point of failure. The results from these tensile tests are provided in Figure A.2. In this work, the beams will only be used in the elastic domain. It is decided to calculate EA for the linear part up to an elongation of 1 mm. The strain is calculated by

$$\epsilon = \frac{\Delta L}{L} = \frac{1 \text{ mm}}{100 \text{ mm}} = 0.01 . \quad (\text{A.1})$$

The strain is used to calculate the Young's modulus in

$$E = \frac{\sigma}{\epsilon} . \quad (\text{A.2})$$

This expression requires the stress, which is calculated by

$$\sigma = \frac{F}{A} . \quad (\text{A.3})$$

If we use σ in Equation A.2 and multiply both sides by A , this results in

$$EA = \frac{F}{\epsilon}. \quad (\text{A.4})$$

With $\epsilon = 0.01$ and $F = 242.34$ N, the axial rigidity becomes $EA = 2.42 \times 10^4$ N.

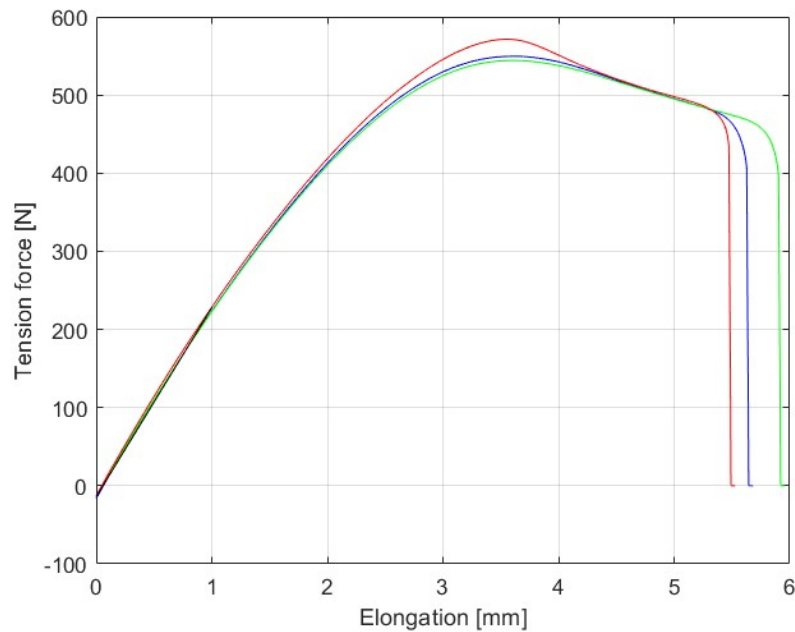


Figure A.2: Results from the tensile test for determination of axial rigidity EA .

A.2. Flexural rigidities

To determine the flexural rigidities, two three-point bending tests are performed. In Figure A.3 a picture is provided from a three-point bending test. Two points of the beam are simply supported, in the middle a vertical displacement is applied and the reaction force is measured.



Figure A.3: Picture of the three-point bending test.

First, the flexural rigidity EI_{yy} will be determined. This is the orientation corresponding to Figure A.3 and is the stiffest bending direction. The distance between the two simply supported points L_b is 60 mm. The results from the three-point bending tests are provided in Figure A.4. Unfortunately, one of the files with

measurement data was corrupted, so only two tests are used in this determination. A straight line is fitted through the results to obtain EI_{yy} . The flexural rigidity is calculated using

$$EI_{yy} = \frac{FL_b^3}{48w}, \quad (\text{A.5})$$

in which w is the deflection [30]. With $F = 15.31 \text{ N}$ and $w = 0.5 \times 10^{-3} \text{ m}$ the flexural rigidity becomes $EI_{yy} = 0.138 \text{ N/m}^2$.

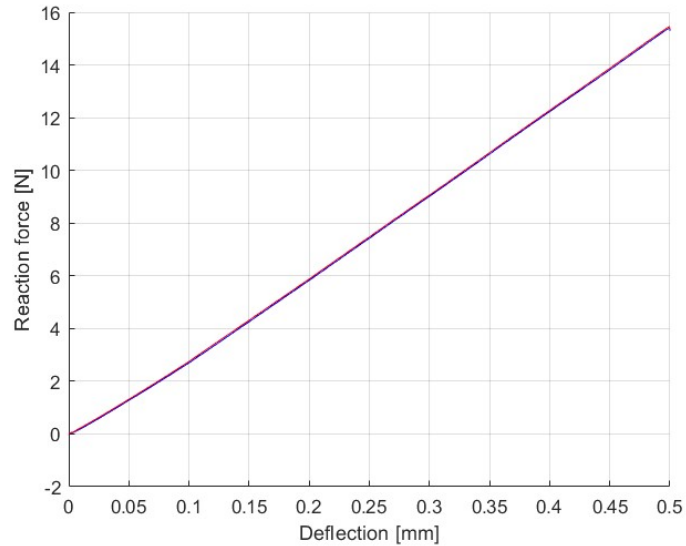


Figure A.4: Results from the three-point bending test for determination of flexural rigidity EI_{yy} .

The same procedure is performed for the flexural rigidity EI_{zz} . The results are shown in Figure A.5. The

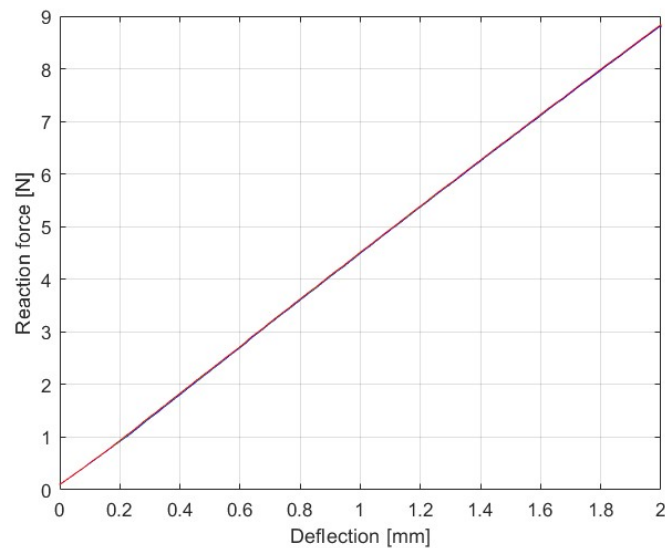


Figure A.5: Results from the three-point bending test for determination of flexural rigidity EI_{zz} .

flexural rigidity is calculated using

$$EI_{zz} = \frac{FL_b^3}{48w}, \quad (\text{A.6})$$

with $F = 8.686 \text{ N}$ and $w = 2 \times 10^{-3} \text{ m}$ the flexural rigidity becomes $EI_{zz} = 0.0195 \text{ N/m}^2$.

A.3. Torsional rigidity

Lastly, the torsional rigidity GJ is determined by a torsion test. A beam of length $L = 100$ mm is used for this test. A rotation $\theta = 90^\circ$ is applied on the specimen. The results of the torsion tests are shown in Figure A.6. The angle of twist of determined by

$$\theta = \frac{TL}{GJ}, \quad (\text{A.7})$$

in which T is the applied torque [30]. This expression can be rewritten into

$$GJ = \frac{TL}{\theta}. \quad (\text{A.8})$$

With $T = 0.0671$ Nm, $L = 0.1$ m and $\theta = 90^\circ$, the torsional rigidity becomes $GJ = 0.0043$ Nm². The found

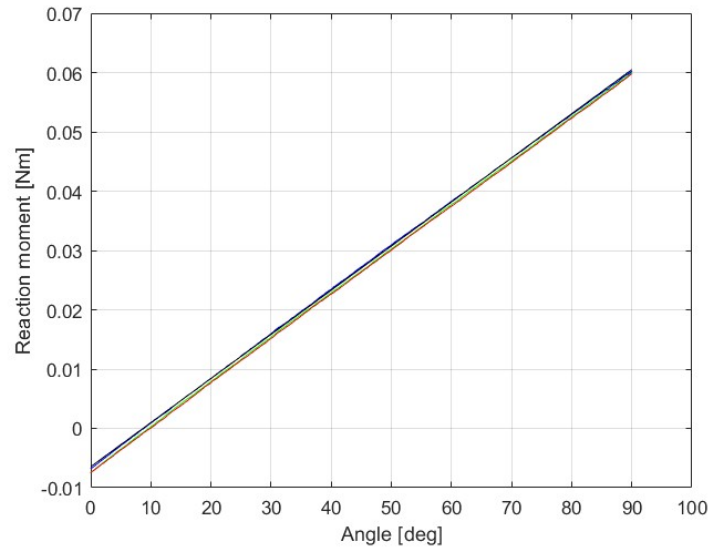


Figure A.6: Results from the torsion test for determination of torsional rigidity GJ .

rigidities are used in the FEA instead of the separate material and cross-sectional properties and are provided in Table A.1. To give an idea of how much the results will differ without the use of rigidities the cross-sectional properties are calculated using the expressions in Equation A.9 and using the obtained values for the rigidities. For this calculation, a very important assumption is made: the material properties provided by the manufacturer are correct. The used material properties are $E = 2.1$ GPa and $G = 0.8$ GPa. This assumption implies that the material properties are perfect and all the imperfections are cross-sectional imperfections. The errors in the cross-sectional properties are varying from 11% up to 31%. The actual material properties will be a bit lower and the actual values of the cross-sectional properties lie somewhere in between the values in the table. However, we can not determine what the correct values are. This is the reason the rigidities are used in the FEA.

Table A.1: Determined rigidities

	Rigidities		Material test	Formula
EA	2.42×10^4 N	A	1.15×10^{-05} m ²	1.34×10^{-05} m ²
EI_{yy}	0.138 N/m ²	I_{yy}	6.56×10^{-11} m ⁴	8.45×10^{-11} m ⁴
EI_{zz}	0.0195 N/m ²	I_{zz}	9.31×10^{-12} m ⁴	1.05×10^{-11} m ⁴
GJ	0.0043 Nm ²	J	5.33×10^{-12} m ⁴	7.81×10^{-12} m ⁴

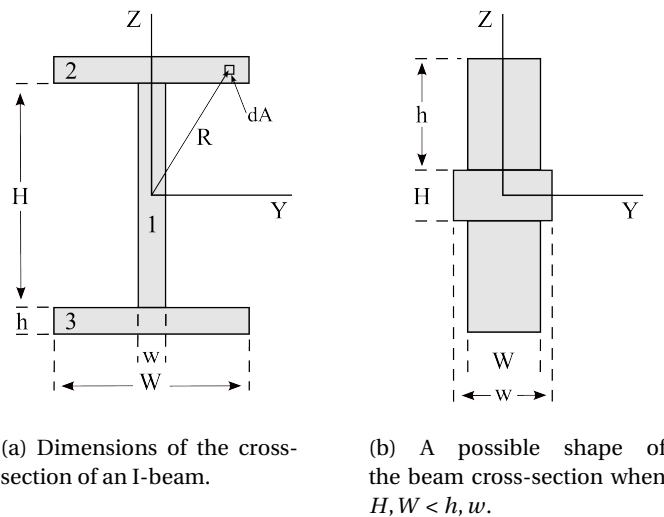
$$\begin{aligned}A &= 2Wh + Hw \\I_{yy} &= \frac{1}{12}wH^3 + \frac{2}{12}Wh^3 + \frac{2}{4}hW(H+h)^2 \\I_{zz} &= \frac{1}{12}Hw^3 + \frac{2}{12}hW^3 \\J &= \frac{2}{3}Wh^3 + \frac{1}{3}Hw^3\end{aligned}\tag{A.9}$$

B

Torsional constant

B.1. Optimal shape

In the sensitivity analysis in the research paper, the influence of the cross-sectional dimensions on the region of zero-stiffness is investigated. The dimensions of the cross-section are provided in Figure B.1a. From the sensitivity analysis is concluded that the highest region of zero-stiffness is found for low values of H and W and high values of h and w . A cross-section corresponding with these values of shown in Figure B.1. The definition of the dimensions is still the same. The shape of the cross-section, however, is completely different.



(a) Dimensions of the cross-section of an I-beam.

(b) A possible shape of the beam cross-section when $H, W < h, w$.

Figure B.1: Dimensions of the cross-sections that will be used in the determination of the torsional constant J .

The changing shape of the cross-section causes some problems in the FEA. In the FEA, the following cross-sectional properties are calculated; the area A , the second moments of inertia I_{yy} and I_{zz} and the St. Venant torsional constant J . The expressions of A , I_{yy} and I_{zz} remain the same for the changing shape and are

$$\begin{aligned}
 A &= 2Wh + Hw . \\
 I_{yy} &= \frac{1}{12} wH^3 + \frac{2}{12} Wh^3 + \frac{2}{4} hW(H + h)^2 , \\
 I_{zz} &= \frac{1}{12} Hw^3 + \frac{2}{12} hW^3 .
 \end{aligned}
 \tag{B.1}$$

B.2. Definition torsional constant

The expression of the St. Venant torsional constant, however, does not remain the same. In the research paper, the used torsional constant is

$$J = \frac{2}{3}Wh^3 + \frac{1}{3}Hw^3, \quad (\text{B.2})$$

which is only valid for a thin-walled I-section [20]. The St. Venant torsional constant is also referred to as the polar moment of inertia [31]. The definition of this constant is

$$J = \int R^2 dA, \quad (\text{B.3})$$

in which each element of area dA is multiplied by the square of the distance to the origin. R and dA are also provided in Figure B.1a. By defining $R^2 = y^2 + z^2$ and $dA = dydz$, this integral becomes

$$J = \iint (y^2 + z^2) dydz = \iint y^2 dydz + \iint z^2 dydz. \quad (\text{B.4})$$

The cross-section is divided into 3 parts, which are shown in Figure B.1a. The torsional constant is now calculated using

$$J = J_1 + J_2 + J_3. \quad (\text{B.5})$$

First, the torsional constant of the web J_1 is determined. If the bounds of the integral are added to Equation B.4 the integral becomes

$$J_1 = \int_{-\frac{H}{2}}^{\frac{H}{2}} \int_{-\frac{w}{2}}^{\frac{w}{2}} y^2 dydz + \int_{-\frac{H}{2}}^{\frac{H}{2}} \int_{-\frac{w}{2}}^{\frac{w}{2}} z^2 dydz. \quad (\text{B.6})$$

The integration with respect to z is performed resulting in

$$J_1 = z \Big|_{-\frac{H}{2}}^{\frac{H}{2}} \int_{-\frac{w}{2}}^{\frac{w}{2}} y^2 dy + \frac{1}{3} z^3 \Big|_{-\frac{H}{2}}^{\frac{H}{2}} \int_{-\frac{w}{2}}^{\frac{w}{2}} dy. \quad (\text{B.7})$$

If we fill in the integral bounds on z , this results in

$$J_1 = H \int_{-\frac{w}{2}}^{\frac{w}{2}} y^2 dy + \frac{1}{12} H^3 \int_{-\frac{w}{2}}^{\frac{w}{2}} dy. \quad (\text{B.8})$$

Now, the integration with respect to y is performed, this gives

$$J_1 = H \frac{1}{3} y^3 \Big|_{-\frac{w}{2}}^{\frac{w}{2}} + \frac{1}{12} H^3 y \Big|_{-\frac{w}{2}}^{\frac{w}{2}}. \quad (\text{B.9})$$

The integral bounds on y are filled in, resulting in the final expression

$$J_1 = \frac{1}{12} Hw^3 + \frac{1}{12} wH^3. \quad (\text{B.10})$$

The expressions for J_2 and J_3 are the same. The determination is similar to J_1 , the bounds on the integral are added to Equation B.4. The integral becomes

$$J_2 = \int_{\frac{H}{2}}^{\frac{H}{2}+h} \int_{-\frac{W}{2}}^{\frac{W}{2}} y^2 dydz + \int_{\frac{H}{2}}^{\frac{H}{2}+h} \int_{-\frac{W}{2}}^{\frac{W}{2}} z^2 dydz. \quad (\text{B.11})$$

The integration with respect to z becomes

$$J_2 = z \Big|_{\frac{H}{2}}^{\frac{H}{2}+h} \int_{-\frac{W}{2}}^{\frac{W}{2}} y^2 dy + \frac{1}{3} z^3 \Big|_{\frac{H}{2}}^{\frac{H}{2}+h} \int_{-\frac{W}{2}}^{\frac{W}{2}} dy. \quad (\text{B.12})$$

This is followed by filling in the integral bounds of z , which results in

$$J_2 = H \int_{-\frac{W}{2}}^{\frac{W}{2}} y^2 dy + \left(\frac{H^2 h}{4} + \frac{Hh^2}{2} + \frac{h^3}{3} \right) \int_{-\frac{W}{2}}^{\frac{W}{2}} dy. \quad (\text{B.13})$$

Next, the integration with respect to y is performed, resulting in

$$J_2 = H \frac{1}{3} y^3 \Big|_{-\frac{W}{2}}^{\frac{W}{2}} + \left(\frac{H^2 h}{4} + \frac{Hh^2}{2} + \frac{h^3}{3} \right) y \Big|_{-\frac{W}{2}}^{\frac{W}{2}}. \quad (\text{B.14})$$

When we fill in the bounds we find the final expression

$$J_2 = \frac{1}{12} hW^3 + W \left(\frac{H^2 h}{4} + \frac{Hh^2}{2} + \frac{h^3}{3} \right), \quad (\text{B.15})$$

for J_2 and J_3 . When these results are used in Equation B.5, the expression for the torsional constant becomes

$$J = \frac{1}{12} Hw^3 + \frac{1}{12} wH^3 + \frac{1}{6} hW^3 + \frac{1}{2} WH^2 h + WHh^2 + \frac{2}{3} Wh^3. \quad (\text{B.16})$$

This expression can be rewritten into

$$J = \frac{1}{12} wH^3 + \frac{2}{12} Wh^3 + \frac{2}{4} hW(H+h)^2 + \frac{1}{12} Hw^3 + \frac{2}{12} hW^3. \quad (\text{B.17})$$

When comparing this expression with the second moments of inertia in Equation B.1, it can be concluded that

$$J = I_{yy} + I_{zz}. \quad (\text{B.18})$$

The same result is also found in literature [20, 31, 30]. This general expression can be applied to both cross-sections in Figure B.1. We end up with a situation where Equation B.2 is valid for thin-walled I-sections and where Equation B.18 is valid for rectangular cross-sections. For further research, it is recommended to find an expression for J that is always valid or, to develop a few lines of code that can determine J based on the shape of the cross-section using multiple expressions for J .

C

Experiments

C.1. Testing protocol

This appendix elaborates on the testing protocol used to carry out the experiments. An overview of the test set-up is provided in Figure C.1. The relevant parts are indicated with white text. The force sensor, connected to the precision stage, is connected to the mechanism by a fishing line. For clarification, the used fishing line is made red in the figure. The mechanism is connected to a mass by another fishing line and a green cartesian coordinate system is provided for the directions. The pulley is used to redirect the vertical gravitational force of the mass to a horizontal force.

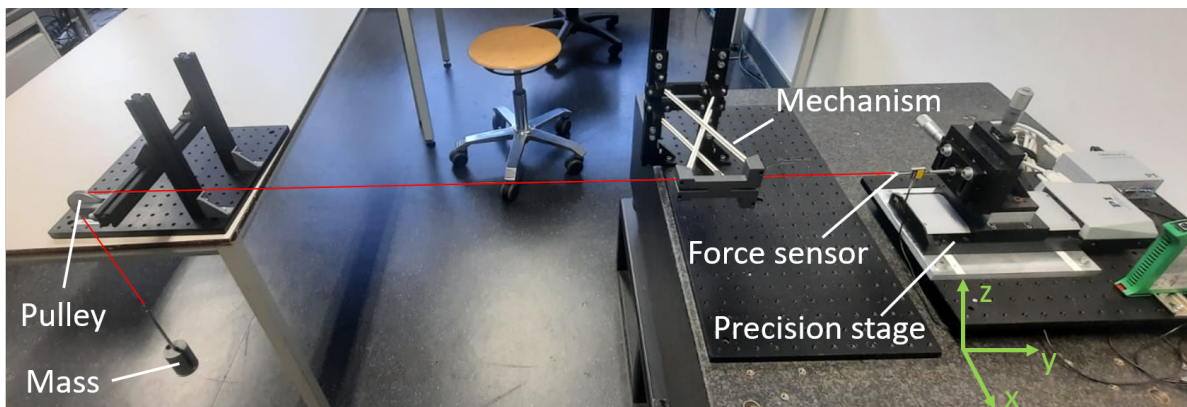


Figure C.1: Experimental set-up; the precision stage with force sensor, the compliant mechanism and the mass connected to each other by a fishing line.

The following steps are taken for a set of measurements for one of the mechanisms (translational joint or rotational joint):

1. The mechanism, without preload, is mounted on two XE25L300/M Thorlabs construction rails. Next, the construction rails are mounted on the Thorlabs breadboard. The mechanism is connected to the precision stage and mass by the fishing lines. The position of the precision stage is in the middle (50 mm).
2. The height of the pulley and precision stage is adjusted such that the fishing lines are horizontal. Next, the pulley and precision stage are positioned such that the x -position is correct. A more elaborate explanation of the x -positioning will be given after this measurement protocol.
3. The mechanism is now ready for the first set of measurements. The precision stage moves to 0 mm, this corresponds to -50 mm after data-processing. Next, the precision stage performs a forwards motion from 0 mm to 100 mm followed by the reverse motion from 100 mm to 0 mm. The displacements and

measured forces are saved to an Excel-file. This is a single measurement, this process is repeated 5 times to reduce measurement-errors.

4. The mechanism can now be prepared for the next set of measurements. A preload displacement z_d is applied using gauge blocks. One of the rigid parts, mounted on the construction rails, is displaced $\frac{z_d}{2}$ downwards and the other rigid part is displaced $\frac{z_d}{2}$ upwards. Using this method, the fishing lines remain always horizontal and no further adjusting is required for the force sensor and pulley. The measurement process in step 3 can now be performed.
5. Step 4 is repeated for all the required preloads.

After all the steps are taken for the measurements on a mechanism, this process can be repeated for the other mechanism. The Excel-files are loaded into MATLAB[®], the data is processed and the results are compared to the results from the FEA.

C.2. Parasitic x -displacement

As mentioned above, the x -position of the pulley and precision stage requires more attention. Over the range of motion, the mechanism has a parasitic x -displacement x_p . The parasitic displacement is the largest for the rotation joint and can result in measurement errors because the fishing line is no longer in line with the force sensor. To minimize parasitic forces the distance between the mechanism and force sensor have to be maximized. The same holds for the distance between the mechanism and the pulley. As can be seen in Figure C.1, the available space between the mechanism and force sensor was limited. Therefore, the effect of the relatively small distance on the measurements will be determined. The minimum length of the fishing line between the mechanism and force sensor is $L_f = 190$ mm. A top-view of the situation is provided in Figure C.2. The green line corresponds with the path of the middle point of the shuttle over the range of motion. The blue line is the rotational mechanism at the end position. The red line is the fishing line from the mechanism to the force sensor. The black lines are used to make a triangle to determine the angle of the fishing line.

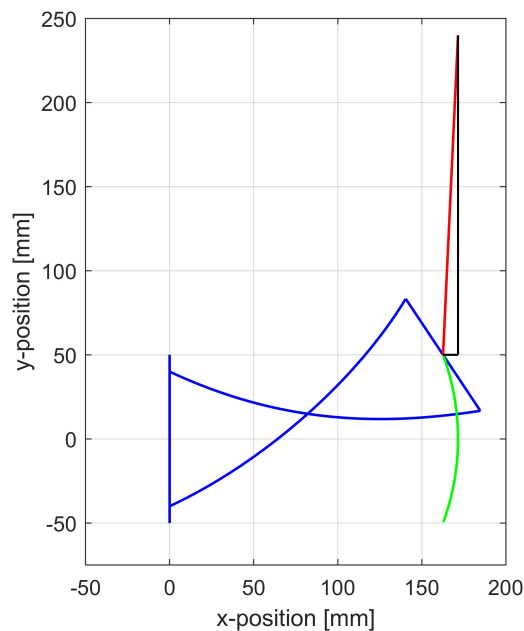


Figure C.2: Determination of the parasitic displacement x_p .

This triangle is rotated, as can be seen in Figure C.3. The dimensions to calculate α are also provided. The formula to calculate the angle is

$$\alpha = \arcsin \frac{x_p}{L_f}. \quad (\text{C.1})$$

For the rotation mechanism, $x_p = 8.9$ mm. Combined with $L_f = 190$ mm, this results in $\alpha = 2.69^\circ$. Next, α can be used to determine the measurement error introduced by x_p . The measured reaction force in the end position for the rotational joint without preload is $F_m = 3.1822$ N. The tension force in the fishing line is calculated by

$$F_t = \frac{F_m}{\cos \alpha}. \quad (\text{C.2})$$

This results in $F_t = 3.1857$ N. So the difference between the measured force and the actual force in the fishing line is 0.0035 N. The error is calculated using

$$\text{error} = \frac{F_t - F_m}{F_m} 100. \quad (\text{C.3})$$

The resulting error is 0.11%. It can be concluded that the limited space between the force sensor and mechanism has a minimal effect on the measurement results. The situation described above is the worst case scenario. In the experiments the parasitic displacement x_p was already taken into account. In step 2 of the measurement protocol is mentioned that the precision stage is positioned such that the x -position is correct. The aim is to position the precision stage halfway the parasitic displacement such that x_p is the same for the neutral position $y_d = 0$ mm and the outer positions $y_d = \pm 50$ mm. If the force sensor has the perfect x -position, the measurement error is 0.0009 N or 0.02%.

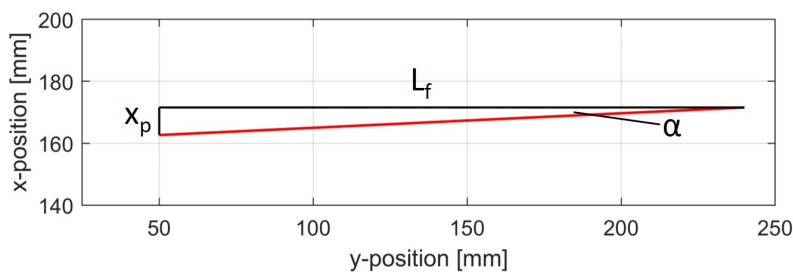
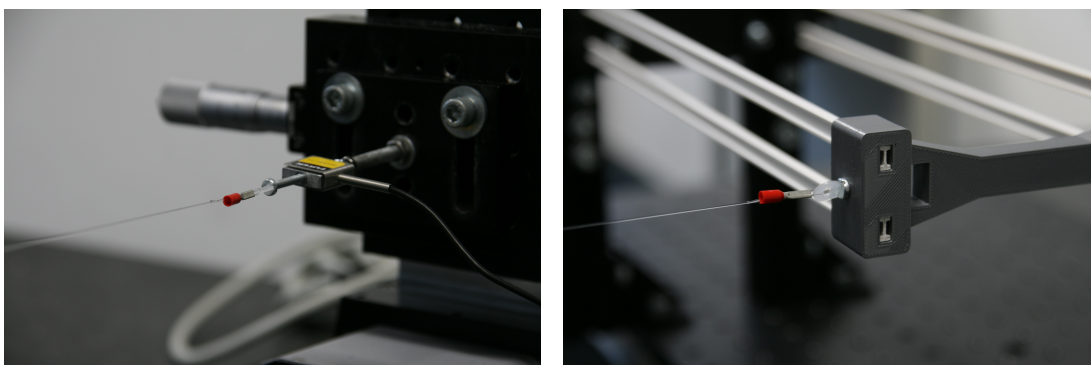


Figure C.3: Rotated triangle to determine α .

C.3. Additional photos

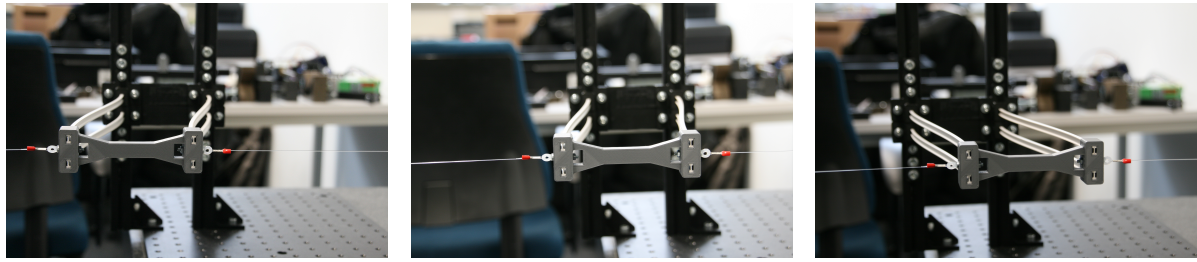
Next, some photos from the experiments are provided. In Figure C.4 two close-ups from the connections of the fishing wire to the force sensor and shuttle are shown. In Figure C.5 the positions over the range of motion of the translational joint are shown. Similar, but from above, in Figure C.6 the positions over the range of motion of the rotational joint are shown. Figure C.7 is a close-up of the translational mechanism at the critical preload displacement. The photo gives a clear view on how the beams deform.



(a) Close-up of the connection to the force sensor.

(b) Close-up of the connection to the 3D-printed shuttle.

Figure C.4: Close-up of the connections of the fishing wire to the components of the experimental set-up.

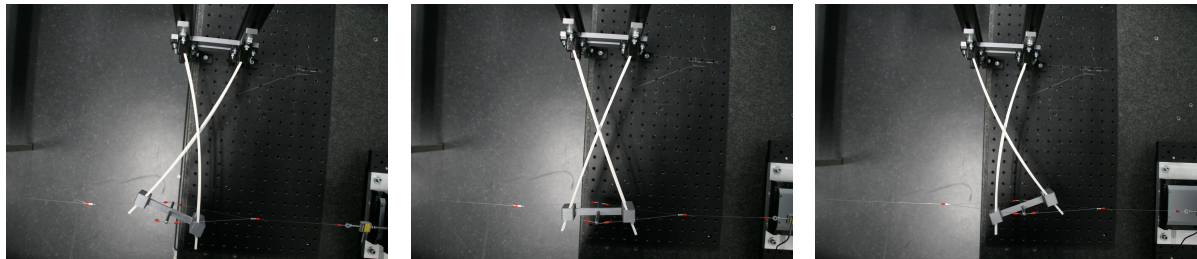


(a) Translational joint in left end position.

(b) Translational joint in the middle position.

(c) Translational joint in right end position.

Figure C.5: Positions of the translational joint over the range of motion without preload.



(a) Rotational joint in left end position.

(b) Rotational joint in the middle position.

(c) Rotational joint in right end position.

Figure C.6: Positions of the rotational joint over the range of motion without preload.

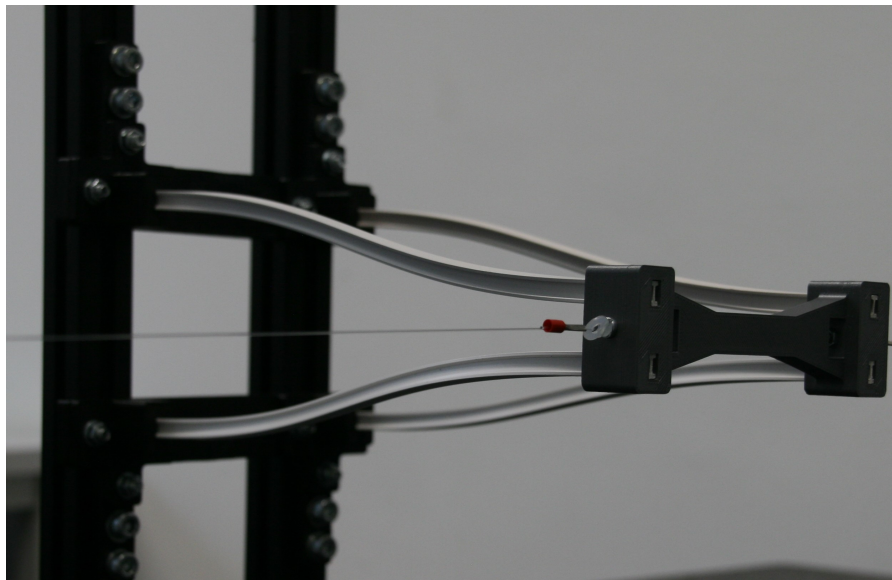


Figure C.7: Close-up on the translational joint at the critical preload displacement.

The double translational joint is tested to investigate the potential of adding multiple mechanisms in series. For the experiments, this prototype is tested with the beams oriented vertically. It is decided to do this because the influence of gravity could not be neglected for this prototype. A picture of the DTJ in the right end position is provided in Figure C.8.

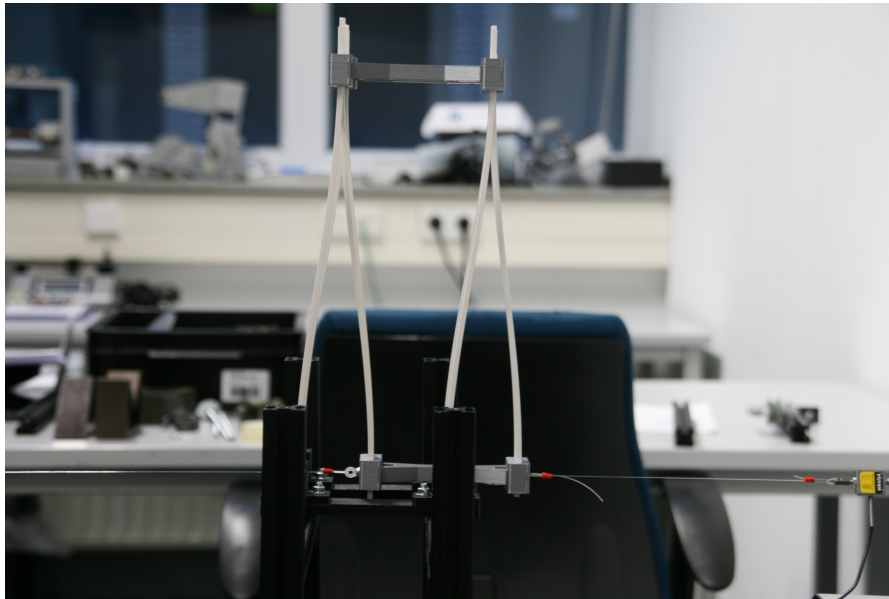
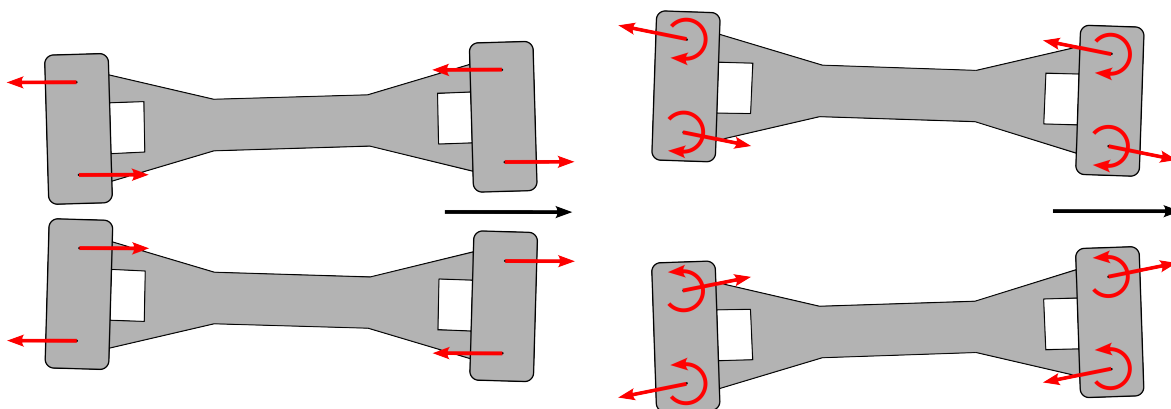


Figure C.8: Double rotational joint in right end position.

C.4. Rotation shuttles

As discussed in the research paper, the forces on the two top shuttles are not balanced out. This will be explained using the FBD in Figure C.9. The black arrow indicates the direction of the bottom shuttle. In the configuration without preload, the forces applied on the shuttles form a couple. These forces are indicated by the red arrows. This couple results in a rotation of the shuttles. In this situation, the left ends of the shuttles will move towards each other. In the preloaded situation, shown in Figure C.9b, some additional loads are applied on the shuttles. The I-beams also apply a vertical force component, resulting in a rotation of the resultant force. Additionally, a moment is applied on the shuttles by the I-beams. These moments are counteracting the rotation introduced by the forces. For a certain preload, the moments are dominant resulting in an opposite rotation. In this case, the right ends of the shuttles move towards each other.

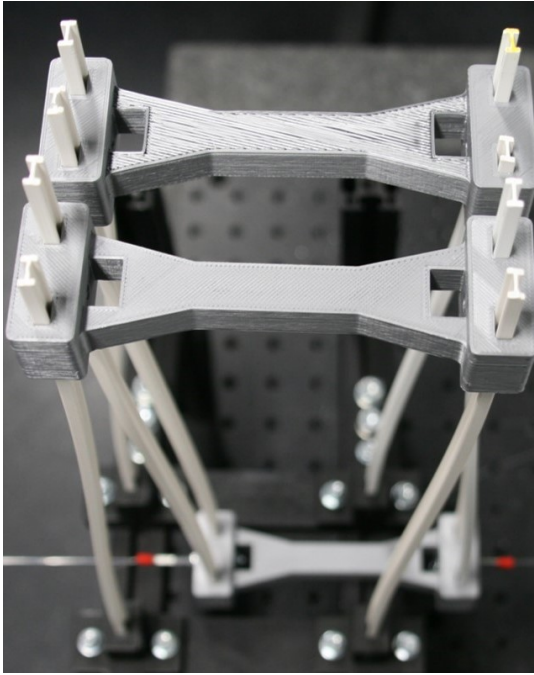


(a) FBD of the two shuttles without preload.

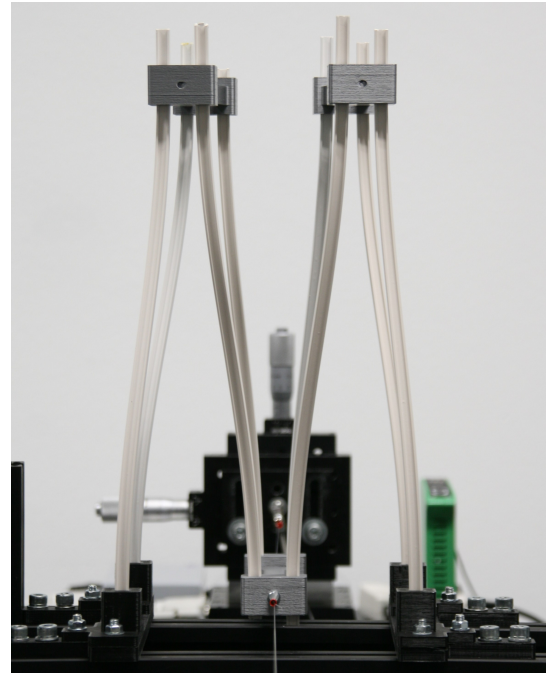
(b) FBD of the two shuttles with preload.

Figure C.9: Explanation of rotation of the shuttles. The displacement of the bottom shuttle is indicated with the black arrow. In red the applied loads are given.

The rotations are observed during the experiments. Figure C.10a shows the DTJ without preload. The left ends of the shuttles are rotated slightly towards each other. The preloaded configuration is shown in Figure C.10b. In the picture, the bottom shuttle moves away from the viewer. Similar to the result in Figure C.9b, the shuttles rotate towards each other at the same side the bottom shuttle is moving.



(a) Rotations of the shuttles in the configuration without preload.



(b) Rotations of the shuttles in the configuration with preload.

Figure C.10: Pictures of the prototype during the experiments. These pictures show the rotations of the two top shuttles when a lateral displacement y_d is applied.

D

Rotational joint

D.1. Basic model

In this appendix, an alternative design of the rotational joint is presented. Several designs for the compliant joints are considered during the project. One of the rotational joints showed potential but at the time it seemed not to be the best solution. The basic idea and some first results will be discussed in this appendix. The rotational joint consists of two flexible I-beams. The beams are connected to each other with a rigid part at the free end of the beams. The top-left plot in Figure D.1 shows the design of the rotational joint. The beams are of length L and the rigid part has a length R .

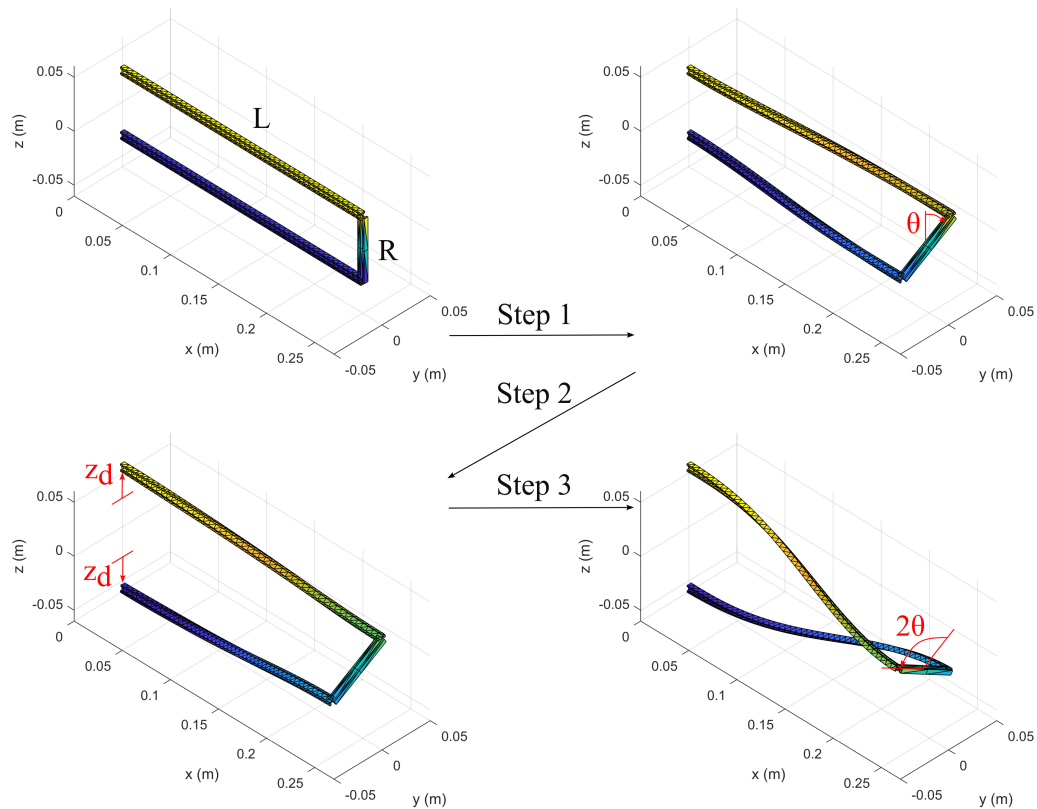


Figure D.1: Design of alternative rotational joint with stills from the FEA. Step 1 is a negative rotation θ around the x -axis. Step 2 is the preload displacement z_d , equally divided at the two end points. Step 3 is a positive rotation 2θ around the x -axis.

Figure D.1 also shows the loading steps of a single analysis of this joint. First, the rigid part is rotated a negative angle α around the x -axis. Next, the preload displacement z_d is applied at the fixed ends of the beams. The preload displacement is divided equally such that the middle point of the rigid part remains at the same position. Lastly, a positive rotation 2θ around the x -axis is applied on the rigid part. The reaction moment to this rotation is calculated and will be used in the analysis. A moment-angle plot of two different preload displacements is provided in Figure D.2. The red line corresponds with the mechanism without preload, the blue line is obtained with $z_d = 50$ mm. The results for this rotational joint are quite good, with a region of zero-stiffness of approximately 30° .

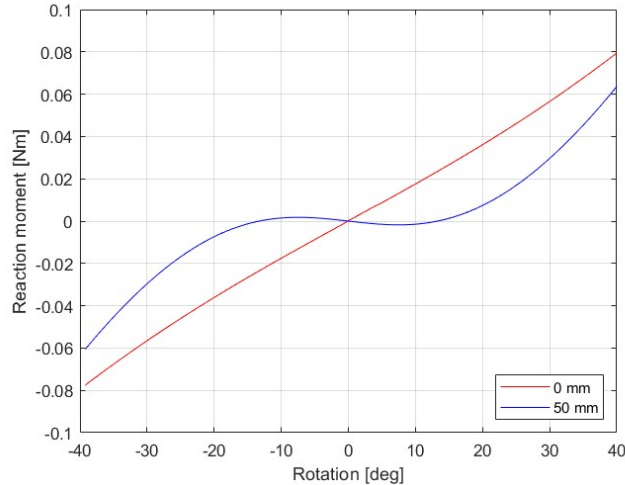


Figure D.2: Moment-angle plot of the rotational joint for two different preload displacements.

D.2. Improvement zero-stiffness range

There is an additional idea to further improve the region of zero-stiffness. However, proof of this idea is not obtained so far. For this idea one of the two beams in this design is analysed. The model consists of a cantilever beam, rotation of the end of the beam around y is constrained (just as in the model with 2 beams). A displacement is applied in the negative z -direction. First, the end of the beam will move vertically. At the displacement where lateral torsional buckling occurs, the end of the beam will start to move laterally. The displacement of the end of the beam in the $y - z$ -plane is provided in Figure D.3. Changing the cross-

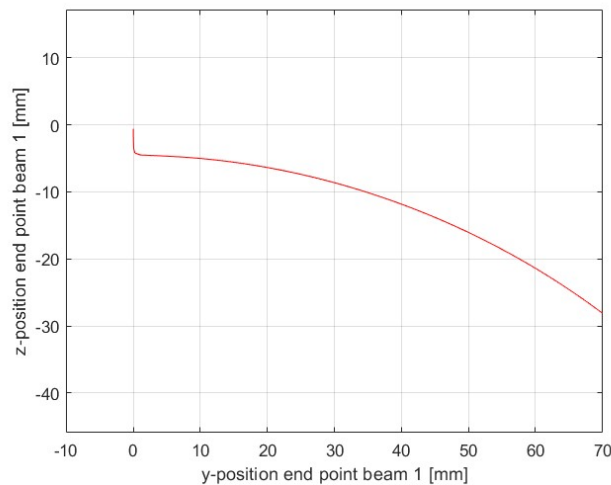


Figure D.3: Movement of the free end of a cantilever beam for lateral torsional buckling.

sectional dimensions and the length of the cantilever changes the path of the free end of the beam. The path of the free end of the beam looks like a part of a circle. The idea is the following: the region of zero-stiffness increases if we manage, by adjusting the cross-sectional dimensions and L and R , to overlap the circular path with the circular path of the rigid part in Figure D.1. This can be performed in a sensitivity analysis or in an optimization process.

E

Twisted beam

At the start of the project, many options for using LTB in a compliant mechanism were considered. One of the ideas was to change the shape of the beam. The aim of this idea was to be able to change the shape of the beam, such that LTB occurs at a desired place of the beam at a desired load or displacement. One of the possibilities to do this had promising results and will be discussed in this appendix.

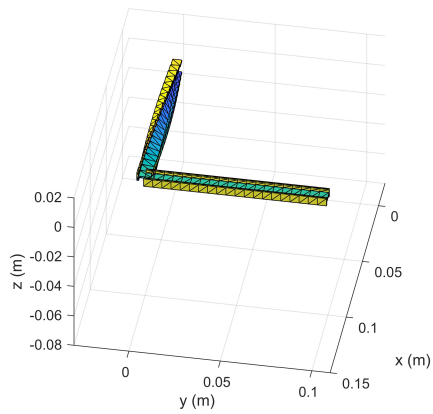
The beam in this design consists of two parts. One of the ends of the first part is fixed, and the other end is free. Over the length of the first part, the beam has a twist of 90° . This twist is modelled in the FEA using a helical function. The implementation of this function is shown below.

```
1 %% use this for a twisted guide curve
2 dia = 100;
3 pitch = 0.1;
4 height = 0.1;
5 t = linspace(0,-pi/2,20);
6 radius = dia/2;
7 yy = radius*sin(t);
8 zz = radius*cos(t);
9 xx = t/(pi/2)*pitch;
10
11 m.GuideCurve(:,1:20) = [xx; yy; zz];
12 s = linspace(0,2*pi,m.numberNodes);
13 m.GuideCurve(2,:) = m.GuideCurve(2,:) + 0.1*sin(s);
14
15 m.guidecurve = reshape(m.GuideCurve,3*m.numberNodes,1);
```

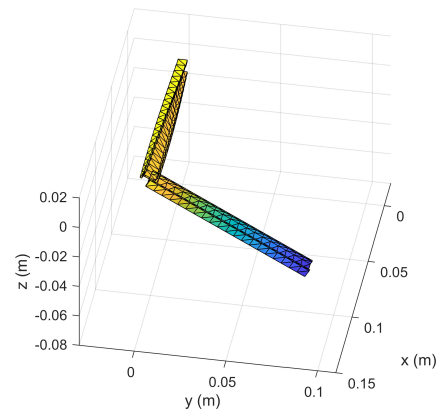
Perpendicular to the first part, a second part of the beam is modelled. The stiffness is multiplied by 1000 in order to make this part rigid. Both parts have a length of 0.1 m. At the end of the second part, a downward displacement z_d is applied. Some stills of the deformation for increasing z_d of this beam are provided in Figure E.1. After the twist in the first part of the beam is removed, lateral torsional buckling occurs as can be seen in Figure E.1d. The shown example is the most basic version of this idea. Some possible alternations and extensions are listed below.

- The second part of the beam can be connected to the first part with a small offset z_o in the positive z -direction (for example $z_o = 0.005$ m). This ensures that the twist in the first part of the beam is completely removed before LTB occurs. In the situation where the second part becomes almost vertical (approximately the position in Figure E.1c), the downward force will still have a moment arm with respect to the first part.
- The used angles in the model can be varied to change the behaviour of the beam. The twist-angle of the first part can be changed. Also, the orientation of the second part can be changed, a rotation around x and z both belong to the possibilities.
- This model contains two parts. The initial idea was to expand this to a beam with more parts that will buckle at the same time, or at different desired times. Ideally, we want to be able to model the (desired)

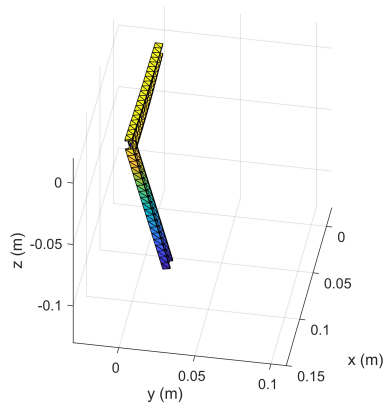
buckling behaviour of a beam with n parts. So far, this idea has some challenges that have not been solved yet.



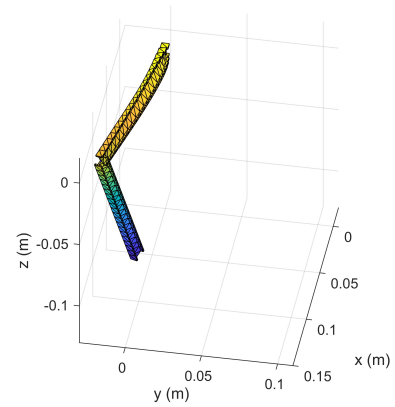
(a) Twisted beam with applied displacement $z_d = 0$ m.



(b) Twisted beam with applied displacement $z_d = -0.05$ m.



(c) Twisted beam with applied displacement $z_d = -0.10$ m.



(d) Twisted beam with applied displacement $z_d = -0.12$ m.

Figure E.1: Stills of the deformation of the twisted beam with perpendicular arm. Displacement z_d is applied at the end of the arm.

F

Matlab code

F.1. Analysis mechanism

In this appendix, the used MATLAB[®] code is provided. The first function is shown below. This function is a single analysis of the translational joint. The function can easily be adjusted to the rotational joint or the double translational joint by changing the geometry of the model in lines 20-43. As input, the dimensions to build the mechanism (H, W, h, w, L), the preload displacement z_d , lateral displacement y_d and some extra parameters are required. These parameters are for example the number of elements, the beam type that is used and the material properties E and G . In lines 56-65, the possibility to use rigidities is implemented. If this option is used, the rigidities EA, EI_{yy}, EI_{zz} and GJ obtained from the material tests are used. After the model is completely defined, three loading steps are performed. The displacements and reaction forces are saved in a struct for each time step. This struct is the output of the function and can be used to analyse the mechanism.

```
1 function [history3, m3] = Exp_compare_straight(z_d,y_d,par,params,H,W,h,w,L)
2 % LTB straight mechanism translational joint, single analysis of the
3 % mechanism. Input z_d,y_d,H,W,h,w and extra parameters in par and params.
4 % Output is struct with deformations and reaction force for each time step.
5 % Marco Moerman
6 % 11-10-2022
7
8 par.nTimestep = 20;
9 par.nIter = 100;
10 par.conv = 1e-6;
11 par.getKend = 0;
12 par.step = 'on';
13 par.view = 'off';
14 par.plots = 'off';
15
16 addpath '..\core'
17
18 %% Model
19 % generation of coordinates and connectivities
20 d1 = 0.1;
21 d2 = 0.02;
22 length_beam = L;
23 el_beam = params.Elements;
24
25 x_beam = linspace(0,length_beam,el_beam).';
26 y_beam = [repmat(0,length(x_beam),1) repmat(0,length(x_beam),1)...
27           repmat(d1,length(x_beam),1) repmat(d1,length(x_beam),1)];
28 z_beam = [repmat(0,length(x_beam),1) repmat(d2,length(x_beam),1)...
29           repmat(d2,length(x_beam),1) repmat(0,length(x_beam),1)];
30
31 x = [x_beam; x_beam(end); flip(x_beam); x_beam; x_beam(end); flip(x_beam)];
32 y = [y_beam(:,1); y_beam(end,1); y_beam(:,2); y_beam(:,3); y_beam(end,3); y_beam(:,4)];
33 z = [z_beam(:,1); d2/2; z_beam(:,2); z_beam(:,3); d2/2; z_beam(:,4)];
34
```

```

35 nbeam = numel(x);
36
37 m.X = [x y z, zeros(3,nbeam)'];
38 m.elementNodes = [1:2*el_beam 2*el_beam+2:nbeam-1 el_beam+1;...
39                 2:2*el_beam+1 2*el_beam+3:nbeam 3*el_beam+2]';
40 m.numberNodes = size(m.X,1);
41 m.numberElements = size(m.elementNodes,1);
42 m.eqn = 6*m.numberNodes;
43 m.x = reshape(m.X',m.eqn,1);
44
45 %% material properties
46 index = [el_beam el_beam+1 3*el_beam 3*el_beam+1 4*el_beam+1];
47 m.E = params.E * ones(1,m.numberElements);
48 m.E(index) = 1E3*params.E;
49 m.G = params.G * ones(1,m.numberElements);
50 m.G(index) = 1E3*params.G;
51
52 name = params.type;
53
54 m = DefineCrossSection(m,name,H,W,h,w);
55
56 if params.useEI == 1
57     m.E = 1 * ones(1,m.numberElements);
58     m.E(index) = 1E3*1;
59     m.G = 1 * ones(1,m.numberElements);
60     m.G(index) = 1E3*1;
61     m.A = params.EA*ones(1,length(m.A));
62     m.I22 = params.EI22*ones(1,length(m.I22));
63     m.I33 = params.EI33*ones(1,length(m.I33));
64     m.J = params.GJ*ones(1,length(m.J));
65 end
66
67 %%
68 %Use this for a single orientation point
69 CSO = [0 0 100]'; % cross section orientation. Is the point towards which e03 ...
70           points. Used to be fixed [0.00001 0.000001 1]'
71 m.GuideCurve = repmat(CSO,1,m.numberNodes);
72
73 s = linspace(0,2*pi,m.numberNodes);
74 m.GuideCurve(2,:) = m.GuideCurve(2,:) + 0.1*sin(s);
75
76 m.guidecurve = reshape(m.GuideCurve,3*m.numberNodes,1);
77
78 for e = 1:m.numberElements
79     % m.tr1(:, :, e) = eye(3)*rotRol(m.X(e+1,1:3)'-m.X(e,1:3)');
80     % m.tr2(:, :, e) = eye(3)*rotRol(m.X(e+2,1:3)'-m.X(e+1,1:3)');
81
82     %modified rotRol met richting e03 naar bepaald punt (niet de snelste versie)
83     x21=(m.X(m.elementNodes(e,2),1:3)'-m.X(m.elementNodes(e,1),1:3)');
84     e01 = (x21)/norm(x21);
85     % e03star = veccross(e01,[0.00001 0.000001 1]');
86     e03star = cross(e01, m.guidecurve(3*(m.elementNodes(e,1)-1)+[1:3]) - ...
87         m.X(m.elementNodes(e,1),1:3)');
88     e03 = e03star/norm(e03star);
89     e02 = cross(e03,e01);
90     Ro = [e01 e02 e03]; % voor eqn 4.28
91
92     m.tr1(:, :, m.elementNodes(e,1)) = eye(3)*Ro;
93     m.tr2(:, :, m.elementNodes(e,1)) = eye(3)*Ro;
94 end
95
96 m.tr1(:, :, m.numberElements) = eye(3)*Ro;
97 m.tr2(:, :, m.numberElements) = eye(3)*Ro;
98
99 % m.tr1 = repmat(eye(3),1,1,m.numberElements);
100 % m.tr2 = repmat(eye(3),1,1,m.numberElements);
101 m.Rg1 = ...
102     repmat(eye(3),1,1,m.numberElements);%repmat({eye(3)},m.numberElements,1);
103 m.Rg2 = repmat(eye(3),1,1,m.numberElements);
104
105 m.D = zeros(6,m.numberNodes)';

```

```

103 m.d                = zeros(m.eqn,1);
104
105 % PlotBeamsCrossSectionsModified(m,par, 'undeformed')
106
107 %% BOUNDARY CONDITIONS on begin- and endpoint
108 y_dist = -y_d;
109 ep1 = [0 0 0];
110 theta1= [0 0 0];
111 ep2 = [0 0 0];
112 theta2 = [0 0 0];
113 ep3 = [0 0 0];
114 theta3 = [0 0 0];
115 ep4 = [0 0 0];
116 theta4= [0 0 0];
117 mp1 = [nan y_dist nan];
118 thetamp1 = [0 0 0];
119 Fe = zeros(m.eqn,1);
120 PreFe = zeros(m.eqn,1);
121
122 mp                = [e1_beam+1 2*e1_beam+1 2*e1_beam+2];
123 bc                = [1:6 6*mp(1)-5:6*mp(1) 6*mp(2)-5:6*mp(2) 6*mp(3)-5:6*mp(3) m.eqn-5:m.eqn];
124 dofs.dp           = [ep1 theta1 mp1 thetamp1 ep2 theta2 ep3 theta3 ep4 theta4]';
125 dofs.all          = (1:m.eqn)';
126 dofs.bc           = bc(~isnan([dofs.dp]));
127 dofs.dp           = dofs.dp(~isnan([dofs.dp]));
128 dofs.R            = sparse(1:length(dofs.bc), [dofs.bc], 1+0*dofs.bc, length(dofs.bc), m.eqn);
129
130 [history, m] = solveNONLINstaticCOR(m, dofs, par, Fe, PreFe);
131
132 % PlotBeamsCrossSectionsModified(m,par, 'deformed')
133
134 %% Prepare for loading step 2
135 ep2 = [0 0 z_d];
136 ep3 = [0 0 z_d];
137 mp1 = [nan 0 nan];
138
139 bc                = [1:6 6*mp(1)-5:6*mp(1) 6*mp(2)-5:6*mp(2) 6*mp(3)-5:6*mp(3) m.eqn-5:m.eqn];
140 dofs.dp           = [ep1 theta1 mp1 thetamp1 ep2 theta2 ep3 theta3 ep4 theta4]';
141 dofs.all          = (1:m.eqn)';
142 dofs.bc           = bc(~isnan([dofs.dp]));
143 dofs.dp           = dofs.dp(~isnan([dofs.dp]));
144 dofs.R            = sparse(1:length(dofs.bc), [dofs.bc], 1+0*dofs.bc, length(dofs.bc), m.eqn);
145
146 [history2, m2] = solveNONLINstaticCOR(m, dofs, par, Fe, PreFe);
147 % PlotBeamsCrossSectionsModified(m2,par, 'deformed')
148
149 %% loading step 2
150 par.nTimestep     = 50;
151 y_dist = 2*y_d;
152 ep2 = [0 0 0];
153 ep3 = [0 0 0];
154 mp1 = [nan y_dist nan];
155 % Fe(pertub_node) = -pertub;
156
157 bc                = [1:6 6*mp(1)-5:6*mp(1) 6*mp(2)-5:6*mp(2) 6*mp(3)-5:6*mp(3) m.eqn-5:m.eqn];
158 dofs.dp           = [ep1 theta1 mp1 thetamp1 ep2 theta2 ep3 theta3 ep4 theta4]';
159 dofs.all          = (1:m.eqn)';
160 dofs.bc           = bc(~isnan([dofs.dp]));
161 dofs.dp           = dofs.dp(~isnan([dofs.dp]));
162 dofs.R            = sparse(1:length(dofs.bc), [dofs.bc], 1+0*dofs.bc, length(dofs.bc), m.eqn);
163
164 [history3, m3] = solveNONLINstaticCOR(m2, dofs, par, Fe, PreFe);
165
166 if history3(end).flag == 0
167     return
168 end
169 end

```

In Figures E1 and E2 the loading steps for the translational and rotational joints are provided for clarification on the designs of the joints and the order of the loading steps.

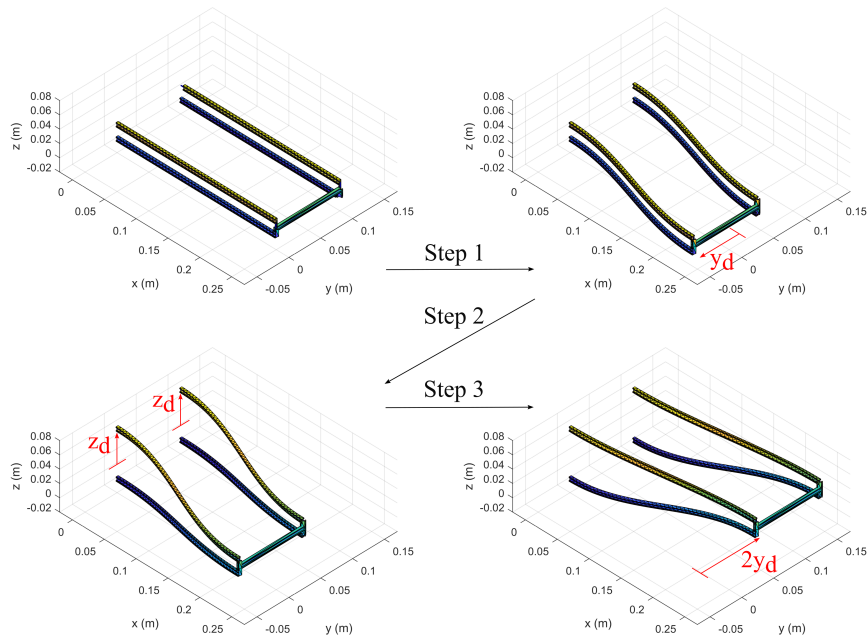


Figure E1: Stills to illustrate the loading steps of the translational joint. Step 1 is a lateral displacement y_d in $-y$. Step 2 is a preload displacement z_d in $+z$. Step 3 is a lateral displacement $2y_d$ in $+y$.

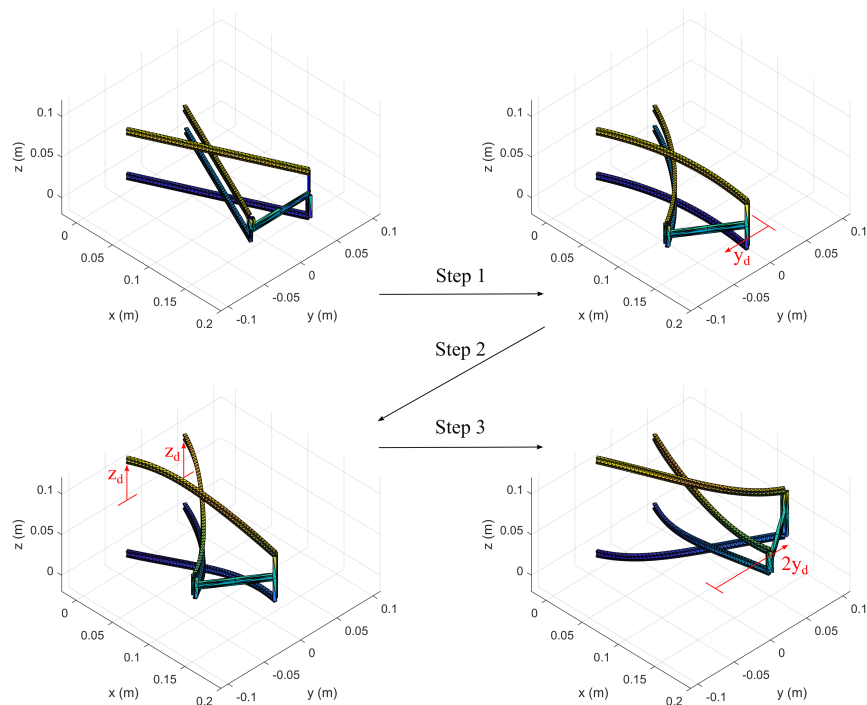


Figure E2: Stills to illustrate the loading steps of the rotational joint. Step 1 is a lateral displacement y_d in $-y$. Step 2 is a preload displacement z_d in $+z$. Step 3 is a lateral displacement $2y_d$ in $+y$.

E2. Sensitivity analysis

The results from this function are used for further analysis of the mechanism. For example, in the sensitivity analysis, the mechanism is analyzed for varying dimensions and preload displacements z_d . The code for the grid search that is performed for the sensitivity analysis of H and W is shown below. The cross-sectional dimensions and the length are used in vector x . This vector is used in the function *beamobjcon* which contains the calculation of the objective and constraints. These results are used to make a contour plot of the sensitivity analysis.

```

1 clear all
2 close all
3 % sensitivity analysis of design variable H and W. h,w and L are constant
4 % Marco Moerman
5 % 12-10-2022
6
7 % Design variables
8 Hgrid = 1:0.3:10;
9 Wgrid = 1:0.3:10;
10 h = 1;
11 w = h;
12 L = 0.25;
13 m.numberElements = 1;
14 name = 'Ibeam';
15 % Vector of output values
16 for i = 1:length(Hgrid)
17     for j = 1:length(Wgrid)
18         tic
19         x(1) = Hgrid(i);
20         x(2) = Wgrid(j);
21         x(3) = h;
22         x(4) = w;
23         x(5) = L;
24         m = DefineCrossSection(m,name,Hgrid(i),Wgrid(j),h,w);
25         if m.I33>m.I22
26             break
27         end
28         % Objective function
29         [f,g,r,z_opt, RF_lim, xcor1, xcor2] = beamobjcon(x);
30         % Grid value of objective function
31         fob(j,i) = f;
32         % Constraint
33         {r,g,r} = beamobjcon(x);
34         % Grid value of constraintsL
35         g1(j,i) = g(1);
36         g2(j,i) = g(2);
37         g3(j,i) = g(3);
38         g4(j,i) = g(4);
39         % optimal preload z values
40         z_opt_save(j,i) = z_opt;
41         RF_lim_save(j,i) = RF_lim;
42         xcor1_save(j,i) = xcor1;
43         xcor2_save(j,i) = xcor2;
44         progress = ((i-1)*length(Wgrid)+j)/(length(Hgrid)*length(Wgrid))*100;
45         time(j,i) = toc;
46         formatSpec = 'Progress = %4.2f, time = %4.2f s, H = %2.1f, W = %2.1f, obj = ...
47             %4.2f, pre = %4.2f\n';
48         fprintf(formatSpec,progress,toc,x(1),x(2), -f*1000, z_opt*1000)
49     end
50 end
51 %%
52 Hgrid = Hgrid(1:length(fob(1,:)));
53 Wgrid = Wgrid(1:length(fob(:,1)));
54 g1(g1==0) = nan;
55 g2(g2==0) = nan;
56 g3(g3==0) = nan;
57 fob(fob==0) = nan;
58 z_opt_save(z_opt_save==0) = nan;
59 RF_lim_save(RF_lim_save==0) = nan;

```

```

60 xcor1(xcor1==0) = nan;
61 xcor2(xcor2==0) = nan;
62
63 %%
64 %Contour plot of beam sensitivity
65 figure()
66 obj_contours = [12 16 20 24 28 32 36 40 44 48 52];
67 contour(Hgrid, hgrid, -fob*1000, obj_contours, 'showtext', 'on')
68 xlabel('Web height H [mm]')
69 ylabel('Flange thickness h [mm]')
70
71 hold on
72 contour(Hgrid, hgrid, g3, [0.0 0.0], 'r')
73 contour(Hgrid, hgrid, g3, [0.01 0.01], '--r', 'HandleVisibility', 'off') % Infeasible ...
    region
74
75 contour(Hgrid, hgrid, g4, [0.0 0.0], 'k')
76 contour(Hgrid, hgrid, g4, [0.02 0.02], '--k') % Infeasible region
77 grid on
78 legend('d_{zs} [mm]', 'Constraint strain', 'Constraint I_{zz}', 'Location', 'NorthEast')

```

In the function *beamobjcon* the region of zero-stiffness and the values for the constraints are calculated. The dimensions and constants are used in a function *z_optimization*.

```

1 function [f,c,ceq,z_opt, RF_lim, xcor1, xcor2] = beamobjcon(x)
2 % computation of scaled constraints
3 % LTB analysis of beams
4
5 % Input: Design variables H,W,h,w,L
6
7 % Output: region of zero-stiffness f, constraints c, equality constraints
8 % ceq, used optimal preload z_opt, bound on reaction force RF_lim,
9 % coordinates of zero-stiffness xcor1 and xcor2
10
11 % Assignment of variables
12 H = x(1)/1000;
13 W = x(2)/1000;
14 h = x(3)/1000;
15 w = x(4)/1000;
16 L = x(5);
17
18 % Constant beam values
19 beamparams;
20
21 % Analysis of current beam design strain
22 [y_res, epsilon, z_opt, RF_lim, xcor1, xcor2] = z_optimization(par,params,H,W,h,w,L);
23
24 f = -y_res;
25 % Scaled dimension constraint
26 % g(1) = W/H - 1;
27 %
28 % Scaled thickness constraint
29 % g(2) = 4*h/H - 1;
30
31 % Scaled strain constraint
32 epsilonmax = params.epsilonmax; % max strain [%]
33 g(3) = epsilon/epsilonmax - 1;
34
35 % Scaled constraint on Izz
36 g(4) = m.I33/m.I22-1;
37
38 c = g;
39 ceq = [];
40 end

```

The function *z_optimization* is used to calculate the optimal preload displacement for a set of design variables. First the preload displacement is estimated using the function *preload_estimation4*. Next the mechanism is analyzed once without preload in lines 7-12. Note that here a different function is used as the one provided at the start of this appendix. This function contains a single beam instead of four to minimize the calculation time. The result from this analysis without preload is used to calculate the bound on the reaction force RF_{lim} . In lines 15-21 the optimal preload displacement is determined using the MATLAB® function *fminsearch*. As a initial guess the result from the analytical estimation is used. The result from this optimization step x_2 is analyzed once more in lines 26-31. This analysis is used to calculate the region of zero-stiffness in line 40, in this code referred to as y_{res} . In lines 42-46 the maximum value of the strain in the mechanism is calculated.

```

1 function [y_res, epsilon, z_opt, RF_lim, xcor1, xcor2, RFz] = ...
   z_optimization(par, params, H, W, h, w, L)
2 % tic
3
4 [z_guess, Pcr] = preload_estimation4(H, W, h, w, L, params, par);
5
6 %% Calculation for RF_lim
7 z_dist0 = 0;
8 [history3, m3] = ...
   Opt_bistable_mech_complete_function_singlebeam(z_dist0, par, params, H, W, h, w, L);
9 for i = 1:length(history3)
10     RFy0(i) = history3(i).RF(7);
11 end
12 RF_lim = 0.01*max(RFy0);
13
14 %% fminsearch
15 x0_search = 2*z_guess;
16 opt2.options = optimset('Display', 'off', 'TolFun', 1E-4, 'TolX', 1E-4);
17 opt2.x0 = x0_search;
18 opt2.objective = @(x) z_obj(x, H, W, h, w, L, RF_lim);
19 opt2.solver = 'fminsearch';
20
21 [x2, fval2, exitflag2, output2] = fminsearch(opt2);
22
23 %% investigate result
24 z_dist = x2;
25
26 [history3, m3] = ...
   Opt_bistable_mech_complete_function_singlebeam(z_dist, par, params, H, W, h, w, L);
27 for i = 1:length(history3)
28     RFy(i) = history3(i).RF(7);
29     RFz(i) = history3(i).RF(8);
30     dispy(i) = history3(i).m.d(history3(end).dofs.bc(7));
31 end
32
33 % RF_lim = params.RF_lim;
34 Xq = linspace(-L/5, L/5, 2000);
35 Vq = interp1(dispy, RFy, Xq, 'spline');
36
37 index1 = find(Vq > -RF_lim, 1);
38 index2 = find(Vq < RF_lim, 1, 'last');
39
40 y_res = Xq(index2) - Xq(index1);
41
42 for i = 1:length(history3)
43     m = history3(i).m;
44     max_strain(i) = StrainEstimation(m, par, 'deformed');
45 end
46 epsilon = max(max_strain);
47
48 z_opt = z2;
49 RFz = max(RFz);
50 xcor1 = Xq(index1);
51 xcor2 = Xq(index2);
52 end

```

As discussed above, the function *preload_estimation4* is used to estimate the critical preload displacement of the mechanism. The function uses the cross-sectional dimensions and beam length as input and calculates the critical displacement of a cantilever beam [21].

```

1 function [z_guess, Pcr, I, Kbar] = preload_estimation4(H,W,h,w,L,params,par)
2 % Estimation of the critical preload of a cantilever beam
3 % Used formula obtained from Andrade et al. 'On the evaluation of elastic
4 % critical moments in double and singly symmetric i-section cantilevers.'
5 % Marco Moerman
6 % 23-09-2022
7
8 % beamparams;
9 m.numberElements = 1;
10 name = params.type;
11
12 m = DefineCrossSection(m,name,H,W,h,w);
13
14 % Method for estimating the critical load and displacement z
15 C2 = 0;
16 C3 = 0;
17 zg = 0;
18 zj = 0;
19 L = L/2;
20 hs = H+h;
21 G = params.G;
22 E = params.E;
23 It = m.J;
24 Iz = m.I33;
25 kz = 2;
26 kw = 1;
27 Iw = 1/4*Iz*hs^2;
28 I = m.I22;
29
30 Kbar = pi/L*sqrt((E*Iz*hs^2)/(4*G*It));
31 C1 = 2.462/sqrt(1+Kbar^2)+2.383*Kbar/sqrt(1+Kbar^2);
32 Mcr = ...
      C1*((pi^2*E*Iz)/((kz*L)^2))*(sqrt((kz/kw)^2*Iw/Iz+((kz*L)^2*G*It)/(pi^2*E*Iz))+ ...
      (C2*zg-C3*zj)^2)-(C2*zg-C3*zj));
33
34 Pcr = Mcr/L;
35 w2 = Pcr*L^3/(3*E*I);
36
37 z_guess = w2;
38 end

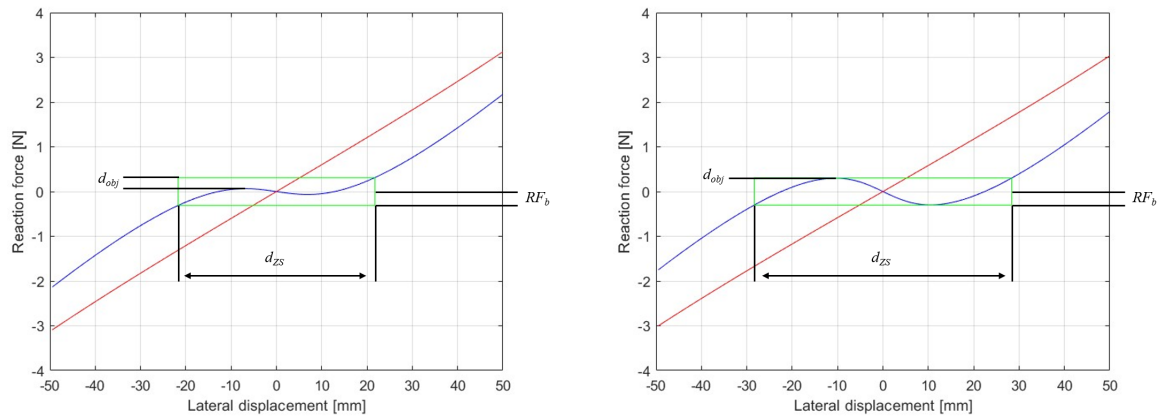
```

In *z_optimization* the optimal preload displacement is determined using *fminsearch*. The objective for this optimization step is defined in the function *z_obj*, which is provided below. The objective is minimizing the distance between the set value $+RF_b$ and the maximum value of the first half of the graph. This corresponds with the preload for which the maximum region of zero-stiffness is found.

```

1 function f = z_obj(x,H,W,h,w,L,RF_lim)
2 % Objective function
3
4 % Assignment of design variables
5 z_dist = x(1);
6
7 % Constant parameters
8 beamparams;
9
10 % Analysis of beam design
11 [y_res] = z_analysis(par,params,z_dist,H,W,h,w,L,RF_lim);
12
13 f = y_res;
14 end

```



(a) Raw data from the experiments on the translational joint with four different preloads. (b) Raw data from the experiments on the rotational joints with four different preloads.

Figure E3: Optimization process for determining the optimal preload $z_{d,opt}$.

In the function z_{obj} the mechanism is analyzed in the function $z_{analysis}$. This function is shown below, for a given set of cross-sectional dimensions, beam length and a preload displacement z_{dist} the distance between RF_b and the maximum of the first half of the graph is calculated. For clarification Figure E3 is provided. d_{obj} in Figure E3a is the objective and needs to be minimized. The optimal preload displacement for which the region of zero-stiffness is the largest is shown in Figure E3b. The mechanism is analysed in the function in line 7. It is a similar to the first function provided in this appendix. However, a single beam is analyzed in this function to minimize the computation time.

```

1 function [y_res] = z_analysis(par, params, z_dist, H, W, h, w, L, RF_lim)
2 % Analysis of the mechanism for a given set of cross-sectional dimensions
3 % and beam length. A preload distance z_dist is provided. The output y_res
4 % is the distance between RF_b and the top of the graph.
5 % Marco Moerman
6
7 [history3] = Opt_bistable_mech_complete_function_singlebeam(z_dist, par, params, H, W, h, w, L);
8 for i = 1:length(history3)
9     RFy(i) = history3(i).RF(7);
10    dispy(i) = history3(i).m.d(history3(end).dofs.bc(7));
11 end
12
13 %% objective function option 3
14 Xq = linspace(-L/5, L/5, 2000);
15 Vq = interp1(dispy, RFy, Xq, 'spline');
16 index1 = find(Vq>0, 1);
17 index2 = length(Xq)/2;
18 if index2<index1
19     index1 = index2-1;
20 end
21
22 maxx = max(Vq(index1:index2));
23
24 y_res = abs(RF_lim - maxx);
25 end

```

In $z_{optimization}$, an estimation is made of the maximal strain in the mechanism over the range of motion. This estimation is made using the function *StrainEstimation*, which is provided below. In lines 21-28 the coordinates of all the corners of the I-section are calculated for every element. The distance between a corner on node n and $n+1$ is approximated by a straight line between these points. This distance, together with the undeformed distance defined in line 8, is used in line 35 to calculate the strain.

```

1 function max_strain = StrainEstimation(m,par,def)
2 % In this function an estimation is made for the strain of every element.
3 % For this estimation the coordinates of the corners of an I-beam are
4 % determined by taking into account m.X, m.D and the rotations in m.tr1.
5 % Marco Moerman
6 beamparams;
7
8 dL0 = m.X(2,1); % aanpassen voor crossed beams
9
10 if strcmpi(def,'def',3)
11     coordinates = m.X + m.D;
12 elseif strcmpi(def,'und',3)
13     coordinates = m.X;
14 end
15
16 if strcmpi(m.CStype,'Ibeam',3)
17     H = m.H;% Flange-flange inner face height (web height)
18     W = m.W;% Flange (total) width
19     h = m.h;% thickness flanges
20     w = m.w;% web thickness
21     for e = 1:params.Elements-1
22         up=m.tr1(:,2,e);
23         side=m.tr1(:,3,e);
24         X= [ coordinates(m.elementNodes(e,1),1)+side(1)*W(e)*.5+up(1)*H(e)*.5; ...
              coordinates(m.elementNodes(e,1),1)+side(1)*W(e)*.5+up(1)*H(e)*.5+up(1)*h(e); ...
              ...
              coordinates(m.elementNodes(e,1),1)-side(1)*W(e)*.5+up(1)*H(e)*.5+up(1)*h(e); ...
              ...
              coordinates(m.elementNodes(e,1),1)-side(1)*W(e)*.5+up(1)*H(e)*.5; ...
              ...
              coordinates(m.elementNodes(e,1),1)+up(1)*H(e)*.5-side(1)*w(e)*.5; ...
              coordinates(m.elementNodes(e,1),1)-up(1)*H(e)*.5-side(1)*w(e)*.5; ...
              coordinates(m.elementNodes(e,1),1)-up(1)*H(e)*.5-side(1)*W(e)*.5; ...
              coordinates(m.elementNodes(e,1),1)-up(1)*H(e)*.5-side(1)*W(e)*.5-up(1)*h(e); ...
              ...
              coordinates(m.elementNodes(e,1),1)-up(1)*H(e)*.5+side(1)*W(e)*.5-up(1)*h(e); ...
              coordinates(m.elementNodes(e,1),1)-up(1)*H(e)*.5+side(1)*W(e)*.5; ...
              coordinates(m.elementNodes(e,1),1)+up(1)*H(e)*.5+side(1)*w(e)*.5; ...
              coordinates(m.elementNodes(e,1),1)+up(1)*H(e)*.5+side(1)*w(e)*.5; ...
              coordinates(m.elementNodes(e,1),1)+side(1)*W(e)*.5+up(1)*H(e)*.5];
25         Y= [ coordinates(m.elementNodes(e,1),2)+side(2)*W(e)*.5+up(2)*H(e)*.5; ...
              coordinates(m.elementNodes(e,1),2)+side(2)*W(e)*.5+up(2)*H(e)*.5+up(2)*h(e); ...
              ...
              coordinates(m.elementNodes(e,1),2)-side(2)*W(e)*.5+up(2)*H(e)*.5+up(2)*h(e); ...
              ...
              coordinates(m.elementNodes(e,1),2)-side(2)*W(e)*.5+up(2)*H(e)*.5; ...
              ...
              coordinates(m.elementNodes(e,1),2)+up(2)*H(e)*.5-side(2)*w(e)*.5; ...
              coordinates(m.elementNodes(e,1),2)-up(2)*H(e)*.5-side(2)*w(e)*.5; ...
              coordinates(m.elementNodes(e,1),2)-up(2)*H(e)*.5-side(2)*W(e)*.5; ...
              coordinates(m.elementNodes(e,1),2)-up(2)*H(e)*.5-side(2)*W(e)*.5-up(2)*h(e); ...
              ...
              coordinates(m.elementNodes(e,1),2)-up(2)*H(e)*.5+side(2)*W(e)*.5-up(2)*h(e); ...
              coordinates(m.elementNodes(e,1),2)-up(2)*H(e)*.5+side(2)*W(e)*.5; ...
              coordinates(m.elementNodes(e,1),2)+up(2)*H(e)*.5+side(2)*w(e)*.5; ...
              coordinates(m.elementNodes(e,1),2)+side(2)*W(e)*.5+up(2)*H(e)*.5];
26         Z= [ coordinates(m.elementNodes(e,1),3)+side(3)*W(e)*.5+up(3)*H(e)*.5; ...
              coordinates(m.elementNodes(e,1),3)+side(3)*W(e)*.5+up(3)*H(e)*.5+up(3)*h(e); ...
              ...
              coordinates(m.elementNodes(e,1),3)-side(3)*W(e)*.5+up(3)*H(e)*.5+up(3)*h(e); ...
              ...
              coordinates(m.elementNodes(e,1),3)-side(3)*W(e)*.5+up(3)*H(e)*.5; ...
              ...
              coordinates(m.elementNodes(e,1),3)+up(3)*H(e)*.5-side(3)*w(e)*.5; ...
              coordinates(m.elementNodes(e,1),3)-up(3)*H(e)*.5-side(3)*w(e)*.5; ...
              coordinates(m.elementNodes(e,1),3)-up(3)*H(e)*.5-side(3)*W(e)*.5; ...
              coordinates(m.elementNodes(e,1),3)-up(3)*H(e)*.5-side(3)*W(e)*.5-up(3)*h(e); ...
              ...
              coordinates(m.elementNodes(e,1),3)-up(3)*H(e)*.5+side(3)*W(e)*.5-up(3)*h(e); ...

```

```
        coordinates(m.elementNodes(e,1),3)-up(3)*H(e)*.5+side(3)*W(e)*.5;    ...
        coordinates(m.elementNodes(e,1),3)-up(3)*H(e)*.5+side(3)*w(e)*.5;    ...
        coordinates(m.elementNodes(e,1),3)+up(3)*H(e)*.5+side(3)*w(e)*.5;    ...
        coordinates(m.elementNodes(e,1),3)+side(3)*W(e)*.5+up(3)*H(e)*.5];
27     geo(:, :, e)=[X, Y, Z];
28     end
29 end
30 for j = 1:params.Elements-2
31     P1 = geo(:, :, j);
32     P2 = geo(:, :, j+1);
33     for i = 1:length(P1(:,1))
34         dL(j,i) = norm(P2(i,:) - P1(i,:));
35         strain(j,i) = (dL(j,i) - dL0) / dL0 * 100;
36     end
37     max_strain = max(abs(strain(j,:)));
38 end
```

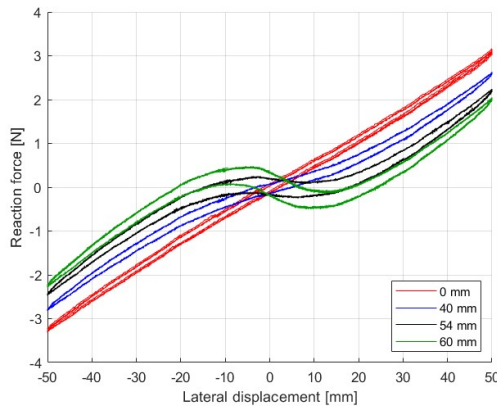

G

Data processing

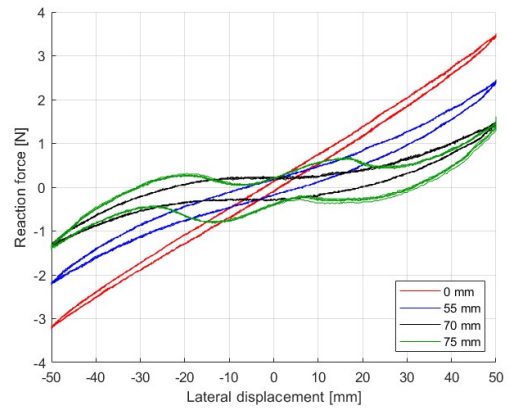
This appendix elaborates on the data processing of the experiments. During the experiments, the measurement data is saved in Excel files. The data is loaded into MATLAB[®] using the function *xlsread*. The data is divided into two vectors, one with the displacements and the other with the reaction forces. The lengths of these vectors may be different for each measurement. Therefore, an interpolation step is performed to make sure that all the vectors have the same length. The function used for the interpolation is shown below. The displacements and forces are divided into a forward and a backward motion.

```
1 function I = interpolate(data,x)
2 % Interpolation of the data and divide in forward and backwards motion
3 % Make vector of specified length
4
5 [~,index] = min(data(:,1));
6 % Divide in forward and backwards motion
7 dispF = data(1:index,1);
8 dispB = data(index:end,1);
9 forceF = data(1:index,2);
10 forceB = data(index:end,2);
11
12 % Interpolation of values
13 dF = dispF(round(dispF,2)~=0);
14 fF = forceF(round(dispF,2)~=0);
15 dB = dispB(round(dispB,2)~=0);
16 fB = forceB(round(dispB,2)~=0);
17
18 fF = fF(round(dF,2)~=round(max(dispF),2));
19 dF = dF(round(dF,2)~=round(max(dispF),2));
20 fB = fB(round(dB,2)~=round(max(dispB),2));
21 dB = dB(round(dB,2)~=round(max(dispB),2));
22
23 I.fF = interp1(dF,fF,x);
24 I.fB = interp1(dB,fB,x);
25
26 I = [I.fF I.fB]';
27
28 end
```

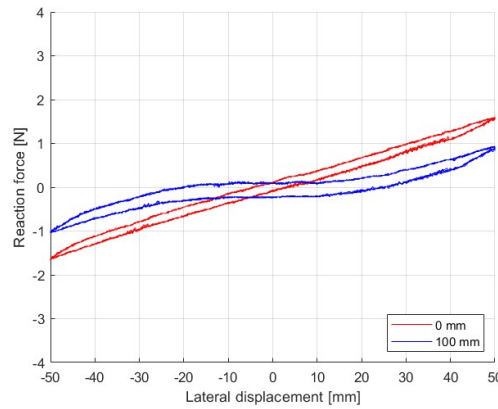
After the interpolation step the raw data is plotted. For the translational (TJ), rotational (RJ) and double translational (DTJ) the raw data is provided in Figure G.1. The curves in these plots are a collection of five measurements for every preload displacement.



(a) Raw data translational joint for four different preload displacements.



(b) Raw data rotational joint for four different preload displacements.

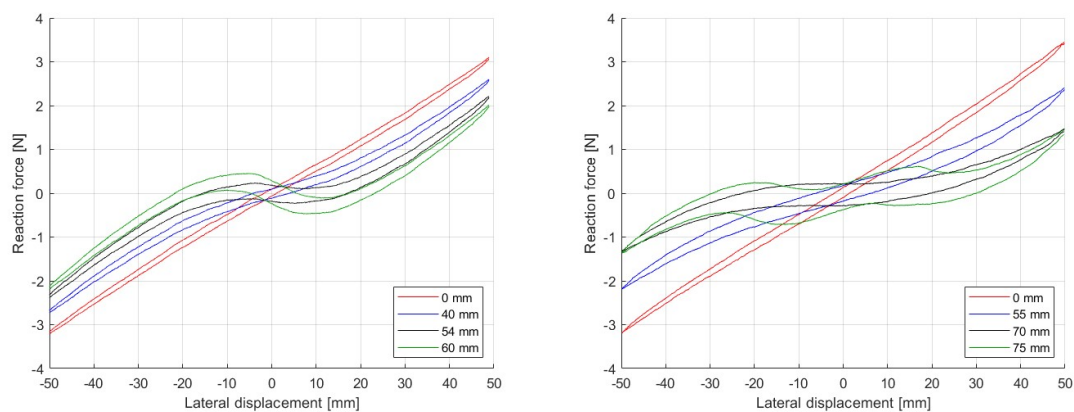


(c) Raw data double translational joint for two different preload displacements.

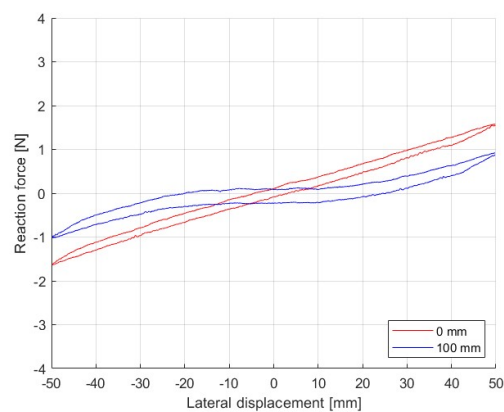
Figure G.1: Raw data from the experiments for the three prototypes.

After plotting the raw data, the mean of the five measurements is calculated for every configuration. These plots are provided in Figure G.2. By averaging the five measurements, the thickness of the plotted lines is decreased.

The mean of the measurements is compared to the results from the FEA. A simulation of the mechanism is performed using the same preload displacement as used in the experiment. One of the resulting figures is provided in Figure G.3, this plot corresponds to the black curves in Figures G.1a and G.2a. The blue line is the result of the FEA. Similar plots are obtained for the other configurations as well.



(a) Mean data translational joint for four different preload displacements. (b) Mean data rotational joint for four different preload displacements.



(c) Mean data double translational joint for two different preload displacements.

Figure G.2: Mean data from the experiments for the three prototypes.

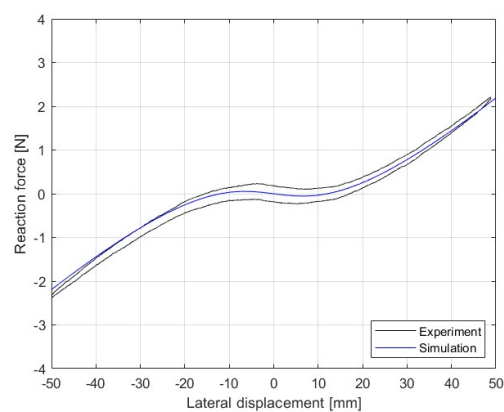


Figure G.3: Force displacement of the translational joint for a preload displacement $z_d = 54$ mm.

Bibliography

- [1] L. L. Howell, “Compliant mechanisms,” in *21st century kinematics*. Springer, 2013, pp. 189–216.
- [2] J. J. Uicker, G. R. Pennock, J. E. Shigley, and J. M. McCarthy, *Theory of machines and mechanisms*. Oxford University Press New York, 2003, vol. 768.
- [3] A. E. Albanesi, V. D. Fachinotti, and M. A. Pucheta, “A review on design methods for compliant mechanisms,” *Mecánica Computacional*, vol. 29, no. 3, pp. 59–72, 2010.
- [4] S. Jagtap, B. Deshmukh, and S. Pardeshi, “Applications of compliant mechanism in today’s world—a review,” in *Journal of Physics: Conference Series*, vol. 1969, no. 1. IOP Publishing, 2021, p. 012013.
- [5] Petermc, ““waste ye not” – a recycled rusty bike bell ;,” Jan 2012. [Online]. Available: <https://rustybikebell.wordpress.com/2012/01/24/waste-ye-not-a-recycled-rusty-bike-bell/>
- [6] M. Schenk and S. D. Guest, “On zero stiffness,” *Proceedings of the Institution of Mechanical Engineers, Part C: Journal of Mechanical Engineering Science*, vol. 228, no. 10, pp. 1701–1714, 2014.
- [7] G. Hao, “A framework of designing compliant mechanisms with nonlinear stiffness characteristics,” *Microsystem Technologies*, vol. 24, no. 4, pp. 1795–1802, 2018.
- [8] F. M. Morsch and J. L. Herder, “Design of a generic zero stiffness compliant joint,” in *International Design Engineering Technical Conferences and Computers and Information in Engineering Conference*, vol. 44106, 2010, pp. 427–435.
- [9] H. Zhao, C. Zhao, S. Ren, and S. Bi, “Analysis and evaluation of a near-zero stiffness rotational flexural pivot,” *Mechanism and Machine Theory*, vol. 135, pp. 115–129, 2019.
- [10] J. Van Eijk, “On the design of plate-spring mechanisms,” 1985.
- [11] T. Liu, S. Bi, Y. Yao, Z. Dong, Q. Yang, and L. Liu, “Research on zero-stiffness flexure hinge (zsfh) based on spring four-bar linkage (4bsl),” *Mechanism and Machine Theory*, vol. 143, p. 103633, 2020.
- [12] C.-W. Hou and C.-C. Lan, “Functional joint mechanisms with constant-torque outputs,” *Mechanism and Machine Theory*, vol. 62, pp. 166–181, 2013.
- [13] K. A. Tolman, E. G. Merriam, and L. L. Howell, “Compliant constant-force linear-motion mechanism,” *Mechanism and Machine Theory*, vol. 106, pp. 68–79, 2016.
- [14] Y.-H. Chen and C.-C. Lan, “An adjustable constant-force mechanism for adaptive end-effector operations,” 2012.
- [15] J. Gan, H. Xu, X. Zhang, and H. Ding, “Design of a compliant adjustable constant-force gripper based on circular beams,” *Mechanism and Machine Theory*, vol. 173, p. 104843, 2022.
- [16] I. Gandhi and H. Zhou, “Synthesizing constant torque compliant mechanisms using precompressed beams,” *Journal of Mechanical Design*, vol. 141, no. 1, 2019.
- [17] Q. Xu, “Design of a large-stroke bistable mechanism for the application in constant-force micropositioning stage,” *Journal of Mechanisms and Robotics*, vol. 9, no. 1, p. 011006, 2017.
- [18] J. Dekens, “Three-step method to design the preload of geometries to create spatial large range of motion zero-stiffness compliant mechanisms,” 2021.
- [19] M. BRETTLE, “Lateral torsional buckling and slenderness,” *New steel construction*, vol. 14, no. 9, 2006.
- [20] S. Timoshenko, J. Gere, and W. Prager, “Theory of elastic stability,” *Journal of Applied Mechanics*, vol. 29, no. 1, p. 220, 1962.

- [21] A. Andrade, D. Camotim, and P. P. e Costa, "On the evaluation of elastic critical moments in doubly and singly symmetric i-section cantilevers," *Journal of Constructional Steel Research*, vol. 63, no. 7, pp. 894–908, 2007.
- [22] I. Kalkan and S. Kartal, "Torsional rigidities of reinforced concrete beams subjected to elastic lateral torsional buckling," *International Journal of Civil and Environmental Engineering*, vol. 11, no. 7, pp. 969–972, 2017.
- [23] T.-S. Yang, P.-J. Shih, and J.-J. Lee, "Design of a spatial compliant translational joint," *Mechanism and Machine Theory*, vol. 107, pp. 338–350, 2017.
- [24] G. Hao, H. Li, X. He, and X. Kong, "Conceptual design of compliant translational joints for high-precision applications," *Frontiers of Mechanical Engineering*, vol. 9, no. 4, p. 331, 2014. [Online]. Available: https://journal.hep.com.cn/fme/EN/abstract/article_11781.shtml
- [25] D. Farhadi, N. Tolou, and J. Herder, "A review on compliant joints and rigid-body constant velocity universal joints toward the design of compliant homokinetic couplings," *Journal of Mechanical Design*, vol. 137, p. 032301, 03 2015.
- [26] J. Zhou, X. Wang, and Y. Mei, "Characteristic analysis of a quasi-zero-stiffness vibration isolator," in *IOP Conference Series: Materials Science and Engineering*, vol. 397, no. 1. IOP Publishing, 2018, p. 012045.
- [27] G. Radaelli, "Reverse-twisting of helicoidal shells to obtain neutrally stable linkage mechanisms," *International Journal of Mechanical Sciences*, vol. 202, p. 106532, 2021.
- [28] L. Xu and Z. Xiang, "Compliant quasi-zero stiffness device for vibration energy harvesting and isolation," *Sensors and Actuators A: Physical*, vol. 347, p. 113964, 2022.
- [29] T.-P. Dao and S.-C. Huang, "A compact quasi-zero stiffness vibration isolator using flexure-based spring mechanisms capable of tunable stiffness," *International Journal of Mechanical and Mechatronics Engineering*, vol. 10, no. 8, pp. 1572–1581, 2016.
- [30] R. C. Hibbeler, *Mechanics of materials*. Pearson Educación, 2005.
- [31] S. P. Timoshenko, "Strength of materials part 1," *Elementary theory and problems*, pp. 165–310, 1955.